FAILURE MODE INTERACTION IN FIBER REINFORCED LAMINATED COMPOSITES

by

Pavana Prabhakar

A dissertation submitted in partial fulfillment
of the requirements for the degree of
Doctor of Philosophy
(Aerospace Engineering)
in The University of Michigan
2013

Doctoral Committee:

Professor Anthony M. Waas, Chair
Brett A. Bednarcyk, NASA Glenn Research Center
Associate Professor Krishna Garikipati
Assistant Professor Veera Sundaraghavan

To Shunnu

ACKNOWLEDGEMENTS

The work presented in this thesis has been the product of influence and interactions with various people, and therefore, I would like to take this opportunity to thank all of them.

First and foremost, I would like to thank Professor Anthony Waas for his wonderful guidance during the past few years. He has been responsible for initiating and pursuing many ideas presented in this thesis. His tremendous enthusiasm towards research and teaching has always amazed and inspired me.

I would like to thank my committee members Dr. Brett Bednarcyk, Professor Krishna Garikipati and Professor Veera Sundararaghavan for their comments and suggestions on the thesis. I would like to express my gratitude towards all my professors who have taught me throughout my academic career. Especially, I am thankful to Professor Anthony Waas, Professor John Shaw, Professor Krishna Garikipati from University of Michigan, Ann Arbor, Professor Franscisco Armero from University of California, Berkeley, and Professor Narasimhan Mattur from National Institute of Technology Karnataka, Surathkal, and many others for having taught me the courses which built the necessary foundations for carrying out the research in this thesis. I would like to thank Dr. Brett Bedbarcyk and Dr. John Thesken for allowing me to spend a few months at NASA Glenn Research Center, where I got an opportunity to learn and interact with nation's great minds.

I am thankful to my labmates from the Composite Structures Lab at the University of Michigan, Ann Arbor who have directly or indirectly helped me over the past years.

Interactions with such a bright and friendly group of young engineers and scientists have given me a broad perspective about solid mechanics, and research in general. This has proven to be invaluable towards my research. I would like to express my gratitude towards all the technical and administrative staff in the Department of Aerospace Engineering at the University of Michigan.

Ann Arbor would not have been the same without the encouraging and sportive environment provided by friends- Devesh Kumar, Kalyan Nadella, Dr. Siva Rudraraju, Abhishek Kumar, Nhung Nguyen, Dr. Christian Heinrich, Dr. Qing Zhu and many others. I am thankful to Usha Ratna for being a great friend all the way from my undergraduate days. I would like to thank Karthik Anantharaman for the most cherished friendship, and his incessant encouragement.

This thesis would not be possible without the love and support of my family. I am thankful to my mother, Dr. H.R.Rukmini, for her tremendous encouragement and perpetual support towards my education and career; and my father, Dr. D.L.Prabhakar for his immense support towards my personal and intellectual growth, and more importantly for having introduced me to mechanics of materials for the very first time! This thesis is dedicated to my sister, Dr. Pavithra Prabhakar, for being my best friend and role-model, and a patient listener for life.

TABLE OF CONTENTS

LIST OF FIGURES

Figure

LIST OF TABLES

Table

LIST OF APPENDICES

Appendix

ABSTRACT

FAILURE MODE INTERACTION IN FIBER REINFORCED LAMINATED COMPOSITES

by

Pavana Prabhakar

Chair: Anthony M Waas

A novel computational modeling framework to predict the compressive strength of fiber reinforced polymer matrix composite (FRPC) laminates has been presented. The model development has been motivated by a set of experimental results on the compression response of two different FRPCs. The model accounts for failure mode interaction between kink-banding and interface fracture (or delamination), which are observed in the experimental results. To reduce the size of the computational model, those interfaces that are most susceptible to delamination are first determined through a free-edge stress analysis. Furthermore, off-axis layers, which are passive in the failure process are represented through an equivalent homogenized model, but the microstructural features of the on-axis layers (zero plies) are retained in the computational model. The predictions of the model matched well with the experimental observations, and they were found to accurately account for failure mechanism interactions. Therefore, this model has the potential to replace the need to carry out large numbers of tests to obtain the compressive strength allowable for FRPC laminates, the latter allowable being an essential element in the design of lightweight FRPC

aerostructures.

Furthermore, the thesis presents a new computational model to predict fiber-matrix splitting failure, a failure mode that is frequently observed in in-plane tensile failure of FRPC's. By considering a single lamina, this failure mechanism was seamlessly modeled through the development of a continuum-decohesive finite element (CDFE). The CDFE was motivated by the variational multiscale cohesive method (VMCM) presented earlier by *Rudraraju et al.* (2010) at the University of Michigan. In the CDFE, the transition from a continuum to a non-continuum is modeled directly (physically) without resorting to enrichment of the shape functions of the element. Thus, the CDFE is a natural merger between cohesive elements and continuum elements. The predictions of the CDFE method were also found to be in very good agreement with corresponding experimental observations.

CHAPTER I

Introduction

Composite materials are "hybrid" material systems which consist of two or more monolithic constituent materials that retain their individual identities, but result in a material with improved physical properties compared to the properties of the individual constituents. The constituent materials do not diffuse completely into each other, but instead retain their chemical, physical and mechanical properties. This is different from the composition of metallic alloys. Composite materials used in the aerospace industry are superior to bulk materials because of their high strength and stiffness to weight ratio [*Blockley and Shyy* (2010)]. This is because an aerospace grade composite material generally consists of a reinforcing phase that improves the strength and stiffness, and a matrix phase (the binder) which is relatively less stiff.

In many applications, a fiber or a particulate is used as a reinforcement, resulting in fiber composites or particulate composites. Due to processing difficulties of uniformly dispersing the particulate reinforcement, particulate composites contain less reinforcement as compared to fiber composites, and therefore are weaker and less stiff than fiber composites.

Fiber composites can be broadly classified into two types : continuous fiber composites with fibers that are relatively long (compared to their cross-sectional dimension) and discontinuous composites with fibers that are short and discontinuous with

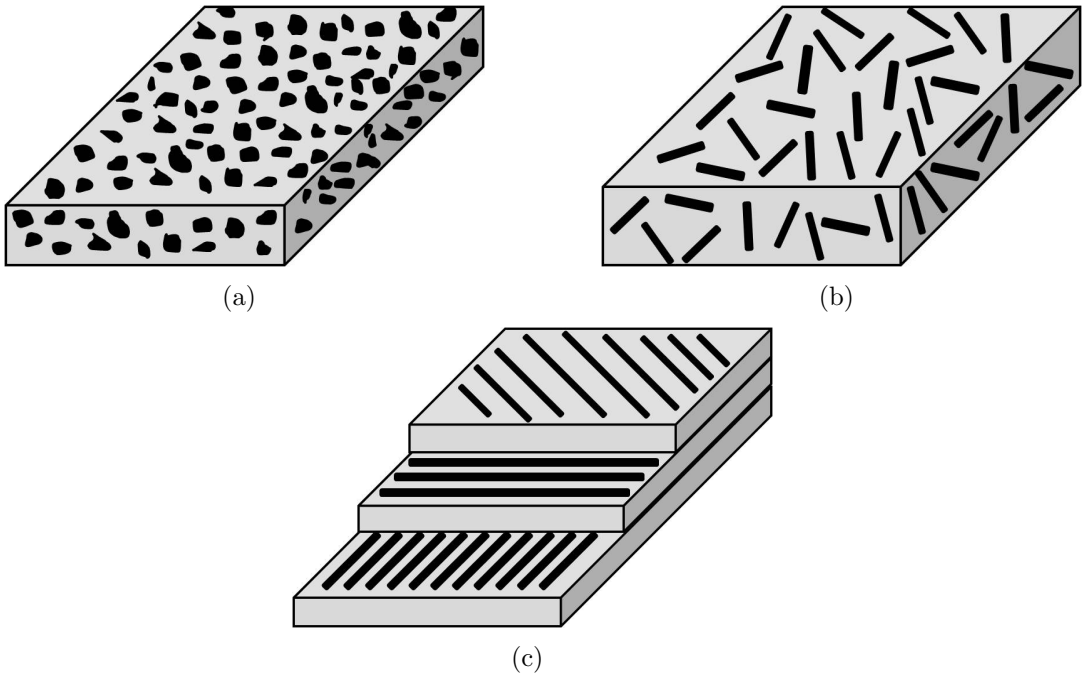

Figure 1.1: Types of fiber reinforced composites; (a) Particulate composite, (b) Discontinuous fiber composite, (c) Continuous fiber composite

small aspect ratios (the length to fiber diameter ratio). Continuous fiber composites usually have a preferred direction, whereas discontinuous fiber composites typically have random orientation of fibers. Fig. 1.1 shows some examples of particle, discontinuous and continuous fiber composites.

As mentioned earlier, in continuous fiber composites, the fibers impart a specific direction or orientation to the resulting fiber/matrix material system, forming a *lamina*. These individual lamina are stacked on top of each other with a specific direction, and consolidated together to form multidirectional laminates. If all the individual lamina have the same orientation, then the resulting laminate is called a unidirectional laminate, and they are referred to as multidirectional laminates if the individual lamina have different orientations. Fig. 1.2(a) and Fig. 1.2(b) show unidirectional and multidirectional laminates, respectively.

In the current work, multidirectional continuous fiber composites with carbon fiber reinforcements and polymer matrix material are considered. They are also known as

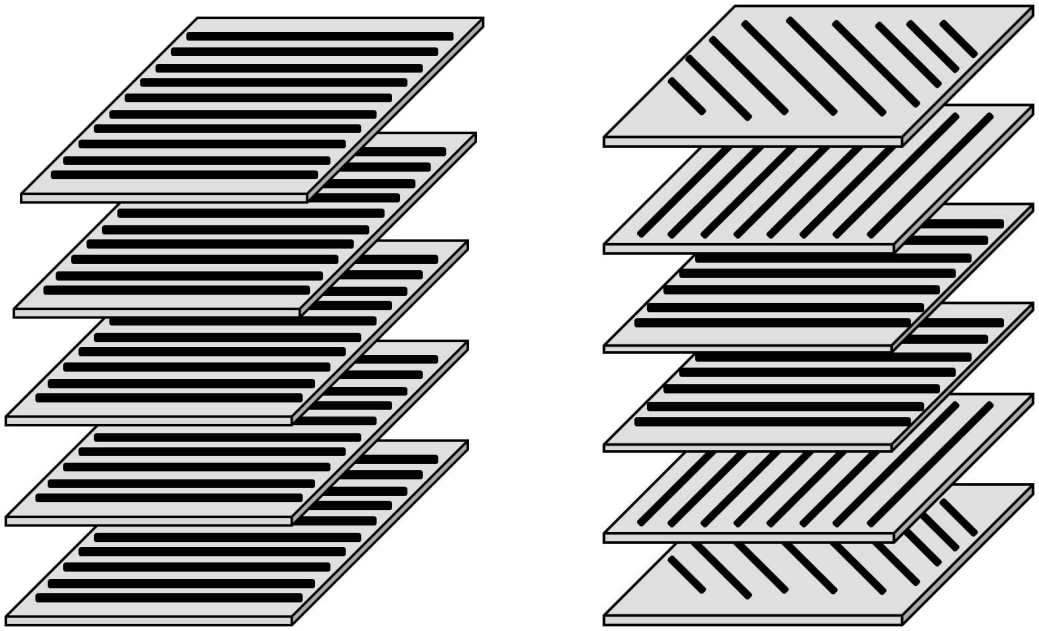

Figure 1.2: (a) Unidirectional laminate and (b) Multidirectional laminate

fiber reinforced polymer matrix composites (FRPC). In a real laminate (as opposed to the idealization shown in Fig. 1.2(a) and Fig. 1.2(b)), a resin rich region forms at the interface between the lamina. This is shown in Fig. 1.3, where for most of the lamina thickness, the fibers are densely packed, however, as the lamina stacking changes, a finite but non-negligible resin rich layer is seen to emerge. As indicated in Fig. 1.3, a typical lamina thickness ≈ 188 μm, while the resin rich region is ≈ 24 μm

.

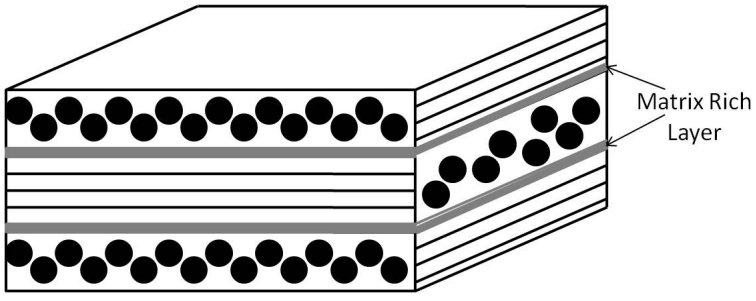

Figure 1.3: Multidirectional laminate with matrix rich layer between lamina

Some of the common failure mechanisms observed in FRPC as relevant to this

thesis are discussed in Section1.1.

1.1 Common Failure Mechanisms in Fiber-reinforced Laminates

Due to the presence of fiber and matrix in a FRPC, different failure mechanisms characteristic of the constituents are observed when the FRPC is subjected to different types of load profiles. Some common failure mechanisms observed when a laminate is subjected to compressive loading are kink band formation in the lamina that are aligned with the loading direction, matrix micro-cracking and delamination between laminae. Kink band formation (Fig. 1.4) is an instability caused by the axial loading on the "zero" fibers in a lamina. In addition, a mismatch in the properties of adjacent layers causes stress concentration between laminae, resulting in the interface matrix rich region to damage and create new surfaces by releasing energy. This type of failure is referred to as delamination (Fig. 1.5) failure. A combination of both kinking and delamination is observed at failure, as shown in Fig. 1.6.

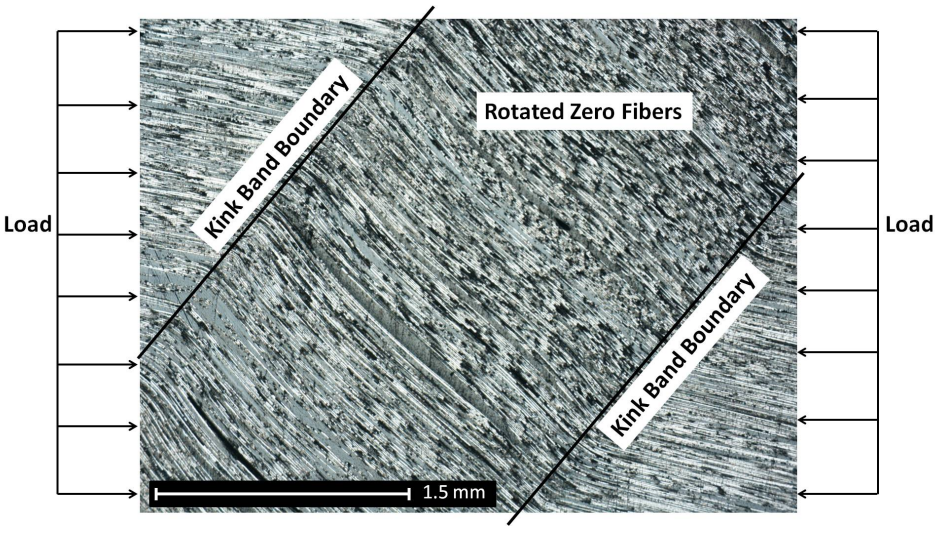

Figure 1.4: An image of a kink band that shows a band of fibers that have locally rotated with respect to other fibers that are aligned with the loading direction (with permission from Paul Davidson)

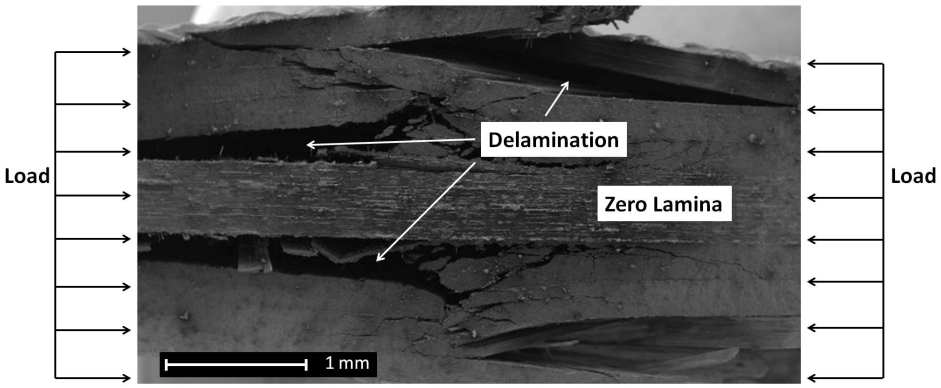

Figure 1.5: Delamination

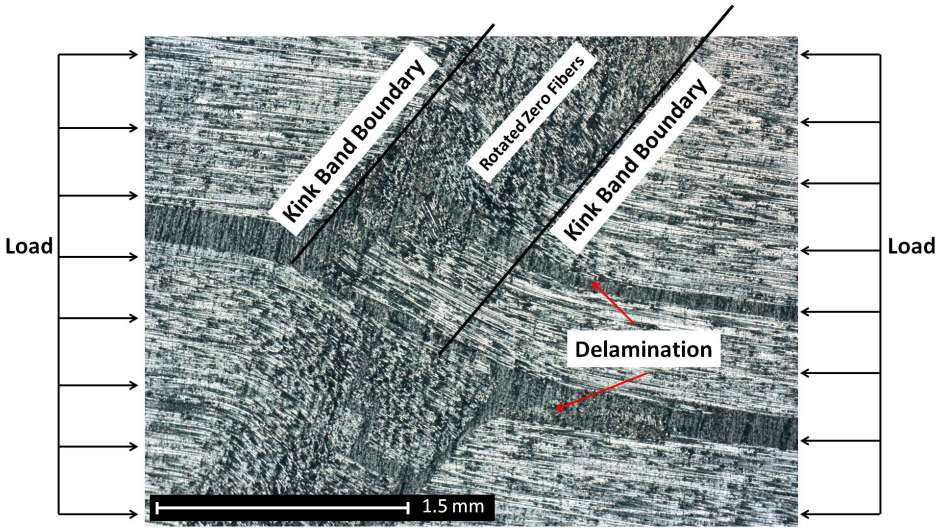

Figure 1.6: Kink band with delamination (with permission from Paul Davidson)

Under a combination of transverse and/or shear loading, matrix damage occurs within a lamina resulting in transverse cracks (Fig. 1.7), or also called matrix cracks. The crack paths are influenced by the presence of fibers in a lamina, and the cracks propagate rapidly to reach the free surface of the ply. Many small matrix cracks coalesce to form a large macroscopic matrix crack.

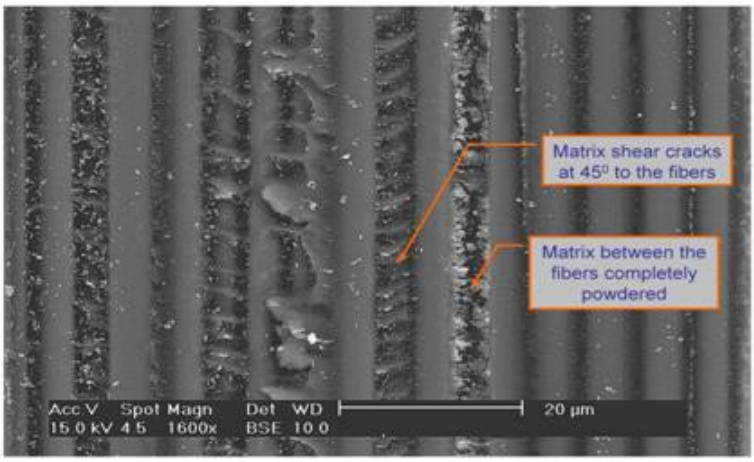

Figure 1.7: Matrix micro-cracking (with permission from Amit Salvi [*Ng et al.* (2010)])

1.2 Compressive Strength Allowable in Laminated Composites

The failure mechanisms mentioned above influence the load carrying capacity (also called "strength allowable") of the composites. These strength allowables are critical in designing structural components made of FRPC. Compressive strength allowables are one of the most significant design parameters in aerospace structures. The higher the compressive strength, the better the FRPC component is for aerospace structural components.

Fiber kink banding has been identified as a compressive strength limiting mechanism in FRPC's that are finding increasing use in lightweight aerostructures, [*Schultheisz and Waas* (1996) and *Waas and Schultheisz* (1996)]. While early studies determined that the compressive strength can be determined by a knowledge of the shear nonlinearity (the shear response, in the 1-2 plane of a lamina, where '1' denotes the fiber direction) in the stress-strain response of a lamina in tandem with a knowledge of initial fiber misalignment [*Budiansky and Fleck* (1993) and *Schapery* (1995)], it was later determined through a combination of experiments and numerical modeling

that kink band formation is an evolutionary process, which is governed by the local stress state (including stress multi-axiality), details of the material constitutive response and the fiber misalignment angles, as explained in the studies by *Sun and Jun* (1994), *Kyriakides et al.* (1995), *Lee and Waas* (1999), *Vogler et al.* (2001), *Yerramalli and Waas* (2003), *Yerramalli and Waas* (2004a), *Basu et al.* (2006), *Pimenta et al.* (2009a,b), *Feld et al.* (2011). As loading proceeds, regions of fiber misalignment in the composite undergo deformation due to combined compression, tension and shear loading in general. This region is surrounded by other material whose deformation characteristics, in general, are different. The progressively increasing local fiber misalignment coupled with shear behavior that exhibits a progressively decreasing tangent shear modulus, perpetuates a local limit-load type instability that initiates a rapid formation of a kink band. During this formation, the external tractions required to support the structure, in general, decrease, indicating an instability. The regions within the band undergo large straining, while material outside the band relaxes and unloads. Consequently, the mechanics of this process are related to the local microstructural details, geometry and volumes of materials that are within the band and that are outside the band.

Lee and Waas (1999), *Lee et al.* (2000), *Vogler et al.* (2001), and *Pimenta et al.* (2009a,b), have shown that kink-band formation can also involve splitting in combination or in isolation of the band formation. *Lee and Waas* (1999) studied the effect of fiber volume fraction on the compressive failure mode, while *Yerramalli and Waas* (2003) studied the effect of fiber type and load multi-axiality on failure. In both of these studies, energy released by splitting failure in combination with kinking was identified as contributing to the failure mechanism. Since the strains within the band can become in excess of the tolerable strain limits of the matrix and/or the fiber/matrix interface, it is conceivable that energy released by splitting is another mechanism by which energy is dissipated in the process of kink-band formation, in

addition to the nonlinear volumetric energy released by the matrix.

The formation of kink banding as an energy release mechanism in limiting the compressive strength of laminates with cut-outs has previously been addressed by *Waas et al.* (1990), *Ahn and Waas* (1999), *Ahn and Waas* (2002), and *Berbinau et al.* (1999), while the influence of fiber waviness on compressive failure of unidirectional laminates has been studied by *Wisnom* (1994). Micromechanical models to predict the compressive strength of composites have been proposed by *Naik and Kumar* (1999), and *Xu and Reifsnider* (1993), while the high strain rate response in compression has been addressed in *Guedes et al.* (2008), *Ochola et al.* (2004), *Pintado et al.* (2001) and *Hosur et al.* (2001).

A large part of this thesis is concerned with the interaction between delamination and kink-banding in the compressive failure of multidirectional composites, studied using a finite element model representation of the composite. FRPCs, when subjected to compression, exhibit different types of failure mechanisms, namely, microbuckling leading to kinking, delamination, and matrix damage. These modes of failure occur either separately or simultaneously depending on the loading, and they affect the global response of the laminate. Therefore, it is of importance to study the interaction among these different types of failure mechanisms and to understand the influence of different layer stacking on limiting compressive strength.

Multidirectional carbon fiber reinforced polymer (CFRP) matrix laminates are considered in this thesis, and the effects of the microstructure of the different laminae are embedded in a semi-homogenized representation of the laminate. Compressive strength prediction, and the study of the influence of failure mechanisms on the compressive strength, are major focuses of this thesis. Two of the main failure mechanisms observed through experiments are considered for modeling, namely kinking and delamination. While delamination is governed by the fracture properties of the matrix and/or fiber matrix interface, the kink banding is governed by the nonlinear response

of the matrix material in a misaligned fiber composite, *Yerramalli and Waas* (2004b). The effect of the stacking sequence on the compressive strength of multidirectional laminates is first studied through a set of experiments, and the experimental results are used to motivate the model development. A semi-homogenized laminate model accounting for kinking and delamination modes of failure is investigated. In order to allow for delamination in the computational model, interface elements are introduced in the inter-laminar regions.

1.3 Splitting Failure in Laminates

Splitting is a failure mechanism observed in laminates, and to distinguish it from delamination, the word "splitting" refers to failure in the matrix within a lamina and parallel to the fiber direction. Due to the presence of fibers in a lamina, the matrix between the fibers often undergo damage, and cracks can easily propagate though the matrix along the fiber. A novel continuum-decohesive finite element (CDFE) method is formulated to model fiber-matrix splitting failure in fiber-reinforced composite materials. Several methods have been proposed previously to model failure in the post-peak regime. For failure by fracture, if the crack path is known a-priori, cohesive zone models have shown promising results. These elements adopt a non-linear traction separation law across the crack faces [*Pietruszczak and Mroz* (1981); *Ungsuwarungsri and Knauss* (1987); *Song and Waas* (1993); *Schellekens and DeBorst* (1993); *Xu and Needleman* (1994); *Camacho and Ortiz* (1996); *Xie and Waas* (2006); *Xie et al.* (2006)], and have zero thickness. They are added along the pre-ordained direction of crack propagation. In order to overcome this limitation, element enriched finite elements [*Armero and Garikipati* (1996); *Garikipati and Hughes* (1998); *Jirasek* (2000)] and nodal enriched finite elements [*Moes et al.* (1999); *Moes and Belytschko* (2002)] have gained popularity, where discontinuities are embedded in the finite elements through shape functions. The Variational Multiscale Cohesive Method

(VMCM) is an element enrichment method where the cohesive law is embedded into continuum elements through discontinuous shape functions. This method has been successfully demonstrated previously by *Rudraraju et al.* (2010).

The current CDFE formulation is motivated by the VMCM, but the element fracturing, modeled as a sharp discontinuity, is carried out directly (physically) as opposed to enriching through the shape functions. In the CDFE approach, the fine scale is seen to emerge upon satisfaction of a failure initiation criterion, which is the onset of departure from a continuum description. The formulation is such that any additional degrees of freedom associated with the fine scale in the CDFE are condensed out, so that the equivalent stiffness matrix and force vector corresponding to the original nodal displacements of the element are maintained, providing computational efficiency. Thus, in the CDFE, the global degrees of freedom are fixed, regardless of the number of cracks (in a multiple cracking situation), much like the VMCM, but the method still captures mesh objective failure due to sharp cracks. The two sub-elements of a fractured element communicate through a traction-law that embeds the fracture properties of the newly created fracture surfaces. Because of this, the CDFE is unlike the crack-band model, *Bazant and Oh* (1983), and is also different from the smeared crack approach [*Rots et al.* (1985); *Heinrich and Waas* (2012)].

The CDFE method is demonstrated in this thesis by modeling an open hole tension test of a unidirectional lamina. Laminae, with fibers oriented at different angles to the loading direction (0,45,90) and containing a central circular hole are subjected to remote tensile loading. The ensuing deformation response, which includes the emergence of a sharp crack along the weak matrix layers between the fibers, is captured. The predictions are seen to agree with the corresponding experimental results.

1.4 Main Contributions and Organization of the Thesis

In this thesis, novel computational models to predict the compressive strength of FRPCs have been presented. The model development was motivated by a set of experimental results on two types of FRPC laminates. The model predictions are found to agree with experimental observations and account for failure mechanism interactions. Therefore, the model has potential to replace the need to carry out a large number of tests to obtain the compressive strength allowable for FRPC laminates, an essential requirement in the design of lightweight FRPC aerostructures. Furthermore, fiber-matrix splitting, a failure mode that is frequently observed in in-plane tensile failure of FRPCs was seamlessly modeled through the development of a novel continuum-decohesive finite element (CDFE) method, which was motivated by the variational multiscale cohesive method (VMCM) presented earlier by *Rudraraju et al.* (2010). The predictions of the CDFE method were also seen to be in good agreement with experimental observations. Fundamental material and fracture parameters that are needed to implement the model were measured for the FRPC material system, which was used throughout the thesis studies.

The dissertation is organized as follows; Chapter II provides a detailed description of the semi-homogenizing technique for the lamina in a laminate. Next, in Chapter III, a finite element method formulation to determine the delamination prone interfaces in a laminate is described. In order to model the interfaces in a multidirectional laminate, interface elements (DCZM) are introduced in Chapter IV, and the coupon level tests that are required to determine the input properties for implementing the element are described. Chapter V presents the results for the compressive response of two laminates with different stacking sequences. The computational model predictions are seen to match well with experimentally observed failure mechanisms and compressive strengths. Preliminary work conducted towards interactive failure between kinking and splitting in unidirectional laminate is presented in Appendix B.

In Chapter VI, the continuum-decohesive finite element (CDFE) method to capture splitting in fiber-reinforced lamina is formulated, and predictive results are presented along with corresponding experimental results. Then, the dissertation concludes with Chapter VII, which provides a summary of the main findings and suggestions for future work.

CHAPTER II

Homogenizing Technique to Determine the Compressive Strength of Laminated Composites

2.1 Introduction

In this chapter, a homogenizing technique is introduced for laminates. Multidirectional carbon fiber reinforced polymer (CFRP) matrix laminates are considered here, and the effects of the microstructure are embedded in the homogenized off-axis laminae of the laminate. This chapter is concerned with the effects of homogenizing the laminae on the compressive kink-banding instability, investigated by comparing a micro-mechanics based 3D finite element model representation of the composite with the semi-homogenized model. While delamination is governed by the fracture properties of the matrix and/or fiber matrix interface, the kink banding is governed by the nonlinear response of the matrix material in a misaligned fiber composite, *Yerramalli and Waas* (2004b). Here, the inter-laminar delamination is not accounted for. Instead the focus is the effect of homogenizing laminae on the predicted compressive strength, limited by the kink-banding instability. This semi-homogenized model will be used in conjunction with interface elements to include delamination prediction capability in the model, as shown later in Chapter V.

2.2 Discrete Fiber-matrix Model

An 8-layered 3-D finite element micro-mechanical model of a CFRP laminate is created with a layup of $[-45/+45/90/0]_s$. This 8 layer stack is a repeat unit that is representative of a bigger laminate. Each lamina is a hexagonally packed transversely isotropic layer having three rows of fibers. The fiber diameter and the volume fraction are 6 μm and 0.49, respectively. These laminae are scaled layers that capture these two features but do not have the same thickness as the laminae in an actual laminate. Fig. 2.1 shows the scale model simplification of the laminate, where red, cream, blue and green regions are fibers in -45, +45, 90 and 0 degrees, and the rest is the matrix material.

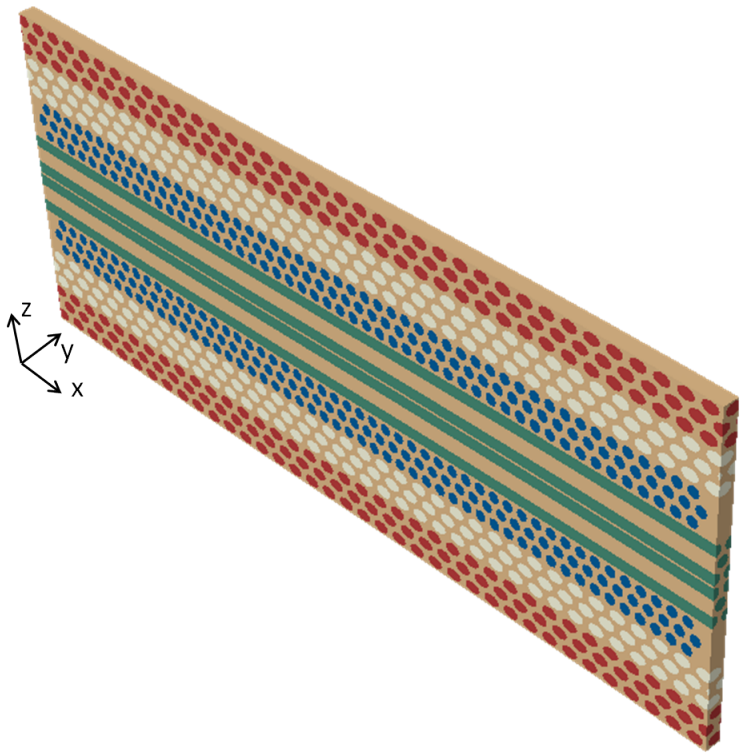

Figure 2.1: 8-layered 3-D finite element model of the laminate with discrete fibers and matrix

The fibers are modeled as elastic transversely isotropic material, and the corresponding properties are given in Table 2.1 (*Lee and Waas* (1999)). The matrix

is modeled as an elastic-plastic isotropic material, and the equivalent stress-strain response is as shown in Fig. 2.2 (*Ng et al.* (2010)).

Table 2.1: Fiber properties (*Lee and Waas* (1999))

E_{11}(GPa)	E_{22}(GPa)	E_{33}(GPa)	G_{12}(GPa)	G_{13}(GPa)	G_{23}(GPa)	ν_{12}	ν_{13}	ν_{23}
276	8.76	8.76	12.0	12.0	3.244	0.35	0.35	0.35

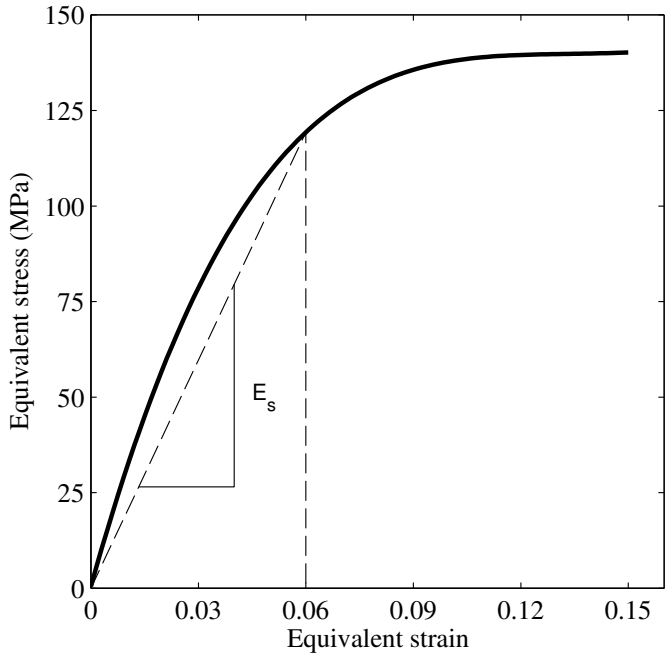

Figure 2.2: Equivalent stress-strain response of the matrix *Ng et al.* (2010)

A schematic of the model, shown in Fig. 2.3 is further used to describe the boundary conditions and the loading on the model. The edge AE of the model is prevented from motion in the z-direction, and the corner E is fixed against moving in the global x, y and z-directions. The face BFGC is subjected to compression along the negative x-direction in a displacement control manner. The faces ABCD and EFGH are held flat but are allowed to expand or contract in the y-direction. Also, the faces ABCD and EFGH deform exactly the same way in the x and z-directions. This enables the use of one representative unit cell in the y-direction, along with preserving a constant initial stiffness of the laminate, regardless of the width of the model.

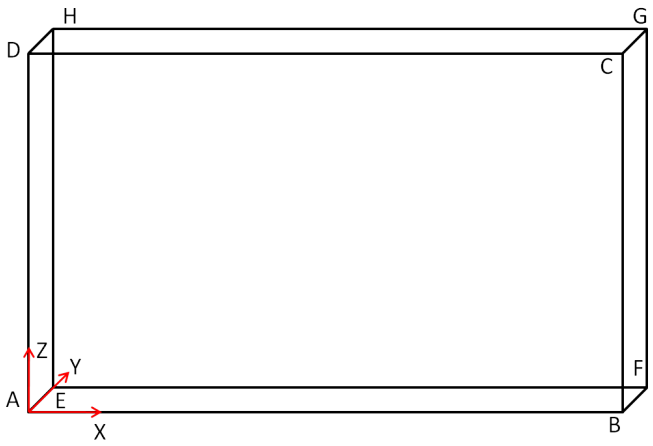

Figure 2.3: A schematic of the laminate model to describe boundary conditions and loading

The Riks method option available in ABAQUS v6.10, which is an arc-length solution scheme, is adopted to conduct the compressive response analysis. As shown in previous studies (*Beghini et al.* (2006)), this method captures unstable equilibrium paths (path in the load vs. loaded edge displacement graph that may show snap-back response) that can occur at limit points, as will be discussed later.

The model is meshed with 3-D tetrahedral and hexahedral elements (C3D4 and C3D8 in ABAQUS v6.10). A slight imperfection is imparted to the model to account for fiber misalignment. Previous work (*Yurgartis* (1987)) has shown that initial misalignment angles of 1 to 2 degrees of the zero laminae bound the distribution of fiber misalignment that is typical of carbon fiber reinforced pre-preg aerospace laminates. The first buckling mode of the laminate is determined by a linear perturbation analysis. Due to the boundary conditions prescribed, the buckling occurs only in the x-z plane, and any buckling in the x-y plane is suppressed. The buckling analysis gives a mode shape with a value of angle of imperfection defined as θ, where $\theta = \frac{\delta}{L}$, as shown in Fig. 2.4. This shape is scaled to make θ equal to a required angle of imperfection.

The initial state in the compression analysis is stress free. The model is seeded with fiber misalignment angles (θ) of 1^0, 1.5^0 and 2^0, and subjected to compression.

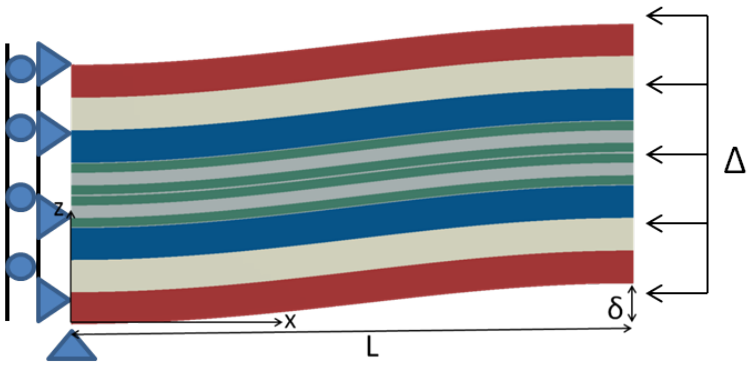

Figure 2.4: Laminate model to describe angle of imperfection

The macroscopic compressive stress-strain response for each case is plotted in Fig. 2.5. Here, macroscopic stress is defined as the total resultant x-direction reaction force on the face BFGC divided by the product of the width BF and thickness BC, while the macroscopic strain is defined as the total contraction (change in length between the faces BFGC and AEHD) divided by the initial length AB (refer to Fig. 2.3).

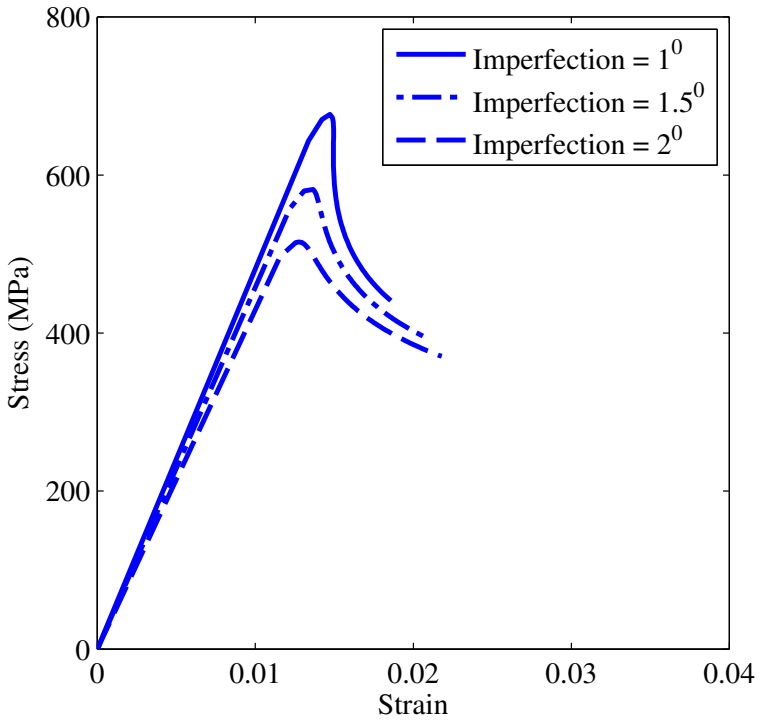

Figure 2.5: Global compressive stress-strain response of the discrete fiber-matrix model

Initially, the micro-laminate response is linear until close to a maximum stress (limit stress) at which the non-linearity of the matrix becomes dominant, and a slight snap-back in the response is observed for small imperfection angles. As the misalignment angle increases, this snap back decreases and the peak stress also diminishes. The peak stress corresponding to the misalignment range, 1^0-2^0 (practical range of misalignment of the zero layers in laminates) is in the range of 515-677 MPa (comparable to compressive strengths obtained from experiments, and reported in *Prabhakar and Waas* (2012a)). The initial (linear) stiffness of the response shown in Fig. 2.5 is approximately 48.5 $\pm$ 0.2 GPa.

2.3 Mathematical Formulation of the Upscaling Technique

The concentric cylinder model (CCM) approach is used to homogenize the fiber - matrix system in a lamina of a laminate. The inner cylinder is the fiber and the outer cylinder is the matrix, as shown in Fig. 2.6.

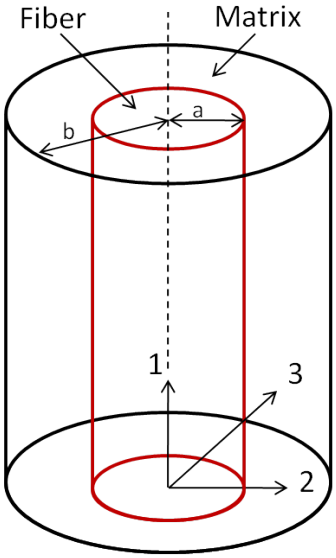

Figure 2.6: A sketch of the concentric cylinder model

The homogenized elastic properties of the lamina are determined by using the well established equations of the concentric cylinder model, given in Appendix A.

Beyond the elastic regime, the homogenized lamina material is represented using Hill's anisotropic potential (refer to *Lubliner* (2008)) given by,

$$f = F(\sigma_{22}-\sigma_{33})^2+G(\sigma_{33}-\sigma_{11})^2+H(\sigma_{11}-\sigma_{22})^2+2L\tau_{23}^2+2M\tau_{31}^2+2N\tau_{12}^2 = constant \tag{2.1}$$

where F, G, H, L, M and N are the relative ease/difficulty of yielding in different directions due to anisotropy in laminates created by the presence of orthotropic fibers in an isotropic matrix. These constants are defined as,

$$\begin{aligned} F &= \frac{1}{2}[\frac{1}{R_{22}^2}+\frac{1}{R_{33}^2}-\frac{1}{R_{11}^2}] \\ G &= \frac{1}{2}[\frac{1}{R_{33}^2}+\frac{1}{R_{11}^2}-\frac{1}{R_{22}^2}] \\ H &= \frac{1}{2}[\frac{1}{R_{11}^2}+\frac{1}{R_{22}^2}-\frac{1}{R_{33}^2}] \\ N &= \frac{3}{2R_{12}^2}; M = \frac{3}{2R_{13}^2}; L = \frac{3}{2R_{23}^2} \end{aligned} \tag{2.2}$$

where, R_{ij}=$(\sigma'_{ij})/\sigma_0$ for i=j=1,2,3 and R_{ij}=$(\tau'_{ij})/\tau_0$ for i≠j=1,2,3. Here, σ'_{11} , σ'_{22} , σ'_{33} , τ'_{12} , τ'_{13} , τ'_{23} are the yield strengths due to corresponding uniaxial loading, and σ_0 and τ_0 are reference yield normal and shear stresses. In order to obtain the constants of Hill's potential, the stress-strain responses corresponding to different uniaxial strain histories of the homogenized lamina are needed. This will provide the corresponding yield strengths. To homogenize the lamina beyond the elastic regime, the same equations corresponding to the elastic regime are extended into the inelastic regime using a series of values of secant moduli of the pure matrix material as opposed to a single value of elastic modulus. That is, $'E'_m$ of the matrix is not a single value, but a series of values $'E'_s$, where E_s is the secant modulus of the pure matrix as shown in Fig. 2.2. By substituting this series of values of $'E'_s$ in expressions for E_{11}, E_{22},G_{12},G_{23} obtained from the CCM, we obtain the corresponding series of values for these constants as a function of stress (or strain), based on the

assumption of stress based or strain based formulation of the CCM methodology. Here, E_{11}(fiber dominated) is strain based, and E_{22},G_{12} and G_{23}(matrix dominated) are stress based calculations. This implies that matrix dominated properties are expressed as a function of stress, while fiber dominated properties are expressed as a function of strain. The stress-strain response corresponding to the above properties are then constructed. From these stress-strain responses, the yield strength in tension and shear along each direction and each plane, respectively, are obtained. The 2-direction is taken to be the reference direction. Therefore, $\sigma_0 = \sigma'_{22}$. The constants F, G, H, N, M and L defined above are determined, and used in Hill's plasticity potential available in ABAQUS (*ABAQUS* (6.10)). It should be noted that plasticity is one of the many ways to approximate nonlinearity of the matrix material, and is chosen in the present study.

2.4 Upscaled Laminate Model

The upscaled homogenized model consists of 8-layers of laminae (see Fig. 2.7), where the off-axis layers i.e. -45^0,45^0,90^0 layers are homogenized using the technique mentioned in the previous section. Here, the red, cream and blue regions are the homogenized -45, +45 and 90 degree laminae. Micro-mechanics is maintained in the 0^0 layers, as they are the load bearing layers and are responsible for kink band formation in multidirectional laminates. Therefore, the regions in green are the 0 degree fibers, and regions in grey are the matrix in 0 degree lamina. The imperfections imparted, boundary conditions and loading applied are identical to the discrete fiber-matrix model explained before.

The homogenized elastic lamina properties of the off-axis laminae corresponding to a volume fraction of 0.49 and the constituent material properties (Table 2.1 and Fig. 2.2), are given in Table 2.2. The constants R_{ij} required to calculate the potential constants of Hill's plasticity are tabulated in Table 2.3 (note that R_{11} is chosen to

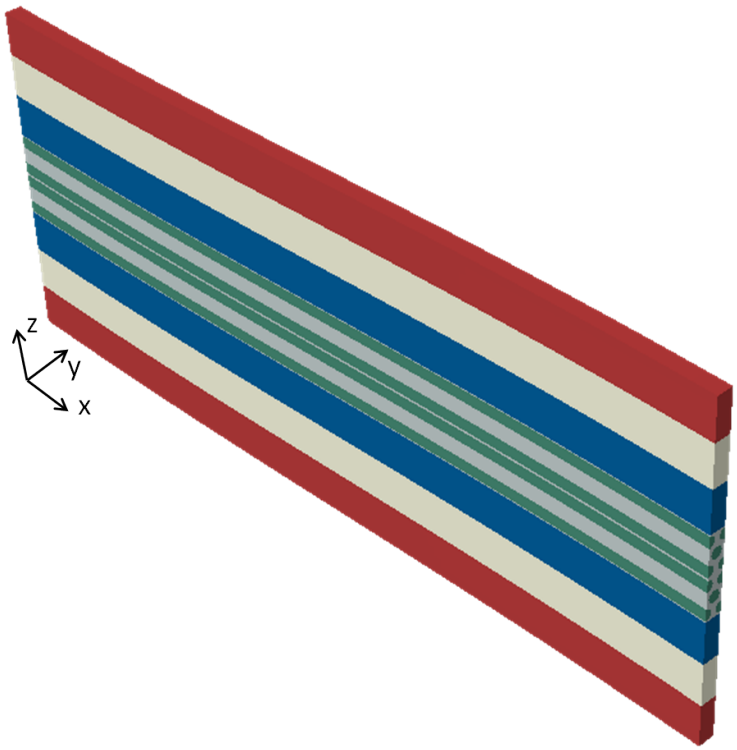

Figure 2.7: 8-layered 3-D finite element model of the laminate with homogenized off-axis laminae

be an arbitrarily high value since the 1-direction of the lamina is assumed to be elastic throughout due to very high E_{11} of the fibers, and hence does not possess a finite yield strength). These properties are applied to off-axis laminae in their rotated coordinates accounting for their ply orientations.

Table 2.2: Elastic homogenized lamina properties

E_{11}(GPa)	E_{22}(GPa)	E_{33}(GPa)	G_{12}(GPa)	G_{13}(GPa)	G_{23}(GPa)	ν_{12}	ν_{13}	ν_{23}
136.8	5.4	5.4	2.5	2.5	1.7	0.42	0.42	0.57

Table 2.3: Values of R_{ij} for calculating Hill's potential constants

R_{11}	R_{22}	R_{33}	R_{12}	R_{13}	R_{23}
18876.5	1.0	1.0	0.95	0.95	1.15

With the values of Hill's potential constants and lamina elastic properties determined, a plot showing the axial, transverse, and shear responses of a homogenized ply

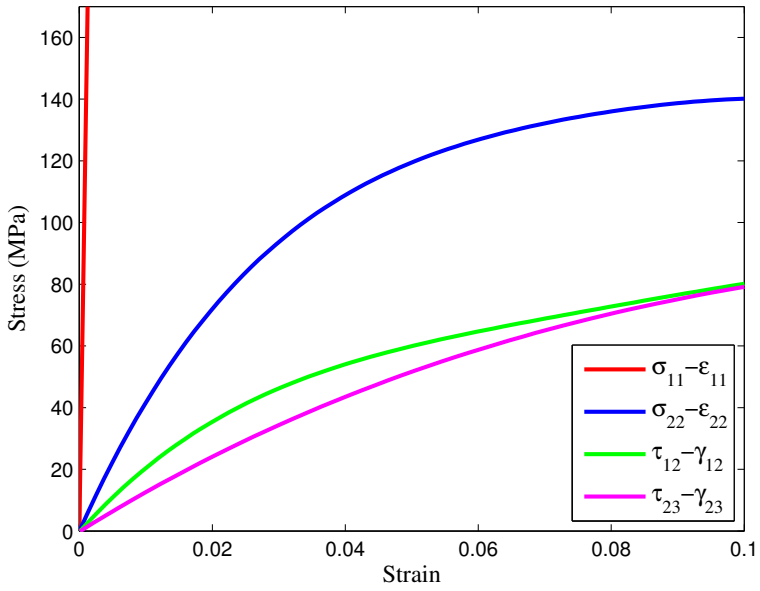

Figure 2.8: Stress-strain responses of a homogenized ply

is shown in Fig. 2.8. It is observed that the response in the axial direction is linear since it depends on the axial stiffness of the fibers, which is very high compared to the stiffness of matrix. The transverse and shear responses are non-linear due to the elasto-plasticity of the matrix.

An imperfection sensitivity analysis similar to that of the discrete fiber-matrix model is carried out here. The stress-strain response of the laminate subjected to compressive loading corresponding to imperfection angles of 1^0, 1.5^0 and 2^0 are plotted in Fig. 2.9. The initial stiffness is approximately 48.3 ± 0.2 GPa and the peak stresses are in a range 536-687 MPa.

2.5 Comparison of Discrete Fiber-matrix Model with the Upscaled Semi-homogenized Model

The deformation plots of both the discrete fiber-matrix model and the upscaled semi-homogenized model are plotted in Fig. 2.11 and Fig. 2.12, with an initial imperfection angle of 1.0^0, at different loading stages. The contours represent the equivalent

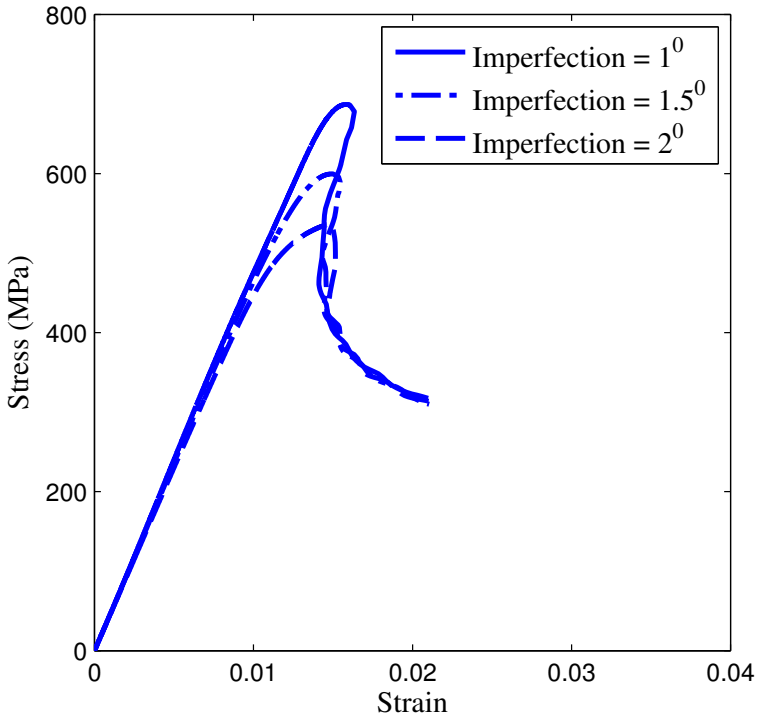

Figure 2.9: Global compressive stress-strain response of the semi-homogenized model

stress (defined as $\sqrt{\frac{3}{2}S:S}$, where S is the deviatoric stress tensor) in the laminates. In order to compare the global stress-strain response more closely, the global stress-strain responses of both the models corresponding to an imperfection of 1^0 are shown in Fig. 2.10. It is observed that the initial linear stiffnesses match well, and the peak stresses are comparable. The percentage difference in peak stress values vary between 2-4 % for different imperfections.

A further discussion on the kink band formation in the two models is presented here. In Fig. 2.11, the model appears to form a kink band at and after the peak load, along with micro-buckling of the 0^0 fibers. In Fig. 2.12, micro-buckling of 0^0 fibers is also observed in 0^0 layers, as they are the primary load bearing laminae. In either case, failure by kinking is captured, though the post peak snap back behavior in the fiber-matrix model is more gradual than in the semi-homogenized model. This can be attributed to the homogenized off-axis layers, which impart relatively more

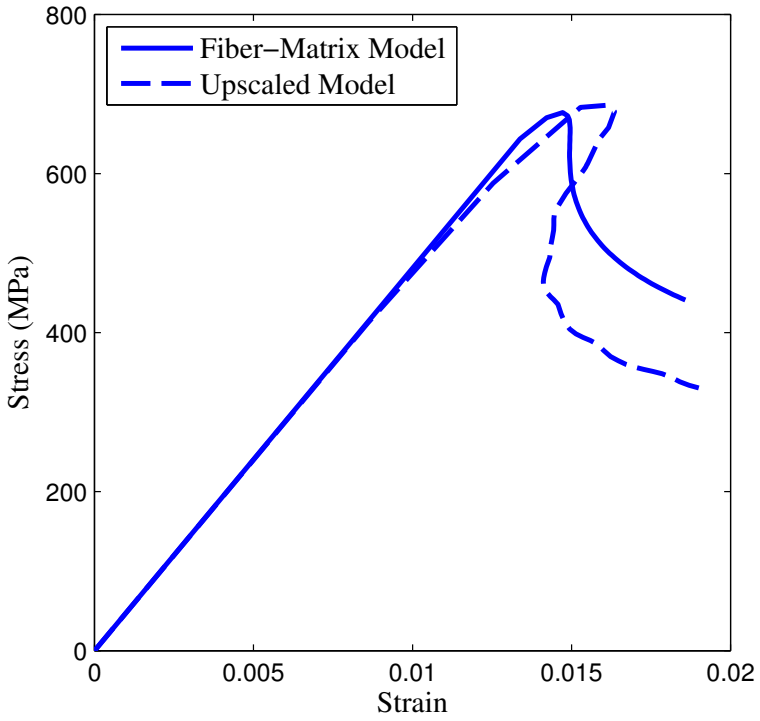

Figure 2.10: Global stress-strain response of both discrete fiber-matrix and upscaled models with an initial imperfection of 1^0

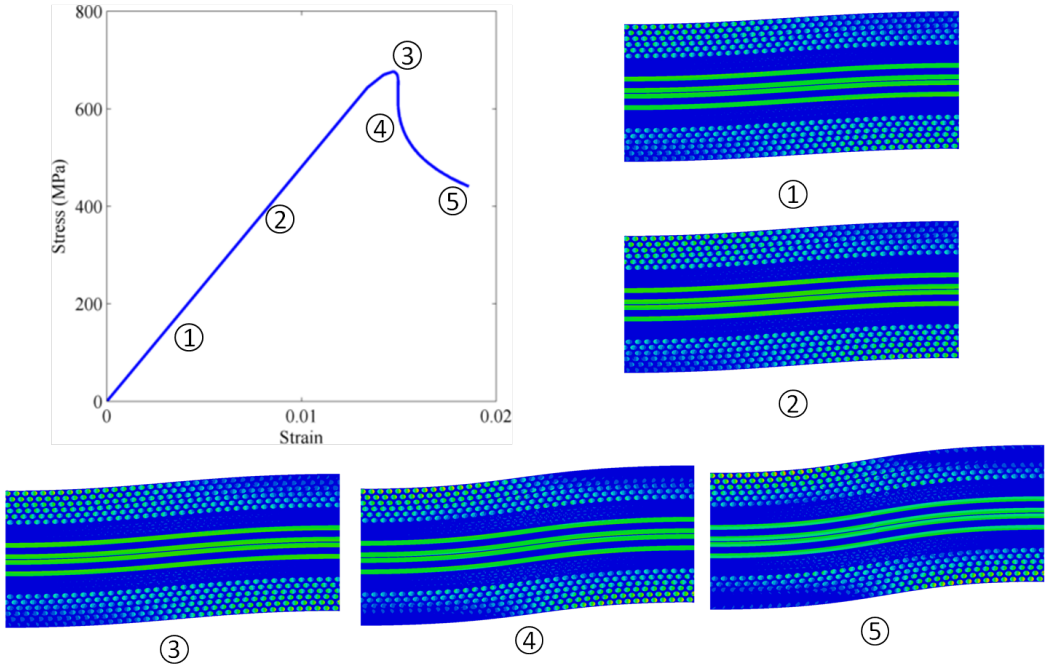

Figure 2.11: Global stress-strain response with deformation plots at different loading stages of the discrete fiber matrix model

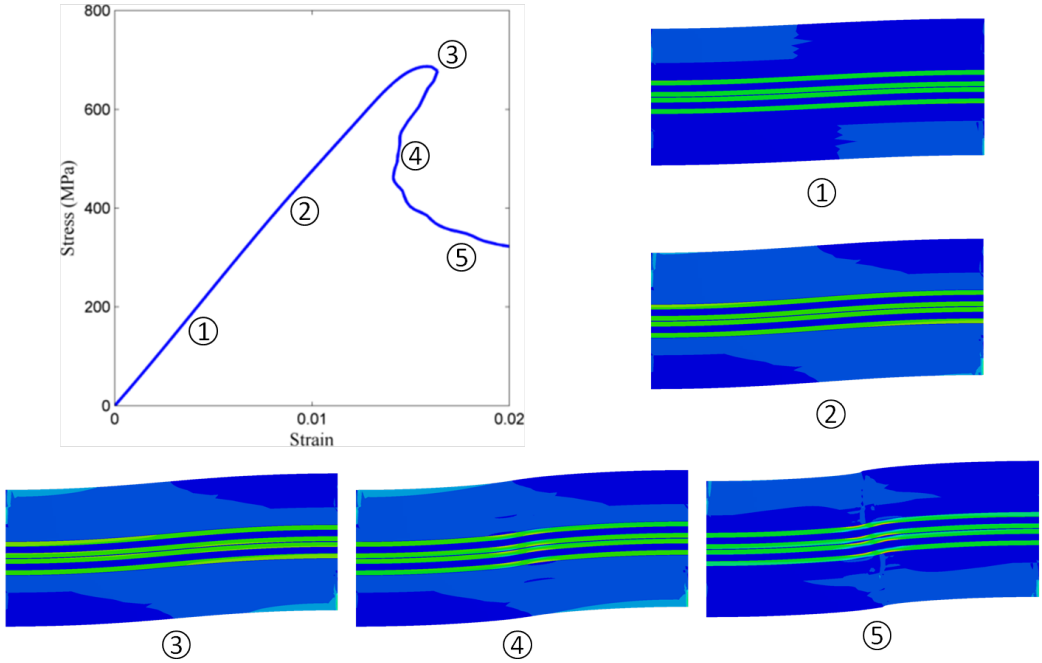

Figure 2.12: Global stress-strain response with deformation plots at different loading stages of the semi-homogenized model

constraint on the 0 degree layers making the kink-bank width more localized than in the discrete fiber matrix model(refer to Fig. 2.11 and Fig. 2.12). Hence, this shows that the upscaling method introduced here leads to a practical engineering approach to predict the compressive strength allowable, that is traditionally obtained by tests (discussed in detail in Chapter V), and predicted here using basic material response data and the fiber volume fraction.

Also, contour plots of equivalent plastic strains in the two models are plotted in Fig. 2.13 and Fig. 2.14. From the two figures, it is observed that significant plastic strain appears in the two model after the peak stress is reached. Therefore, nonlinearity in the two models occur in the post peak regime only. This implies that the approximation of nonlinearity of the matrix and off-axis layers using plasticity is valid for predicting the compressive strength of laminates.

2.6 Conclusions

An upscaled semi-homogenizing method was formulated and presented in this chapter using deformation plasticity theory along with the Hill's anisotropic plasticity model to establish a model to predict the compressive strength allowable for composite laminates, dominated by kink banding failure. This model, as mentioned above, will be used in Chapter V to study failure mode interaction between kink band formation and delamination by introducing delamination capability to the model. The inputs to this method are the elastic properties of fiber and matrix, along with the nonlinear elastic-plastic shear response of the matrix. An 8-layer laminate was semi-homogenized (homogenizing off-axis layers, while retaining micro-mechanics of the 0^0 layers) using the method, and was compared against a discrete fiber-matrix rendition of the laminate. It was observed that the semi-homogenizing method predicts the initial linear stiffness accurately, and the predicted compressive strengths fall in the range of that predicted by the discrete fiber-matrix model. The snap back behavior in the global stress-strain response, which is characteristic of a kink banding driven failure, was also captured fairly accurately by the semi homogenized model for smaller imperfection angles imparted to the model. Therefore, this method is useful for modeling larger laminates, without having to account for the individual fibers in the off-axis laminae, yet being able to obtain the compressive response within a satisfactory limit.

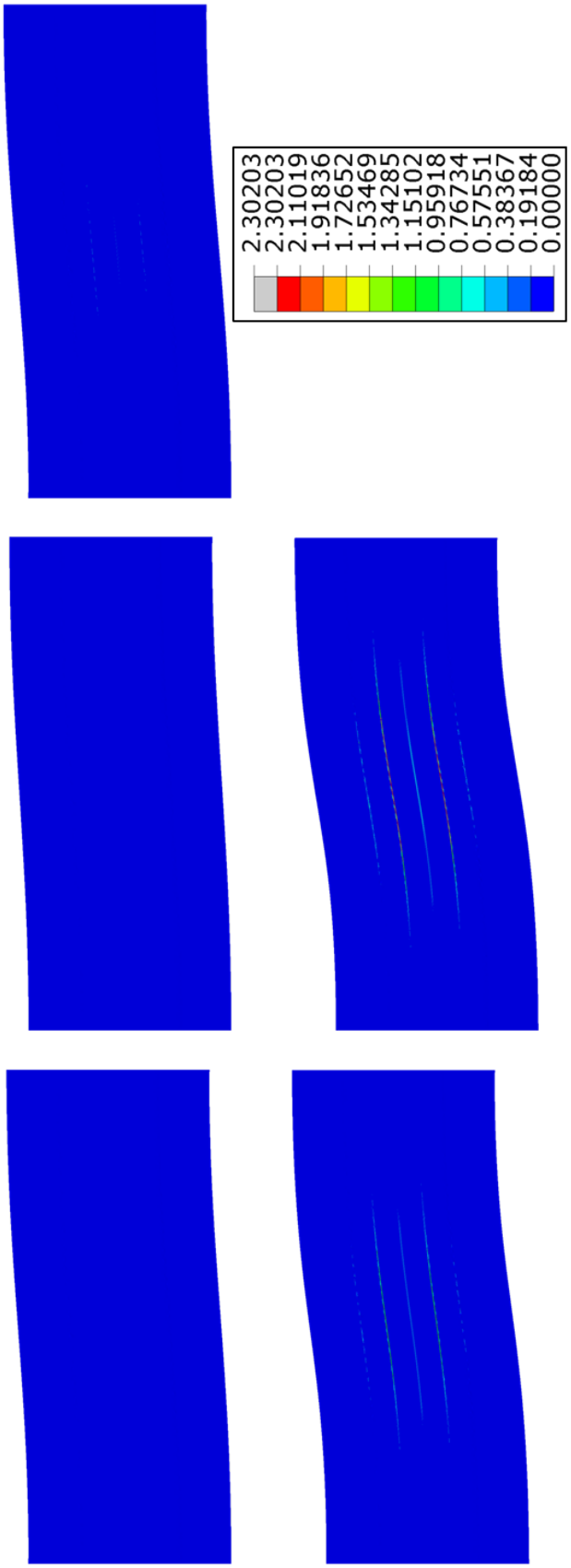

Figure 2.13: Equivalent plastic strains at different loading stages of the discrete fiber matrix model

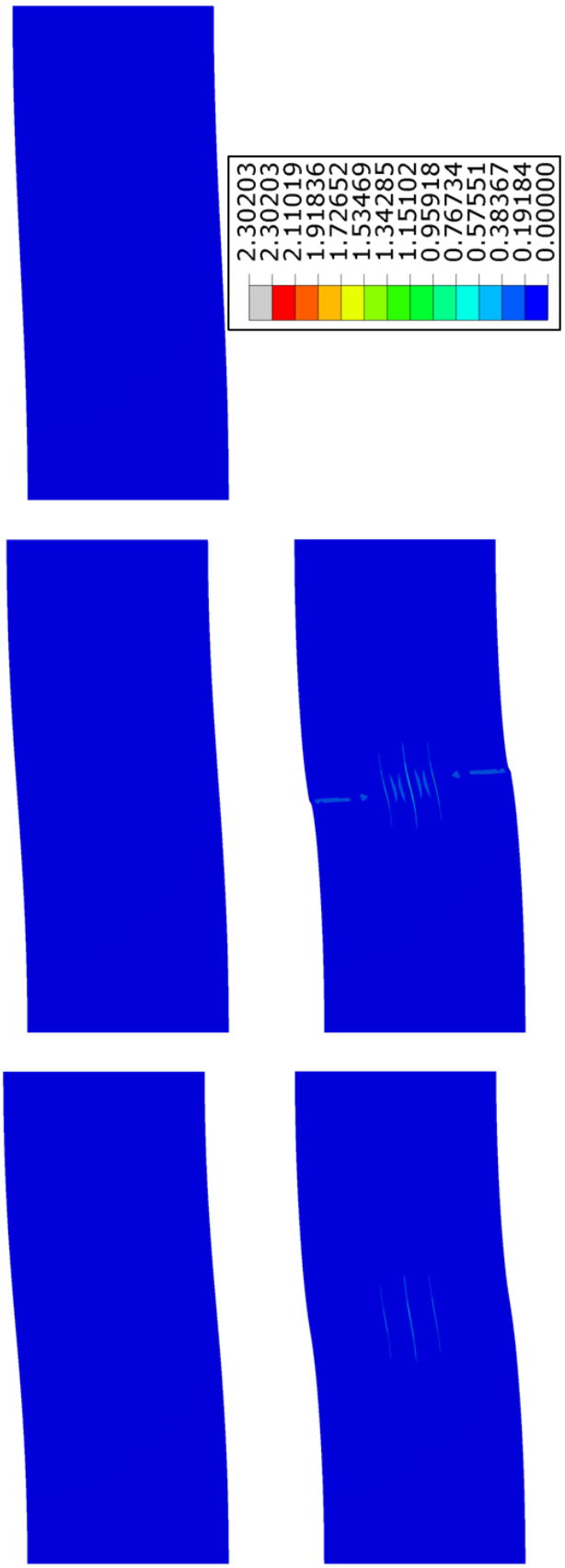

Figure 2.14: Equivalent plastic strains at different loading stages of the semi-homogenized model

CHAPTER III

Interface Analysis of Multidirectional Laminates

3.1 Introduction

Free edge effects are dominant in multidirectional laminates, and lead to a very high inter-laminar stresses causing pre-mature failure. Therefore, the determination of the interfaces with very large inter-laminar stresses a-priori is very important for delamination driven failure. By doing so, the interfaces most susceptible to delamination are determined, and the model can be allowed to delaminate along those interfaces only, thereby reducing the complexity of the model as compared to the one with delamination capability along each interface in the laminate.

So, what are free edge effects, and how are they experimentally observed?

Fig. 3.1 shows a free edge in a specimen subjected to loading. Due to drastic changes in the material properties depending on the orientation of fibers in different lamina, significant stress concentrations appear at these free edges. This can be observed as Moire fringe patterns on the surface of free edges through the thickness of the laminate. These fringes display drastic change in the fringe pattern implying high strain gradients, which indicate high stresses at the interfaces. Fig. 3.2 shows an example of high strain gradients in laminates with $+\theta/-\theta$ stacking.

After developing the upscaled laminate model given in Chapter II, the interface within the laminate most susceptible to delamination needs to be determined in order

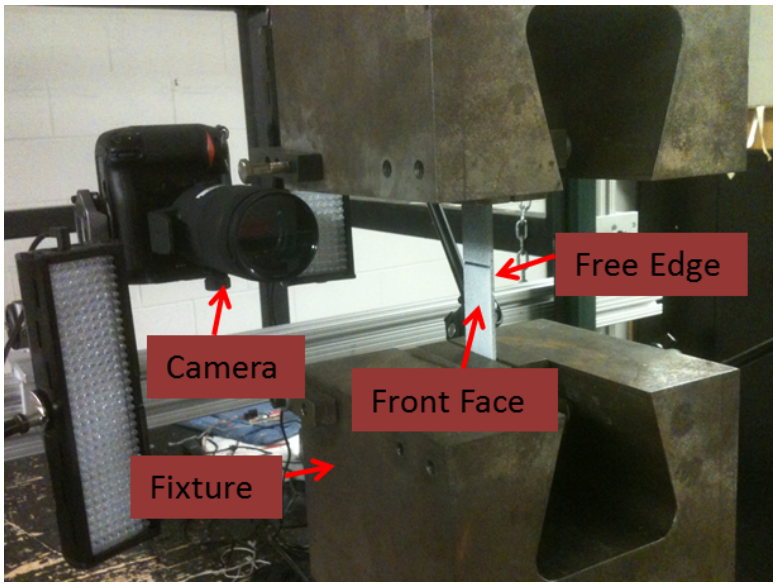

Figure 3.1: Illustration of free edge

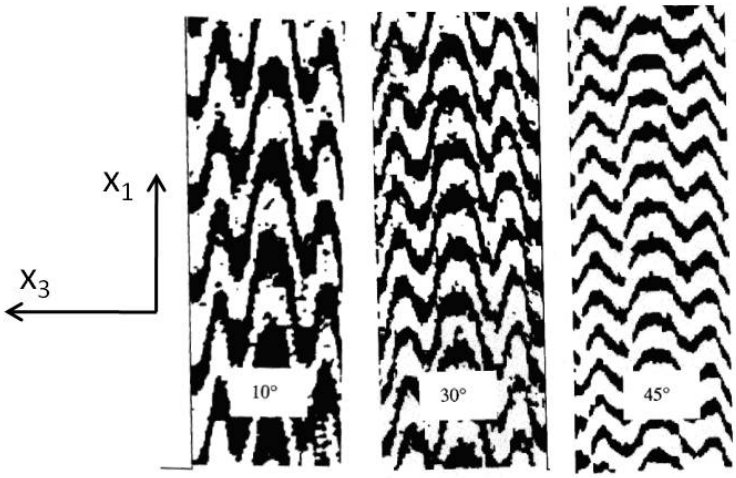

Figure 3.2: Moire fringes of free edge in multidirectional laminates (*Herakovich* (1998))

to add interface elements along that interface. Towards this end, a generalized 2-D formulation in the FEM framework is derived as explained in the following section.

3.2 Mathematical Formulation

Based on the formulation given in *Pipes and Pagano* (1970), and *Martin et al.* (2012), a laminate of length $2L$, width of $2b$ and lamina thickness equal to h is

considered. The geometry of the laminate along with its boundaries is shown in Fig. 3.3. The layers in the laminate are in the x_1-x_2 plane. A compressive load is applied at the edges Σ_{+L} and Σ_{-L} along the x_1 direction. Edges Σ_0 and Σ_{2b} are the free edges in the x_2 direction.

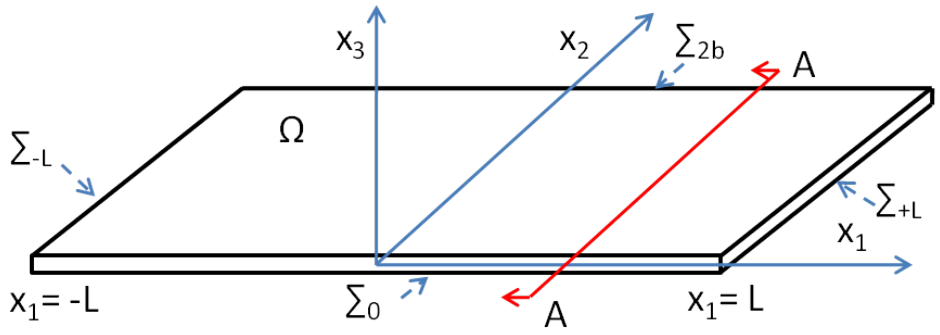

Figure 3.3: 3-D laminate

A cross-section of the laminate at A-A is shown in Fig. 3.4 that has N layers through the thickness. The p^{th} interface between the laminae is represented by Γ^p. At a region considerably far from the loading edges, the stress components are assumed to be independent of x_1. That is, the axial strain ϵ_{11} is assumed to be uniform along the x_1-direction within the laminate. This behavior was reported in *Pipes and Daniel* (1971) through Moire fringe patterns on the surfaces in the x_1-x_2 plane of different laminates, as shown in Fig. 3.5.

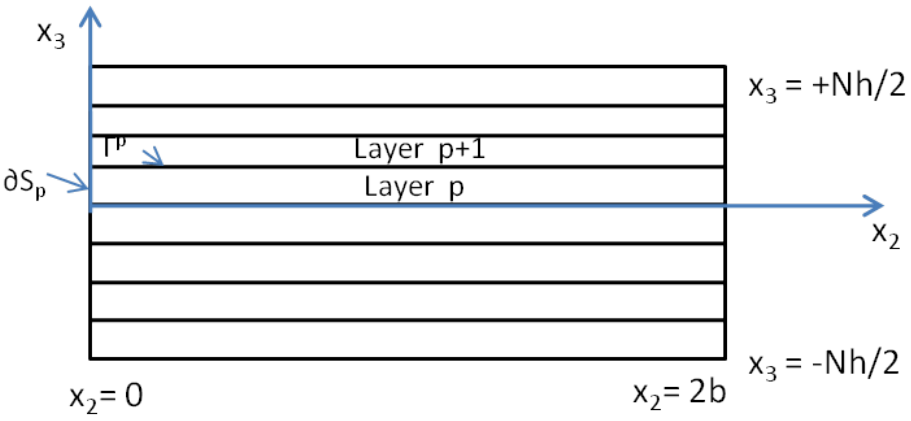

Figure 3.4: Cross-section of the 3-D laminate

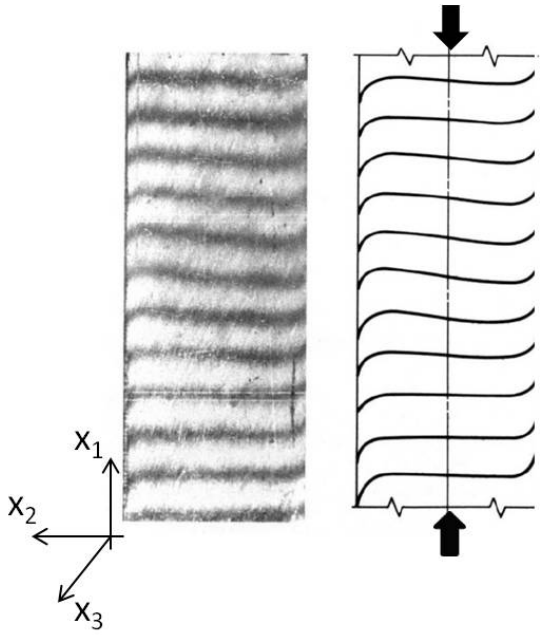

Figure 3.5: Moire fringe pattern on the surface of a 16-ply graphite-epoxy laminate (*Pipes and Daniel* (1971))

Thus, the displacement field assumes the following form,

$$\begin{aligned} U_1(x_1, x_2, x_3) &= \tilde{U}_1(x_2, x_3) + \epsilon_{11} x_1 \\ U_2(x_1, x_2, x_3) &= \tilde{U}_2(x_2, x_3) \\ U_3(x_1, x_2, x_3) &= \tilde{U}_3(x_2, x_3) \end{aligned} \tag{3.1}$$

Here, ϵ_{11} is the applied uniform axial strain in the laminate in the x_1-direction. The strains are determined as,

$$\epsilon_{ij} = \frac{1}{2}\left(\frac{\partial U_i}{\partial x_j} + \frac{\partial U_j}{\partial x_i}\right) \tag{3.2}$$

for $i = 1, 2, 3$.

Therefore, the corresponding strain field is given by,

$$\begin{aligned}
\epsilon_{11} &= \frac{1}{2}(\frac{\partial U_1}{\partial x_1} + \frac{\partial U_1}{\partial x_1}) \Longrightarrow \epsilon_{11} = \epsilon_{11} \\
\epsilon_{22} &= \frac{1}{2}(\frac{\partial U_2}{\partial x_2} + \frac{\partial U_2}{\partial x_2}) \Longrightarrow \epsilon_{22} = \frac{\partial \tilde{U}_2}{\partial x_2} \\
\epsilon_{33} &= \frac{1}{2}(\frac{\partial U_3}{\partial x_3} + \frac{\partial U_3}{\partial x_3}) \Longrightarrow \epsilon_{33} = \frac{\partial \tilde{U}_3}{\partial x_3} \\
\epsilon_{12} &= \frac{1}{2}(\frac{\partial U_1}{\partial x_2} + \frac{\partial U_2}{\partial x_1}) \Longrightarrow 2\epsilon_{12} = \frac{\partial \tilde{U}_1}{\partial x_2} + \frac{\partial \tilde{U}_2}{\partial x_1} \Longrightarrow \gamma_{12} = \frac{\partial \tilde{U}_1}{\partial x_2} \\
\epsilon_{13} &= \frac{1}{2}(\frac{\partial U_1}{\partial x_3} + \frac{\partial U_3}{\partial x_1}) \Longrightarrow 2\epsilon_{13} = \frac{\partial \tilde{U}_1}{\partial x_3} + \frac{\partial \tilde{U}_3}{\partial x_1} \Longrightarrow \gamma_{13} = \frac{\partial \tilde{U}_1}{\partial x_3} \\
\epsilon_{23} &= \frac{1}{2}(\frac{\partial U_2}{\partial x_3} + \frac{\partial U_3}{\partial x_2}) \Longrightarrow 2\epsilon_{23} = \frac{\partial \tilde{U}_2}{\partial x_3} + \frac{\partial \tilde{U}_3}{\partial x_2} \Longrightarrow \gamma_{23} = \frac{\partial \tilde{U}_2}{\partial x_3} + \frac{\partial \tilde{U}_3}{\partial x_2}
\end{aligned} \tag{3.3}$$

It is noted that the strain field is independent of x_1. The constitutive law for each linear elastic lamina (3-D), in tensorial form, yields the corresponding stress field :

$$\sigma_{ij} = a_{ijkl}\epsilon_{kl} \tag{3.4}$$

where, i,j=1,2,3 within the laminate. Here, a_{ijkl}, is the fourth order linear elasticity tensor for a general anisotropic material. At the interface, we must ensure displacement and traction continuity, which are given by,

$$\begin{aligned}
\text{Displacement} \quad \text{Continuity} : \quad & [[U_i]] = 0 \\
\text{Traction} \quad \text{Continuity} : \quad & [[\sigma_{ij} n_j]] = 0 \quad \text{on} \quad \text{the} \quad \text{interface} \quad \Gamma^k
\end{aligned} \tag{3.5}$$

At the traction free edges we have,

$$\sigma_{ij} n_j = 0 \quad \forall \quad i,j = 1,2,3 \quad \text{on} \quad \Sigma_0 \quad \text{and} \quad \Sigma_{2b} \tag{3.6}$$

and the boundary conditions at the loading edges are,

$$\begin{aligned} \sigma_{ij} n_j &= -F_i \quad \text{on} \quad \Sigma_{+L} \\ \sigma_{ij} n_j &= F_i \quad \text{on} \quad \Sigma_{-L} \end{aligned} \tag{3.7}$$

The derivation of the weak form in the FEM framework follows. Let V be a kinematically admissible displacement field for the equilibrium equations, given by,

$$V = \begin{pmatrix} V_1(x_2, x_3) \\ V_2(x_2, x_3) \\ V_3(x_2, x_3) \end{pmatrix} \tag{3.8}$$

The weighted average of the equilibrium equations to determine the weak form are,

$$\int_{\Omega} \frac{\partial \sigma_{ij}}{\partial x_j} V_i d\Omega = 0, \quad \forall V_i \quad \text{for} \quad \text{i, j} = 1, 2, 3 \tag{3.9}$$

Applying divergence theorem to the above equation yields,

$$\begin{aligned} &\int_{\Omega} \sigma_{ij} \frac{\partial V_i}{\partial x_j} d\Omega - \int_{\Sigma_L} \sigma_{ij} n_j dS = 0 \\ &\implies \int_{\Omega} \sigma_{ij} \frac{\partial V_i}{\partial x_j} d\Omega - \int_{\Sigma_{+L}} F_i V_i dS + \int_{\Sigma_{-L}} F_i V_i dS = 0 \\ &\implies \int_{\Omega} \sigma_{ij} \frac{\partial V_i}{\partial x_j} d\Omega = 0, \quad \forall V_i \quad \text{for} \quad \text{i, j} = 1, 2, 3 \end{aligned} \tag{3.10}$$

From the assumption of admissible displacement field of V, i.e. since V does not depend on x_1, we have $V = f(x_2, x_3) \implies \frac{\partial V_i}{\partial x_1} = 0$. Therefore,

$$\int_{\Omega} \sigma_{i\alpha} \frac{\partial V_i}{\partial x_\alpha} d\Omega = 0, \quad \forall V_i \quad \text{for} \quad \text{i} = 1, 2, 3; \alpha = 2, 3 \tag{3.11}$$

Substituting the constitutive relation(3.4) into the above equation gives,

$$\Longrightarrow \int_{\Omega} a_{i\alpha kh} \frac{\partial U_k}{\partial x_h} \frac{\partial V_i}{\partial x_\alpha} d\Omega = 0, \quad \forall V_i \quad \text{for} \quad \text{i, k, h} = 1, 2, 3; \alpha = 2, 3 \tag{3.12}$$

Using the displacement field assumption given in Equation 3.1, we have,

$$\Longrightarrow \int_{\Omega} a_{i\alpha kh} \frac{\partial \tilde{U}_k}{\partial x_h} \frac{\partial V_i}{\partial x_\alpha} d\Omega + \epsilon_{11} \int_{\Omega} a_{i\alpha 11} \frac{\partial V_i}{\partial x_\alpha} d\Omega = 0, \quad \forall V_i \quad \text{for} \quad \text{i, k, h} = 1, 2, 3; \alpha = 2, 3 \tag{3.13}$$

where ϵ_{11} is the global strain applied in the x_1 direction.

Dividing the volume integral into two integrals, one along the x_1-direction, and the other in the plane of the cross-section (x_2-x_3), we have,

$$\begin{aligned} &\Longrightarrow \int_{-L}^{+L} \int_{S} a_{i\alpha kh} \frac{\partial \tilde{U}_k}{\partial x_h} \frac{\partial V_i}{\partial x_\alpha} dx_1 dx_2 dx_3 + \epsilon_{11} \int_{-L}^{+L} \int_{S} a_{i\alpha 11} \frac{\partial V_i}{\partial x_\alpha} dx_1 \underline{d} x_2 dx_3 = 0 \\ &\Longrightarrow \int_{-L}^{+L} dx_1 \int_{S} a_{i\alpha kh} \frac{\partial \tilde{U}_k}{\partial x_h} \frac{\partial V_i}{\partial x_\alpha} dx_2 dx_3 + \epsilon_{11} \int_{-L}^{+L} dx_1 \int_{S} a_{i\alpha 11} \frac{\partial V_i}{\partial x_\alpha} dx_2 dx_3 = 0 \end{aligned} \tag{3.14}$$

Carrying out the integral along the x_1-direction,

$$2L[\int_{S} a_{i\alpha kh} \frac{\partial \tilde{U}_k}{\partial x_h} \frac{\partial V_i}{\partial x_\alpha} dx_2 dx_3 + \epsilon_{11} \int_{S} a_{i\alpha 11} \frac{\partial V_i}{\partial x_\alpha} dx_2 dx_3] = 0 \tag{3.15}$$

Rearranging the terms in the above equation gives,

$$\int_{S} a_{i\alpha kh} \frac{\partial \tilde{U}_k}{\partial x_h} \frac{\partial V_i}{\partial x_\alpha} dx_2 dx_3 = -\epsilon_{11} \int_{S} a_{i\alpha 11} \frac{\partial V_i}{\partial x_\alpha} dx_2 dx_3 \tag{3.16}$$

Applying the divergence theorem to the R.H.S. of the above equation yields,

$$\int_{S} a_{i\alpha kh} \frac{\partial \tilde{U}_k}{\partial x_h} \frac{\partial V_i}{\partial x_\alpha} dx_2 dx_3 = -\epsilon_{11} \int_{\partial S} a_{i\alpha 11} V_i n_\alpha ds \tag{3.17}$$

where, "s" represents a coordinate that denotes the boundary ∂S, starting at the origin of the x_2-x_3 axes for the region S, and traversing in an anti-clockwise direction. Therefore, "s" is either "x_2" or "x_3" depending on the portion of the boundary being traversed. The above equation is modified to account for layers with different orientation in a multidirectional laminate as given below,

$$\sum_{p=1}^{N} \int_{S^p} a^p_{i\alpha kh} \frac{\partial \tilde{U}^p_k}{\partial x_h} \frac{\partial V^p_i}{\partial x_\alpha} dx_2 dx_3 = -\epsilon_{11} \sum_{p=1}^{N} \int_{\partial S^p} a^p_{i\alpha 11} V^p_i n^p_\alpha ds \tag{3.18}$$

Equation 3.18 is a generalized 2-D formulation which has displacement fields along the x_1, x_2 and x_3 directions, but in a 2-D (x_2-x_3 plane) domain. The input to the above formulation is the 4th order elasticity tensor of each layer of the laminate for a linear elastic material and the applied external strain. The equivalent loads calculated for a laminate are applied to the 2-D generalized representation of the laminate in the FEM model given in the next section.

3.3 Implementation of the Generalized 2-D Formulation

The above formulation can be implemented in several ways using the finite element method. The method used here is to modify a thin slice of a 3-D model to behave like a generalized 2-D model. The coordinate system used in ABAQUS is a x-y-z cartesian coordinate system which corresponds to the x_1-x_2-x_3 coordinate system used in the previous section. A 3-D model with a small thickness in the x-direction is considered as shown in Fig. 3.6.

The model is restricted from any expansion in the x-direction using multi-point constraints. This satisfies the requirement that the displacement fields are independent of the x-direction. This gives us the left hand side of equation (3.18). The external loads given by the right hand side of equation (3.18) are applied to the model on the edges in the y-z plane and the interfaces between the layers.

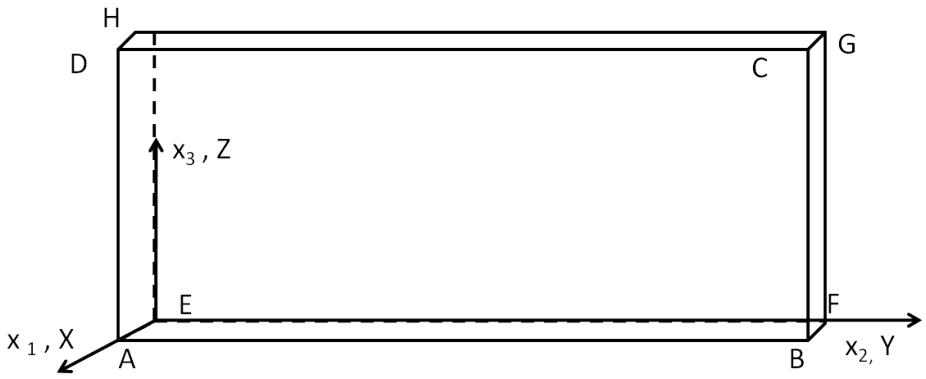

Figure 3.6: 3-D slice of a laminate

3.4 Determination of Delamination Prone Interfaces in Laminates

The current formulation is validated against two laminates with different ply stacking, and subjected to an axial (x-direction) strain. The first laminate is a $[0^0/90^0]$s laminate from *Zhang et al.* (2006) and the second is a $[+10^0/-10^0]$s laminate from *Martin et al.* (2012). The current implementation is compared against the results presented by *Zhang et al.* (2006) and *Martin et al.* (2012), and the stresses along the interfaces are found to match well. The comparison of the current implementation with *Martin et al.* (2012) is shown in Fig. 3.7.

Further, the above formulation is also implemented for an 8-ply laminate with a stacking of [-45/+45/90/0]s (half of the laminate is used as shown in Fig. 3.8) to determine the weak interfaces.

Fig. 3.9 shows the strains ϵ_{33}, ϵ_{13} and ϵ_{23} along the -45/+45 (Interface 1), +45/90 (Interface 2) and 90/0 (Interface 3) interfaces.

It is observed in Fig. 3.9 that ϵ_{13} is very high at Interface 1 as compared to the strains at the other interfaces. Therefore, Interface 1 is considered to be the interface that is most susceptible to delaminate. This information will be used in constructing the computational model of the laminate, i.e., the cohesive elements will be added

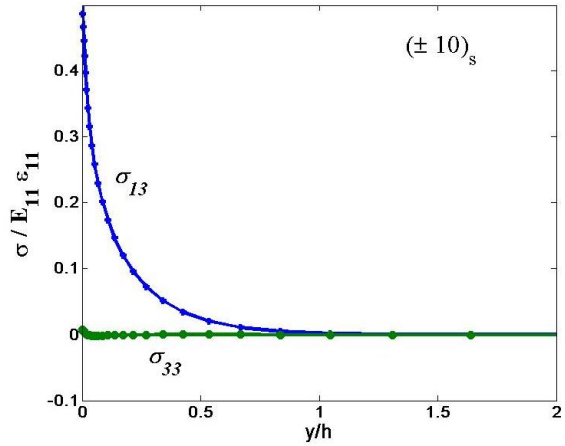

(a)

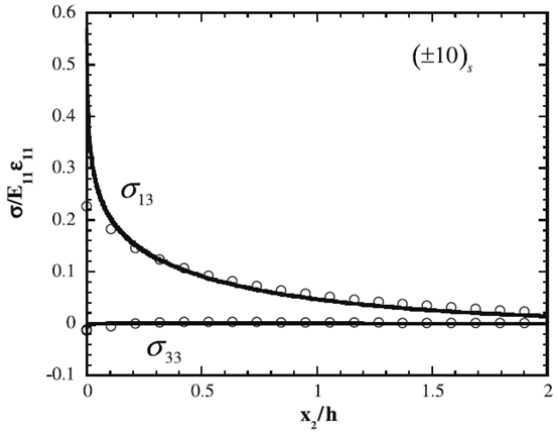

(b)

Figure 3.7: Interface stresses along +10/-10 interface in a $(\pm 10)_s$ laminate from (a) current implementation, (b) *Martin et al.* (2012)

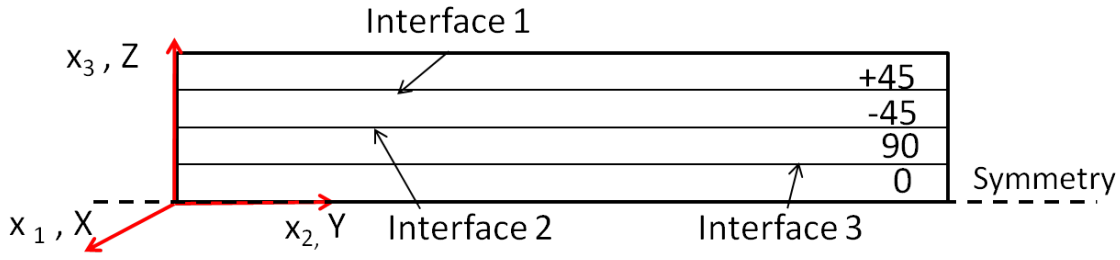

Figure 3.8: Symmetric model representing an 8-ply laminate with a stacking of $[-45/+45/90/0]_s$

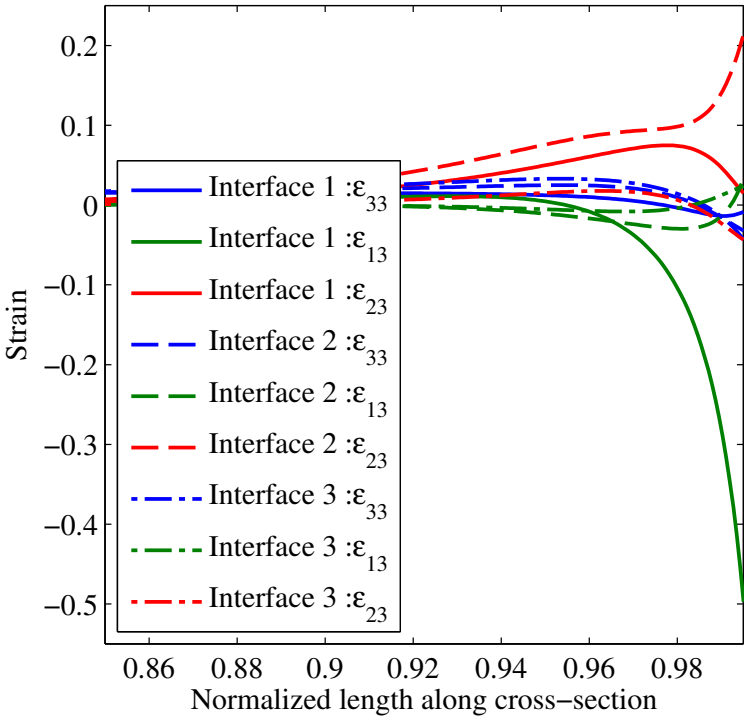

Figure 3.9: Strains at the interfaces of an 8-ply laminate model

along Interface 1 to allow for delamination at -45/+45 interfaces.

3.5 Conclusions

In this chapter, a generalized 2-D formulation to determine delamination prone interfaces in multidirectional laminates was presented. The formulation was implemented in the FEM framework using a commercially available FEM software, and validated against published results in the literature. Further, this method was used to determine the delamination prone interfaces in an 8-ply laminate with a stacking of [-45/+45/90/0]s. This result will be used in Chapter V to study the interactive failure between kinking and delamination in multidirectional laminates.

CHAPTER IV

Interface Elements : Discrete Cohesive Zone Method (DCZM) Elements

4.1 Introduction

In this chapter, interface elements to model delamination in laminates are introduced. These interface elements are added at the boundaries between different layers in the laminate. The formulation of these elements is motivated by the cohesive zone models, which can be traced back to the Barenblatt-Dugdale [*Barenblatt* (1962); *Dugdale* (1960)] model. The interface is treated as a discrete non-linear bed of 1-D elements, which are attached between adjacent node pairs of the decohering surfaces. Therefore, these elements are added between interfacial node pairs to model cohesive interactions between surfaces instead of using continuum type elements along the crack path. Further, these elements are scalable according to the mesh size, making the formulation mesh independent even in the presence of softening stiffness in the cohesive law.

4.2 DCZM Element Formulation and FEM Implementation

The discrete cohesive zone method (DCZM) element in 3D is an 8-node element connecting two free surfaces through a traction-separation law (cohesive law), repre-

sented schematically in Fig. 4.1. This interface element has zero thickness.

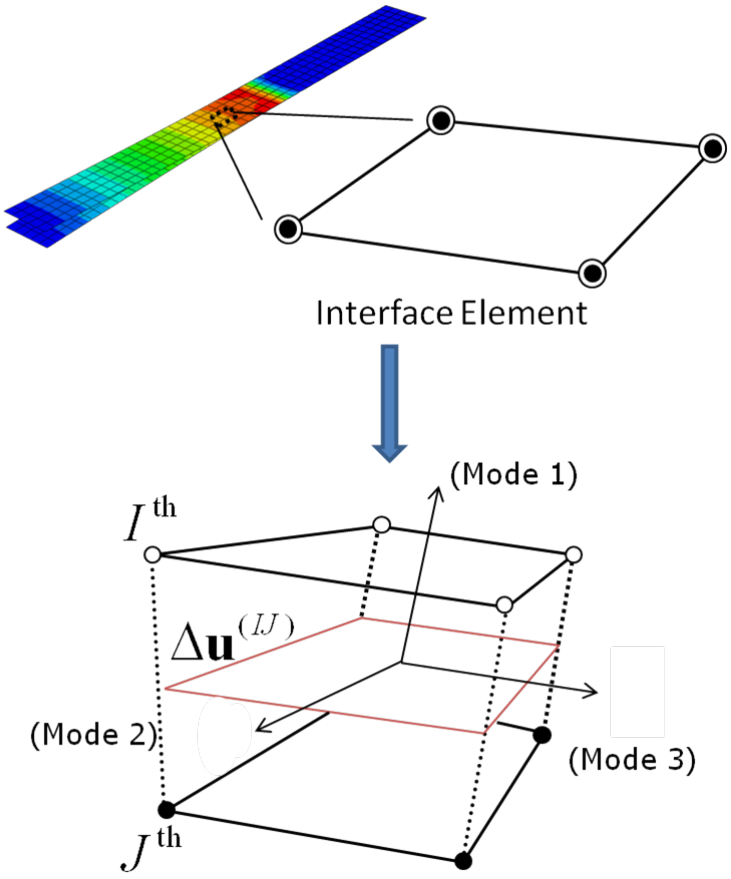

Figure 4.1: Schematic of 8-noded DCZM element in 3D

For illustration purposes, the formulation of a 4-noded DCZM element in 2D is presented here (details are given in *Gustafson* (2008)). The 3D formulation is merely an extension of the 2D formulation. The 2D DCZM element is shown in Fig. 4.2.

The stiffness matrix of the element is given by,

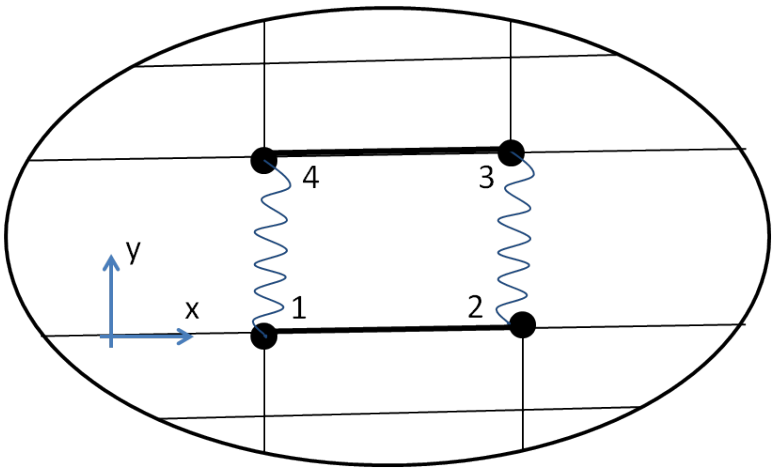

Figure 4.2: 4-noded DCZM element in 2D

$$K_{el} = \begin{bmatrix} K_{14x} & 0 & 0 & 0 & 0 & 0 & -K_{14x} & 0 \\ 0 & K_{14y} & 0 & 0 & 0 & 0 & 0 & -K_{14y} \\ 0 & 0 & K_{23x} & 0 & -K_{23x} & 0 & 0 & 0 \\ 0 & 0 & 0 & K_{23y} & 0 & -K_{23y} & 0 & 0 \\ 0 & 0 & -K_{23x} & 0 & K_{23x} & 0 & 0 & 0 \\ 0 & 0 & 0 & -K_{23y} & 0 & K_{23y} & 0 & 0 \\ -K_{14x} & 0 & 0 & 0 & 0 & 0 & K_{14x} & 0 \\ 0 & -K_{14y} & 0 & 0 & 0 & 0 & 0 & K_{14y} \end{bmatrix}$$

The corresponding force vector for an element is,

$$F_{el} = \begin{bmatrix} -F_{14x} & -F_{14y} & -F_{23x} & -F_{23y} & F_{23x} & F_{23y} & F_{14x} & F_{14y} \end{bmatrix}^T$$

The nodal displacements are,

$$u_{el} = \begin{bmatrix} u_{1x} & u_{1y} & u_{2x} & u_{2y} & u_{3x} & u_{3y} & u_{4x} & u_{4y} \end{bmatrix}^T$$

The contribution of a DCZM element to the global system of equations is,

$$[K_{el}][u_{el}] = [F_{el}] \tag{4.1}$$

Here, K_{ijk} are components of the DCZM stiffness matrix along k direction between nodes i and j. Similarly, F_{ijk} are the components of reaction force acting along the k direction between nodal pair i and j. The nodal pair relative displacements are,

$$\delta_{ijk} = u_{jk} - u_{ik} \tag{4.2}$$

That is, the relative displacement between nodal pair 1-4 along y-direction is $\delta_{14y} = u_{4y} - u_{1y}$ and along x-direction is $\delta_{14x} = u_{4x} - u_{1x}$.

The traction on the DCZM element is a function of the relative displacement between nodal pairs mentioned above. Therefore, the nodal force for opening and sliding modes are given by the traction-separation cohesive law. The traction acting between the two faces is assumed to have a triangular shape as shown in Fig. 4.3.

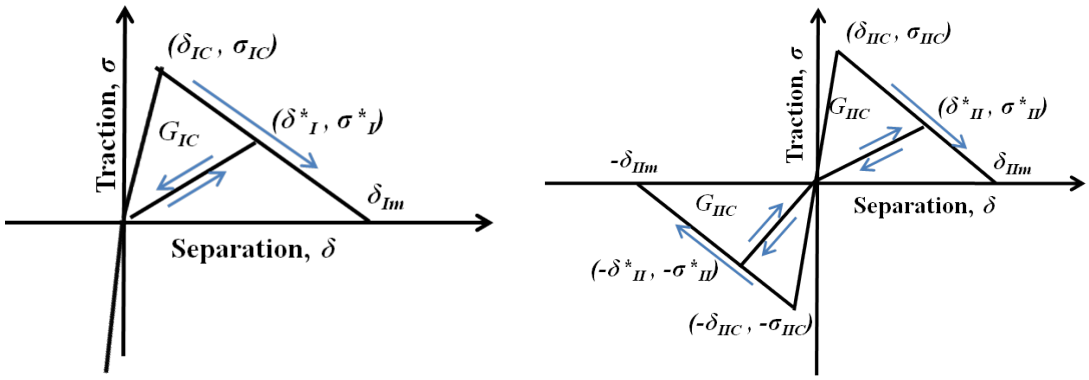

Figure 4.3: (a) Mode-I triangular cohesive law (b) Mode-II triangular cohesive law

Two traction - separation laws are used, one each for mode-I (opening) and mode-II (sliding). The mode-I cohesive law, which signifies displacement jumps perpendic-

ular to the fracture surface, in the local coordinate system is,

$$\begin{aligned}
T_1 &= \frac{\sigma_{IC}}{\delta_{IC}}\,\delta_y \quad \text{if} \quad 0 < \delta_y <= \delta_{IC} \\
T_1 &= \sigma_{IC}\left[1 - \frac{\delta_y}{\delta_{Im}}\right] \quad \text{if} \quad \delta_{IC} < \delta_y <= \delta_{Im}, \Delta\delta_y >= 0 \\
T_1 &= \bar{k}_I \delta_y \quad \text{if} \quad \delta_y > 0, \Delta\delta_y < 0 \quad \text{where,} \quad \bar{k}_I = \frac{\sigma_I^\star}{\delta_I^\star} \\
T_1 &= \sigma_{IC}\left[\frac{\delta_y}{\delta_{Im}}\right] * (factor) \quad \text{if} \quad \delta_y <= 0
\end{aligned} \tag{4.3}$$

where, "factor" is a number chosen to be three orders of magnitude larger than the largest stiffness parameter to simulate no interpenetration of the two surfaces. Similarly, the mode-II cohesive law, which signifies tangential displacement jumps, in the local coordinate system is given by,

$$\begin{aligned}
T_2 &= \frac{\sigma_{IIC}}{\delta_{IIC}}\,\delta_x \quad \text{if} \quad 0 < \delta_x <= \delta_{IIC} \\
T_2 &= \sigma_{IIC}\left[1 - \frac{\delta_x}{\delta_{IIm}}\right] \quad \text{if} \quad \delta_{IIC} < \delta_x <= \delta_{IIm}, \Delta\delta_x >= 0 \\
T_2 &= \bar{k}_{II} \delta_x \quad \text{if} \quad \delta_x > 0, \Delta\delta_x < 0 \quad \text{where,} \quad \bar{k}_{II} = \frac{\sigma_{II}^\star}{\delta_{II}^\star} \\
T_2 &= \frac{\sigma_{IIC}}{\delta_{IIC}}\,\delta_x \quad \text{if} \quad -\delta_{IIC} < \delta_x <= 0 \\
T_2 &= -\sigma_{IIC}\left[1 - |\frac{\delta_x}{\delta_{IIm}}|\right] \quad \text{if} \quad -\delta_{IIC} <= \delta_x <= 0, \Delta\delta_x < 0 \\
T_2 &= \bar{k}_{II} \delta_x \quad \text{if} \quad \delta_x <= 0, \Delta\delta_x > 0 \quad \text{where,} \quad \bar{k}_{II} = \frac{-\sigma_{II}^\star}{-\delta_{II}^\star}
\end{aligned} \tag{4.4}$$

where, δ_y and δ_x are the relative displacements in mode-I and mode-II between the nodal pair of the DCZM element, and $\Delta\delta_y$ and $\Delta\delta_x$ are the corresponding change in the relative displacements between load increments in FEM. It should be noted that the initial stiffness $\frac{\sigma_{IC}}{\delta_{IC}}$ and $\frac{\sigma_{IIC}}{\delta_{IIC}}$ are chosen to be three orders of magnitude larger than the material stiffness of the continuum element, since, ideally no separation is allowed between the nodes until the tractions exceed the critical cohesive strength

of the DCZM. The traction-separation law has two inputs in each mode, that is, the fracture toughness and the cohesive strength in mode-I, mode-II and mode-III. These are the input material properties that are determined through experiments on coupons. The next section will give details of the experiments conducted in order to determine these input properties.

4.3 Methods to Determine Input Fracture Properties

Input fracture properties are determined through experiments aided with simulations. Mode-I fracture toughness is determined through double cantilever beam (DCB) test [*ASTM(D5528)* (2007)] and mode-II fracture toughness through end notch flexure (ENF) test [*Davidson and Sun* (2006)]. Mode-I cohesive strength is inversely determined by simulating the DCB test. Similarly, Single lap joint (SLJ) test [*ASTM(D3165)* (2007)] along with the simulation of the test is used to determine the mode-II cohesive strength. It should be noted that mode-III fracture properties are assumed to be equal to mode-II fracture properties, though this may not be true for these composite materials.

4.3.1 Mode-I Fracture Toughness : Double Cantilever Beam (DCB) Test

The DCB test is a common test conducted to determine the mode-I fracture toughness in materials. This test is used here in the case of a multidirectional laminate to determine the fracture toughness of the interface between adjacent layers of a laminate. *ASTM(D5528)* (2007) is the standard for the test method to determine mode-I interlaminar fracture toughness of fiber-reinforced polymer matrix composites.

Coupons of a 16-ply laminate with stacking of $[-45_2/+45_2/90_2/0_2]_s$ were tested. The dimensions of the coupon are L = 150 mm, W = 25 mm and H = 2.5 mm. An initial horizontal slit of length $a_0 = 70$ mm is created at one of the faces as shown in Fig. 4.4. Blocks of aluminum of length (S) = 20 mm, width = 25 mm and height = 20

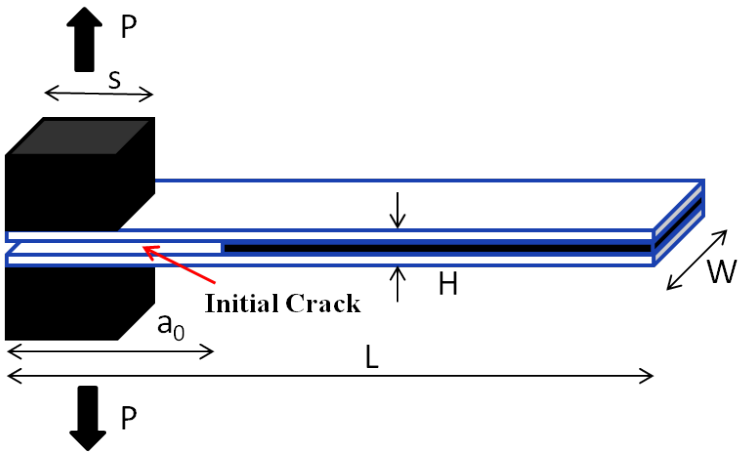

Figure 4.4: Sketch of a DCB test specimen

mm are glued to the top surface of the upper arm and the bottom surface of the lower arm of the specimen as shown in Fig. 4.4. The specimen is loaded by mounting the blocks of aluminum in the grips of the loading machine. As a displacement control load is applied, the specimen deforms in mode-I (opening mode) due to the initial slit of length a_0. As the loading is continued, the delamination grows beyond the initial length and propagates until a complete separation of the two arms is achieved. The delamination growth is measured by recording the crack tip movement at certain intervals during the test, through the inspection of a series of images.

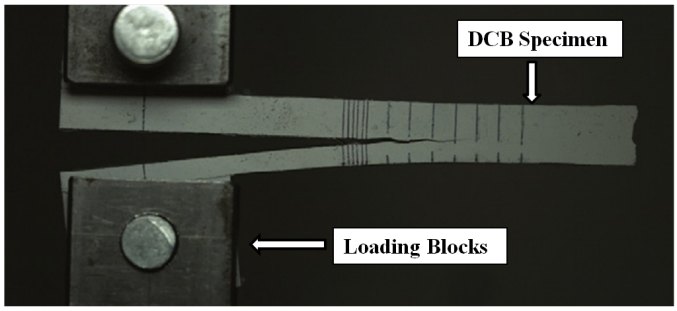

Figure 4.5: DCB test fixture

The mode-I fracture toughness is calculated using the following three methods; (1) modified beam theory (MBT), (2) compliance calibration method (CC) and (3) modified compliance calibration method (MCC). Further, fracture toughness values

obtained from a set of closed form expressions, given in *Nimmer et al.* (1996), matched well with the values determined from the ASTM standard.

4.3.1.1 Modified Beam Theory (MBT) Method

The expression for the mode-I fracture toughness (also known as strain energy release rate) for a perfectly built-in double cantilever beam using the Modified Beam Theory (MBT) Method is as follows :

$$G_{IC} = \frac{3P\delta}{2Wa} \tag{4.5}$$

where, P = load, δ = load point displacement, W = specimen width and a = delamination length.

4.3.1.2 Compliance Calibration (CC) Method

A least squares plot is generated by plotting the log $(\frac{\delta_i}{P_i})$ versus $log(a_i)$, where δ_i and P_i are the incremental load point displacement and the corresponding load, and a_i is the corresponding delamination growth of the initial slit in the specimen. a_i is measured from the images taken incrementally during the experiment by tracking the original crack tip evolution during loading. A straight line is drawn through the data points resulting in a best least-square fit. The slope $(n = \frac{\Delta(\frac{\delta_i}{P_i})}{\Delta(log(a_i))})$ of this straight line is determined. Mode-I interlaminar fracture toughness is calculated as follows:

$$G_{IC} = \frac{nP\delta}{2Wa} \tag{4.6}$$

4.3.1.3 Modified Compliance Calibration (MCC) Method

Similar to the previous section, a least squares plot of the delamination length normalized by the specimen thickness, a/h, is plotted as a function of the cube root of the compliance, $C^{1/3}$, using the values of the delamination propagation explained above.

The slope of this line is A_1. Mode-I interlaminar fracture toughness is calculated as follows :

$$G_{IC} = \frac{3P^2C^{2/3}}{2A_1Wh} \tag{4.7}$$

The fracture toughness was determined from all of the above three methods, corresponding to 4 DCB tests, and the average is calculated. A plot of the average fracture toughness versus crack (delamination) length from each of the above methods is plotted in Fig. 4.6. The value of the mode-I fracture toughness was determined to be 0.67 $\pm$ 0.07 N/mm.

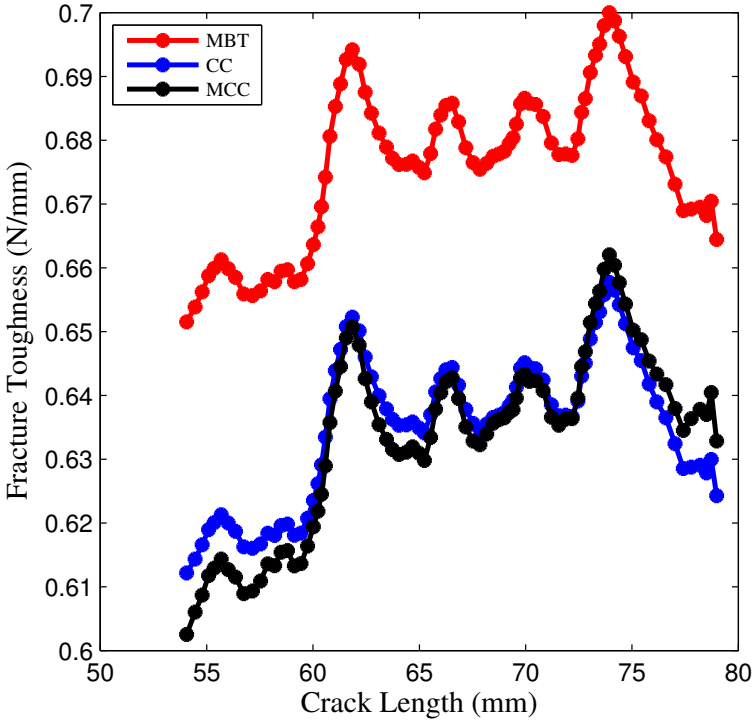

Figure 4.6: Fracture toughness versus crack length

4.3.2 Mode-I Cohesive Strength : Double Cantilever Beam (DCB) Test with Simulation

The DCB test mentioned in the previous section was simulated using the finite element method. A 2-D plane strain model of the DCB test configuration was con-

structed using 2-D bilinear quadrilateral finite elements. The aluminum blocks were modeled with perfect bonding between the blocks and the upper and the lower arms. A displacement control load was applied as shown in Fig. 4.4. The DCZM elements were added along the plane of symmetry in the model. That is, along the interface between the upper and the lower arms in a 16-ply laminate between the 0-0 plies. It is assumed that the fracture properties between all the interfaces in the laminate are comparable. The mode-I fracture toughness was fixed at 0.67 N/mm, and the mode-II and mode-III fracture properties were held fixed at very high values. The influence of mode-II and mode-III properties is minimal on the load-deflection curve due to pure mode-I fracture in a DCB test for a symmetric laminate.

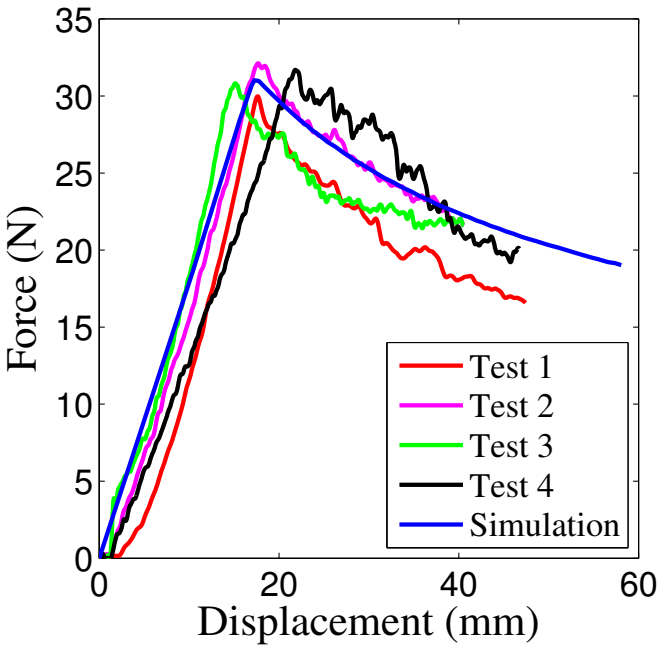

Figure 4.7: Load -deflection responses of DCB tests with simulation

The experiment was virtually carried out in ABAQUS, for a range of input values for the mode-I cohesive strength σ_{IC} (refer to Fig. 4.3(a)). The value of σ_{IC} for which the load-displacement response from the simulation matches the average load-displacement response from the DCB tests was chosen to be the mode-I cohesive strength. A plot of experimental load-displacement responses from the DCB tests,

along with the one obtained from the simulation corresponding to a σ_{IC} value of 15 MPa, are shown in Fig. 4.7. The load-displacement responses match well, and the σ_{IC} value is estimated to be equal to 15 MPa. The finite element model of the DCB specimen at an initial loading stage and at a delamination propagated stage is shown in Fig. 4.8 and Fig. 4.9, respectively.

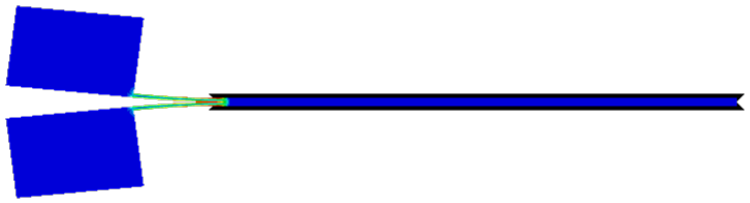

Figure 4.8: Undeformed DCB simulation

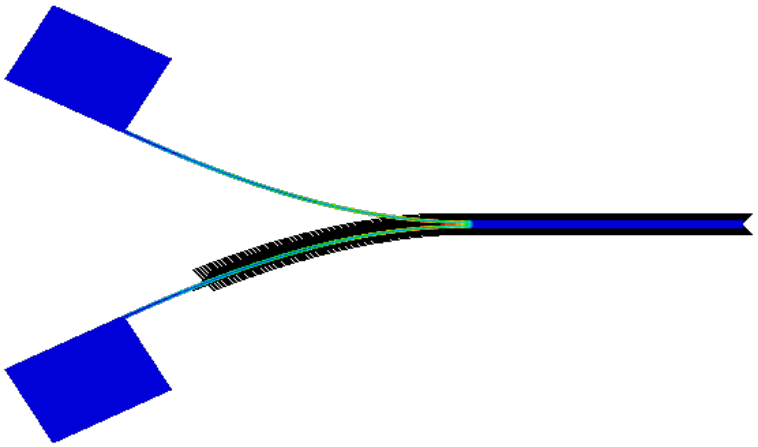

Figure 4.9: Deformed DCB simulation with opened DCZM elements

4.3.3 Mode-II Fracture Toughness : End Notch Flexure (ENF) Test

ENF tests were conducted on the 16-ply laminate to determine the mode-II cohesive strength following the procedure given in *Davidson and Sun* (2006)(since, ASTM standard for ENF test of composites does not exist). The dimensions of the ENF test specimens are as follows : length = 160 mm, width = 25 mm, height = 2.5 mm, and an initial delamination length = 30 mm.

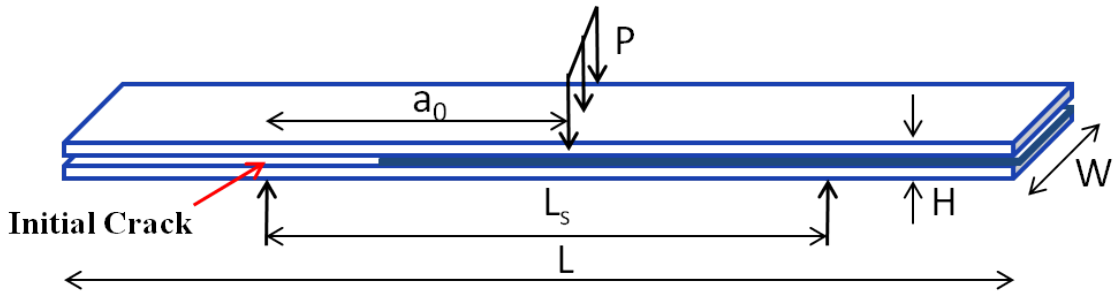

Figure 4.10: Sketch of a ENF test specimen

The ENF test is a 3-point bend test as shown in Fig. 4.11. The specimen is supported on rollers on the bottom surface, and a central vertical load is applied on the top surface. The length between the roller supports is 120 mm. An experimental setup is shown in Fig. 4.11.

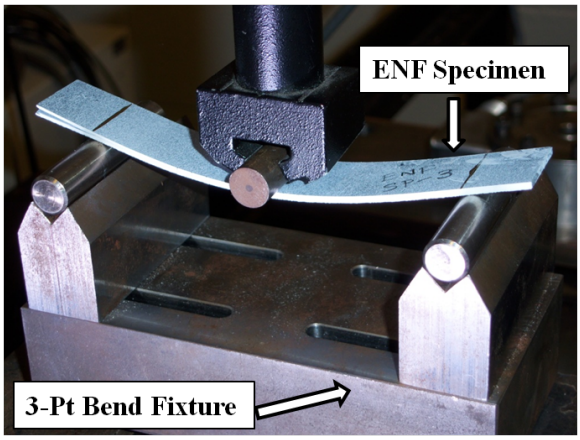

Figure 4.11: ENF test fixture

The applied load - central load point displacement responses obtained from the ENF tests conducted on 16-ply laminate are plotted in Fig. 4.12.

The specimen undergoes bending, and fails catastrophically at the peak load, with rapid crack growth along the interface, following the initial delamination path. The mode-II fracture toughness is obtained from the area under the load-displacement relation given in Fig. 4.12. The interfacial mode-II fracture toughness for these laminates was determined to be 1.67 $\pm$ 0.1 N/mm.

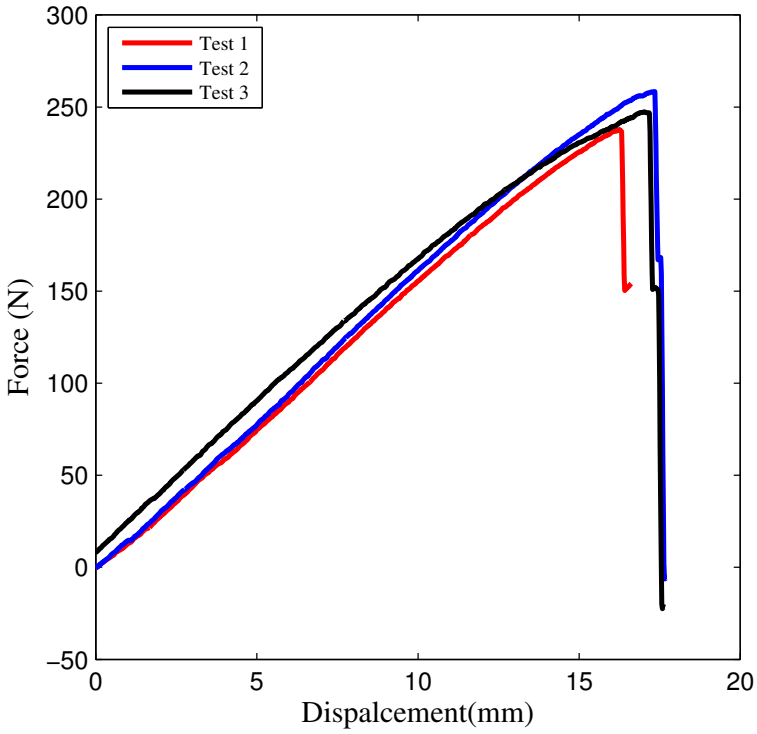

Figure 4.12: Load-load point displacement responses for ENF tests

4.3.4 Mode-II Cohesive Strength : Single Lap Joint (SLJ) Test

The fourth parameter to be determined is the mode-II cohesive strength (τ_c) of the laminate, which is determined through a single lap joint (SLJ) test [*ASTM(D3165)* (2007)]. The concept is borrowed from the SLJ test on adhesively bonded joints. Here, the laminate specimen is modified to behave like a single lap joint. The sketch of the SLJ test specimen is shown in Fig. 4.13.

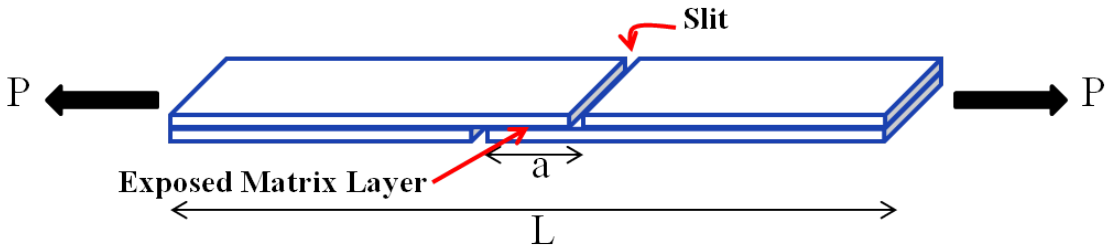

Figure 4.13: Sketch of a ENF test specimen

A slit is cut into each of the top and bottom surfaces of the coupon up to the centerline of the laminate as shown in Fig 4.13. This creates an area of pure matrix between the 0-0 layers in the laminate carrying the load. Though, the interface cohesive strength may vary between different interfaces, it is extremely difficult to determined those properties between the off-axis layers. The dimensions of the specimen are as follows : length = 190 mm, width = 17.75 mm, thickness = 4.47 mm, distance between the notches = 12.7 mm. The specimen is subjected to a tensile load as shown in Fig. 4.14.

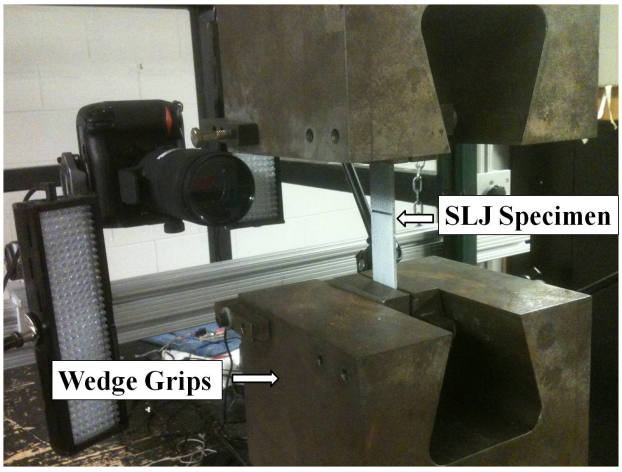

Figure 4.14: SLJ test fixture

When the SLJ specimen is subjected to tensile loading, the area between the notches carries most of the load, and at the peak load, the matrix layer between the slits ruptures creating two parts. Further, the SLJ configuration is studied using a 3-D finite element model in ABAQUS. The individual layers are modeled as homogenized elastic layers using 3-D 8-noded hexahedral elements as shown in Fig. 4.15. The DCZM elements are added at the plane between the notches along the plane of symmetry (i.e. at the interface which ruptured during the experiment) in the plane of the exposed matrix material shown in Fig. 4.15.

Further, by fixing the fracture properties already determined, i.e. G_{IC}, G_{IIC} and σ_c, the average peak load from the SLJ simulations are matched to the experimental

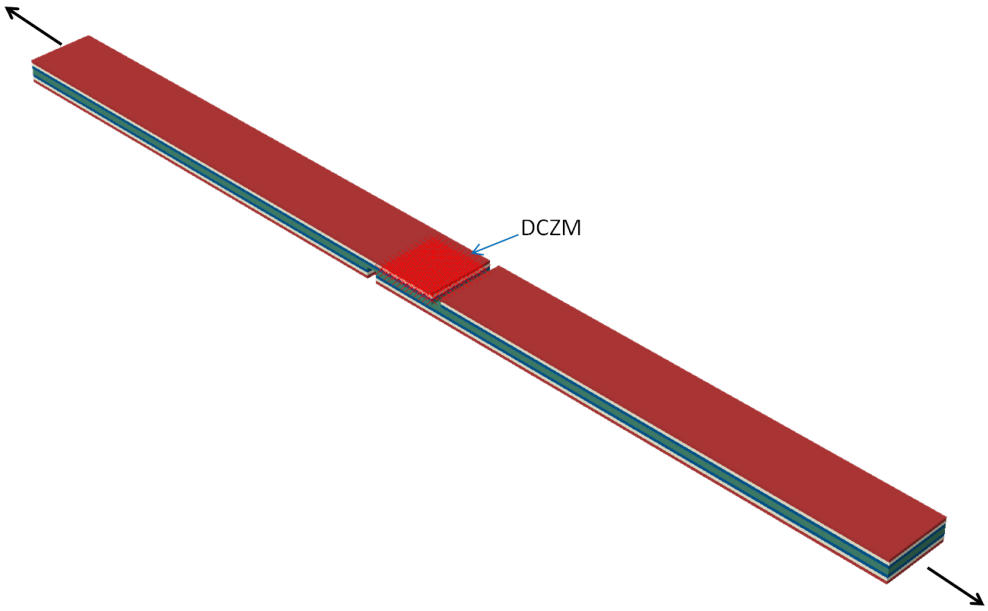

Figure 4.15: A finite element model of the SLJ test specimen

result by varying the value of τ_c in the FEM model.

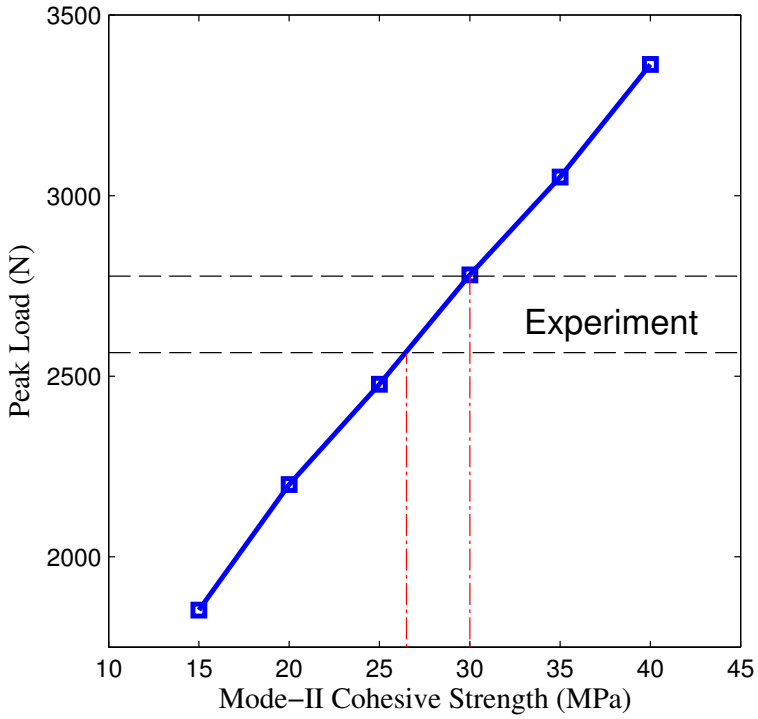

Figure 4.16: Peak load vs. mode-II cohesive strength from SLJ test simulations

The value of τ_c is varied between 15 - 40 MPa. The peak loads obtained from

the simulations are plotted against τ_c values in Fig. 4.16. The experimental range of peak loads for 4 SLJ tests correspond to a τ_c value of 28 $\pm$ 2 MPa, and are shown in Fig. 4.16.

4.4 Conclusions

In this chapter, an overview of the formulation of the DCZM elements was presented. The inputs required for these interface elements were identified as the fracture properties of the interface matrix material in the laminates. These fracture properties, which serve as inputs to the DCZM elements were determined through a combination of experiments and simulations. Therefore, the in-situ interface matrix behavior was characterized in this chapter. The DCZM elements along with the determined fracture properties will be used to model delamination in Chapter V.

CHAPTER V

Interactive Failure in Multidirectional Laminates

5.1 Introduction

In this chapter, interaction between kinking and delamination failure modes in multidirectional laminates is investigated using a set of experimental results and associated modeling studies. Two types of laminates with different stacking sequence are studied here. The first type of laminate, namely, Type A laminates, have a stacking sequence of $[-45/+45/90/0]s$, $[-45_2/+45_2/90_2/0_2]s$ and $[-45_4/+45_4/90_4/0_4]s$ with totals of 8, 16 and 32 layers, respectively. The second laminate is referred to as Type B laminate, with a stacking sequence of $[(-45/+45/90/0)_6]s$, with 48 layers. It should be noted that the zero degree layers are grouped together along the centerline in Type A laminate, whereas they are distributed in the Type B laminate. Upscaled homogenized laminate models are constructed for both types of laminates using the upscaled semi-homogenized modeling method explained in *Prabhakar and Waas* (2012b) and Chapter II. Recall that, in these models, each 0 degree lamina has hexagonally packed fibers maintaining the micro-mechanics, and the off-axis layers are homogenized using a deformation theory implementation of Hill's anisotropic plasticity theory. Interface elements formulated using the discrete cohesive zone method (DCZM) [*Gustafson and Waas* (2009)], are added at the interface between -45/+45 layers, which was in Chapter III as the delamination prone interface in the laminate,

via a simplified 2-D analysis of the laminate. Finally, the laminate model is subjected to compression in the axial direction, using displacement control, to predict the compressive strength and failure modes.

5.2 Type of Laminates Investigated

The two types of laminates investigated are shown in Fig. 5.1 and Fig. 5.2. Different layers are seen in the figures through contrasting colors in the images. The Type A laminate shown in Fig. 5.1 contains 16 layers, and the Type B laminate in Fig. 5.2 contains 48 layers. Both laminates are symmetric about the centerline.

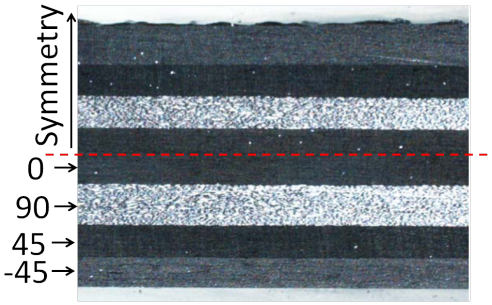

Figure 5.1: Type A laminate

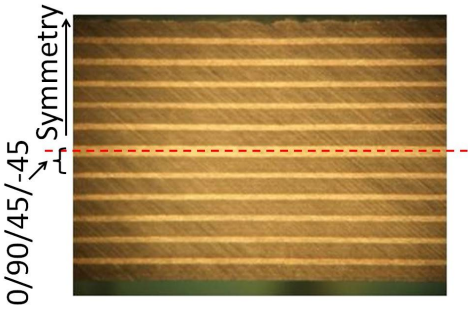

Figure 5.2: Type B laminate

5.3 Compression Tests

Compression tests were conducted on Type A and Type B laminates to understand the mechanisms of failure that are unique to the different type of laminates. The influence of two important types of failure mechanisms, namely delamination and kinking, and their interaction on the compression strength is the main focus. In the following sections, details about the experimental set-up, stacking sequences (also referred to as layups) of different specimens and results of the compression experiments are presented.

5.3.1 Test Fixture

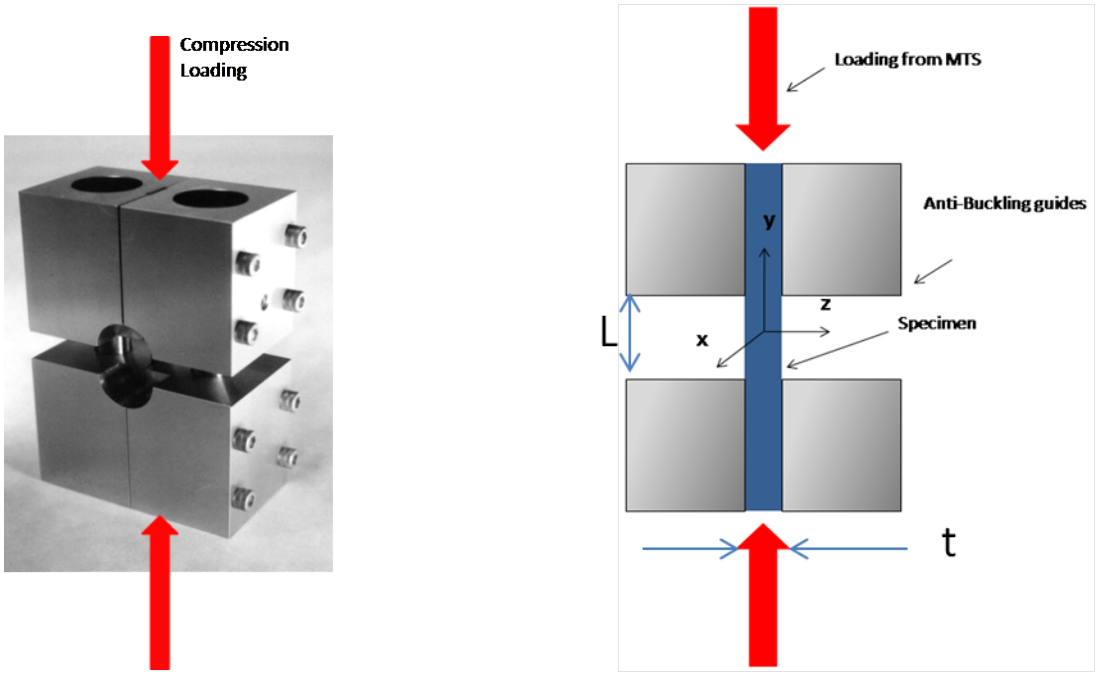

(a) (b)

Figure 5.3: Wyoming Combined Loading Compression (WCLC) test fixture

The Wyoming Combined Loading Compression (WCLC) test fixture, shown in Fig. 5.3(a), was used to carry out the compressive response studies in association with a MTS loading frame. Specimens in the form of strips of laminates with nominal dimensions of 12.7 mm x 133.35 mm x "t" mm, where, "t" is variable, are sandwiched between the large metal blocks of the fixture, and the ends of the fixture are compressed between the flat loading platens of a MTS testing frame as shown in Fig. 5.3(a) and Fig. 5.3(b). The blocks act as anti-buckling guides during loading, supporting a large portion of the specimen length, and providing a length of 0.25 inch as the gage length. This results in the measured compressive strength to be as close as possible to the actual compressive strength of the material, with minimal tendency towards flexural buckling.

5.3.2 Specimens

Specimens of three layups of type A laminates, with varying thickness, and Type B laminates were tested under compression. The Type A specimens were also used to study the effects of scaling, by grouping families of lamina, on the compressive strength of the laminates. As indicated in Table 5.1, the thicknesses of the layups are scaled up by stacking multiple layers of the same orientation. All the laminates shown in Table 5.1 have the same in-plane extensional stiffnesses. All the specimens are of nominal size 12.7 mm x 133.35 mm which results in a nominal gage length of 6.35 mm when placed in the WCLC fixture as shown in Fig. 5.3(b).

Table 5.1: Types of laminates

Type of Laminates	L(mm)	W(mm)	t(mm)
Type A (8 plies): $[-45/+45/90/0]$s	6.35	12.7	1.24
Type A (16 plies): $[-45_2/+45_2/90_2/0_2]$s	6.35	12.7	2.38
Type A (32 plies): $[-45_4/+45_4/90_4/0_4]$s	6.35	12.7	4.47
Type B (48 plies): $[(-45/+45/90/0)_6]$s	6.35	12.7	6.35

Typical images of the laminates mentioned above are shown in Fig. 5.4(a) and Fig. 5.4(b), where Fig. 5.4(a) displays the image of a failed Type A 16-ply laminate, and Fig. 5.4(b) displays a close-up image of the failed region of the corresponding specimen. It is observed that the failed specimen shows extensive delamination occurring at the interface of the laminae, and kinking in the 0 degree ply. As will be discussed later, the strain fields that persist upto and beyond failure indicate that there is a fairly uniform deformation corresponding to an initial linear relation between applied load and strain. At a critical value of the applied end displacement, a sudden transition in the stability of the specimen occurs and this leads to catastrophic failure with a significant reduction in the measured load. Fig. 5.5(b) shows a failed Type B specimen. We observe kink band formation in 0 layers, and small delaminated regions around the kink band are observed. There is no extensive delamination

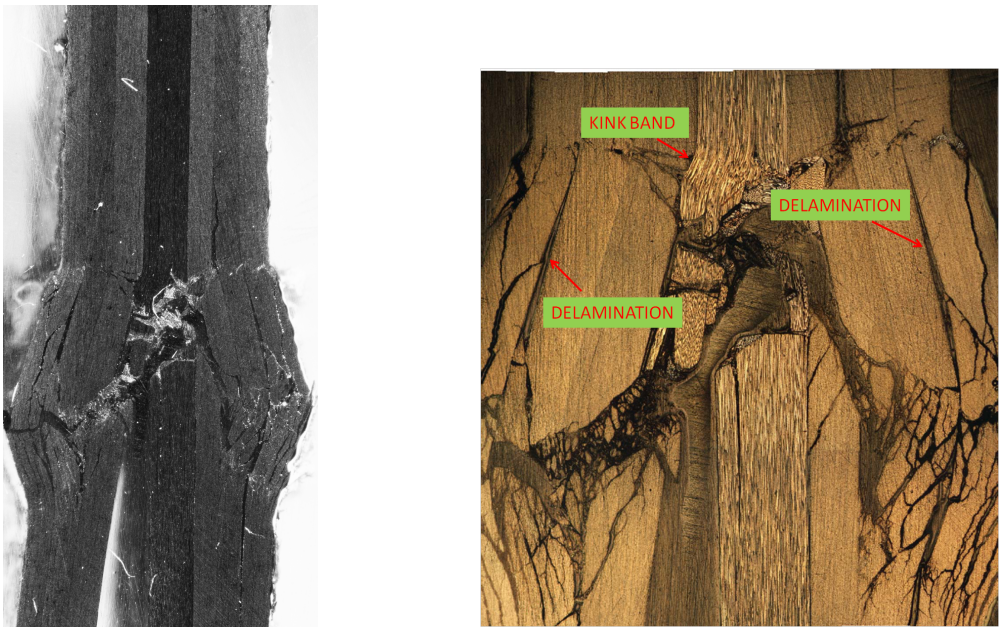

(a) (b)

Figure 5.4: Failed specimen : 16 − ply Type A laminate

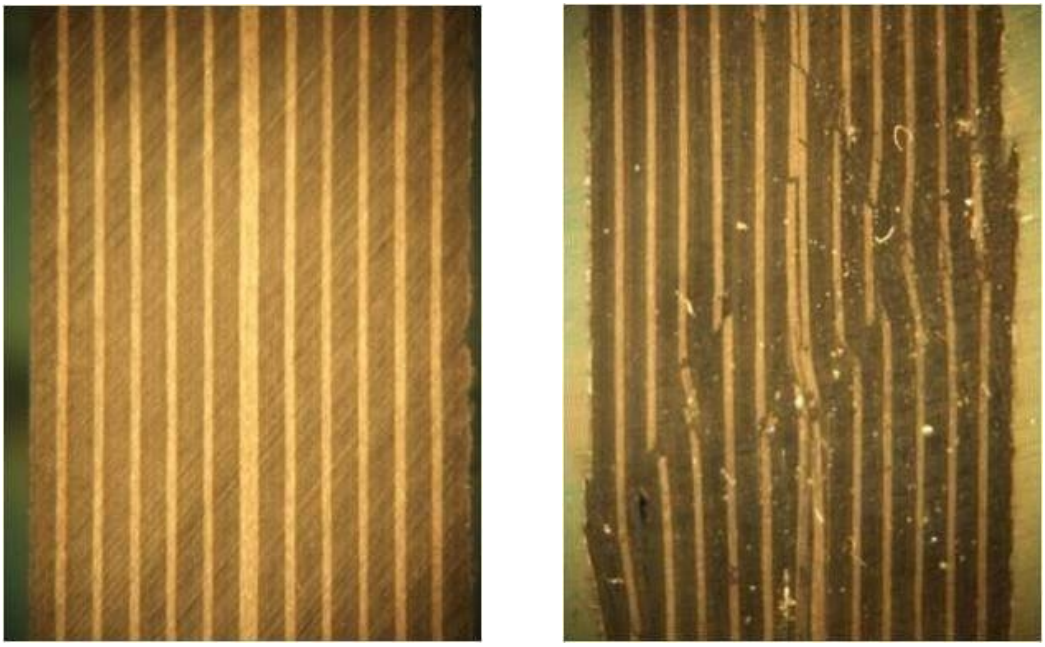

(a) (b)

Figure 5.5: (a)Pristine and (b)Failed specimen : 48 − ply Type B laminate

observed in Type B laminates as in the case of Type A laminates.

5.3.3 Compressive Strength Measurements

The compressive response studies are carried out at an external displacement control loading rate of 0.0004 in/sec in a MTS hydraulic test frame. The "macroscopic" stress is calculated as the total load obtained from a load cell that is placed in-line with the specimen, divided by the initial undeformed cross sectional area of the specimen. The "macroscopic" strain is determined using strain gages on either faces of the specimens. The global stress-strain responses of Type A laminates are shown in Fig. 5.6. The initial stiffness of the laminates is 48.5 $\pm$ 2 GPa, and the compressive strengths are in the range of 590 $\pm$ 30 MPa.

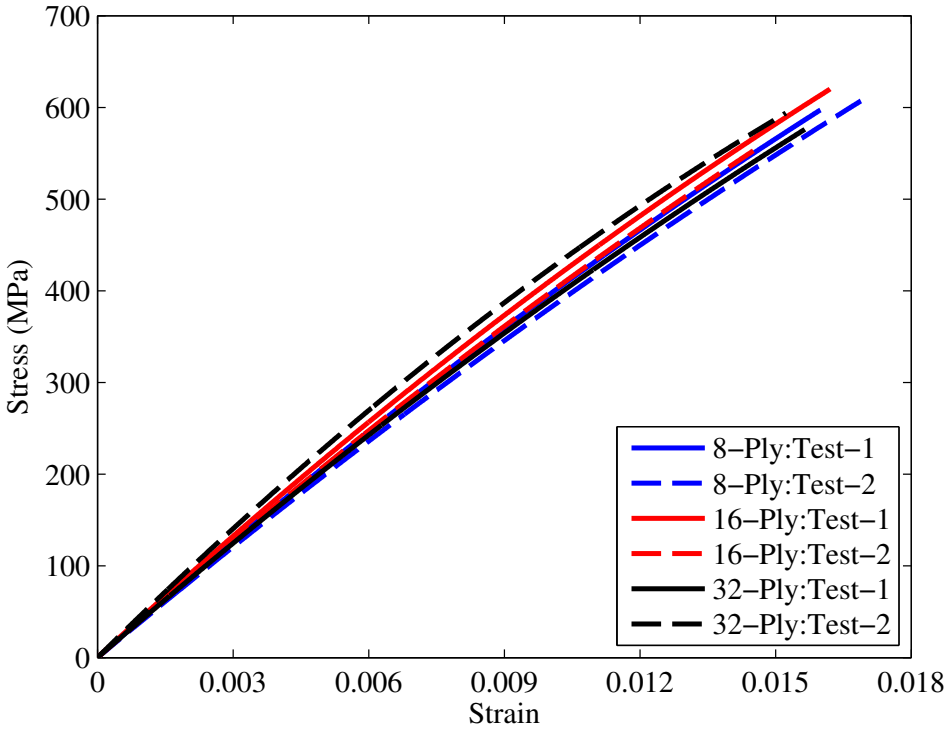

Figure 5.6: Global stress-strain response of the Type A laminates determined experimentally

The results imply that the scaling of lamina thickness in the laminate has no significant influence on either the initial stiffness or the strength of the Type A laminates. The Type B laminates displayed a similar trend with an initial stiffness of 49.3

± 0.5 GPa, and the compressive strengths are in the range of 615 ± 20 MPa.

5.3.4 Strain Analysis of Laminates Using Digital Image Correlation (DIC)

The digital image correlation (DIC) method was used to analyze the strain distribution on the side face of the laminates. ARAMIS, a commercially available software package, is used to perform the DIC analysis. ARAMIS is a non-contact and material independent displacement measuring system that gives displacements, strains and velocities as a function of time [*ARAMIS* (6.3.0)]. The side surface of the specimen (through the thickness), which is to be imaged, has a speckle pattern with random black dots over a white background, created using an air-brush. The side surface that is imaged is the surface with a normal in the z - direction, where the axes are as indicated in Fig. 5.3(b). A series of images are taken during the experiment, and these images are analyzed using ARAMIS to calculate the displacement and strain fields.

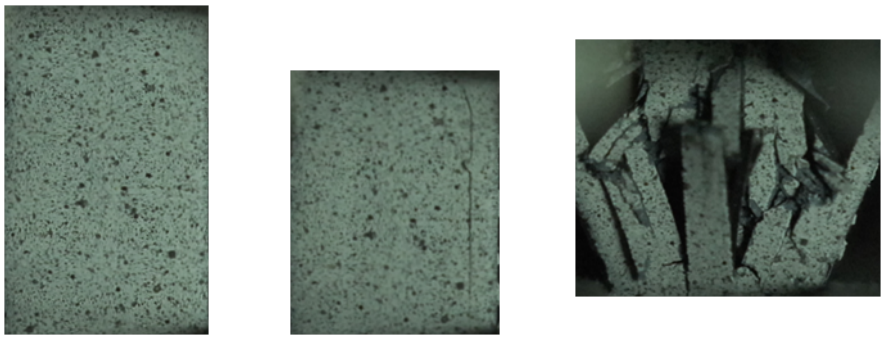

Figure 5.7: (a) Unloaded ; (b) Peak load ; (c) Failed

Fig. 5.7a, Fig. 5.7b and Fig. 5.7c show three of the series of images of a Type A 16-ply specimen as a function of macroscopic stress state. The first image, a reference image that is used for the DIC calculations, corresponds to the unloaded state, while the next two images correspond to an instance near the peak load and immediately thereafter. In the second image, a delamination crack is already visible and is identified as the first event that may trigger the catastrophic failure, which,

as seen in the third image, also induces kinking in the zero lamina in the post-peak regime. This type of process, which initiates the catastrophic failure, was visible in all the Type A laminates, regardless of the thickness scaling, and is also further supported by the DIC strain field analysis which will be discussed below.

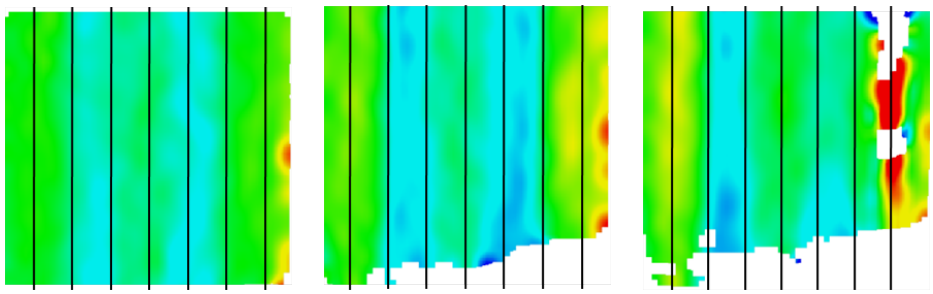

(a) (b) (c)

Figure 5.8: Transverse strain distribution on the side surface for Type-A 16-ply laminate (a) Linear stage (b) Prior peak load (c) At peak load

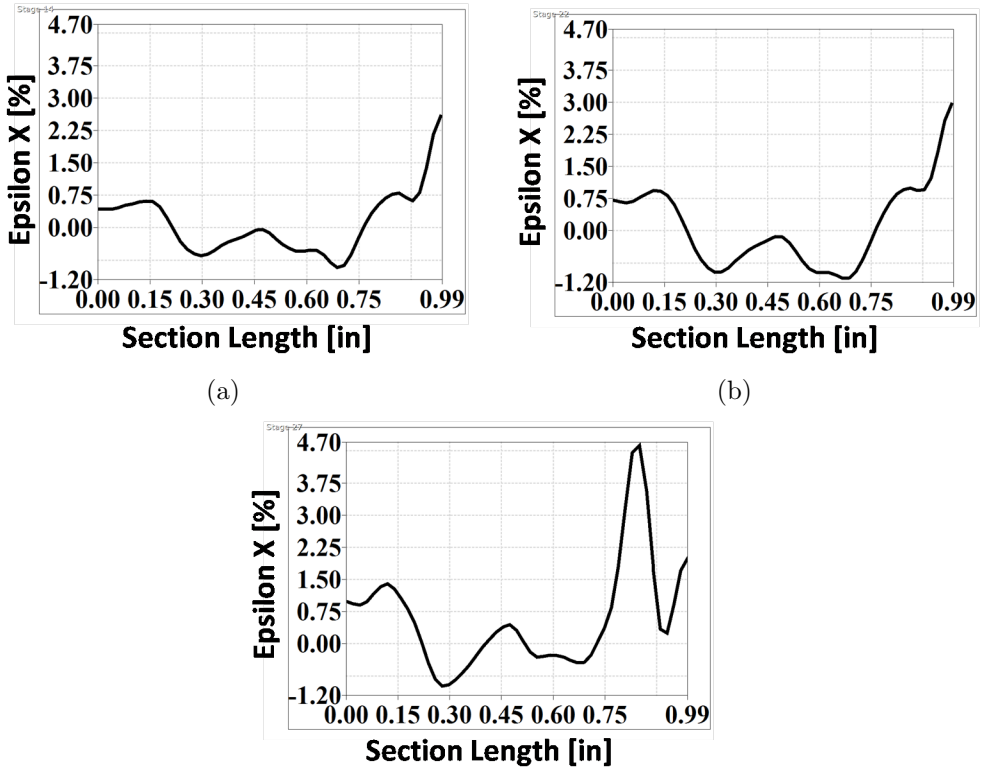

(a) (b)

(c)

Figure 5.9: Transverse strain distribution across the side surface for Type-A 16-ply laminate (a) Linear stage (b) Prior peak load (c) At peak load

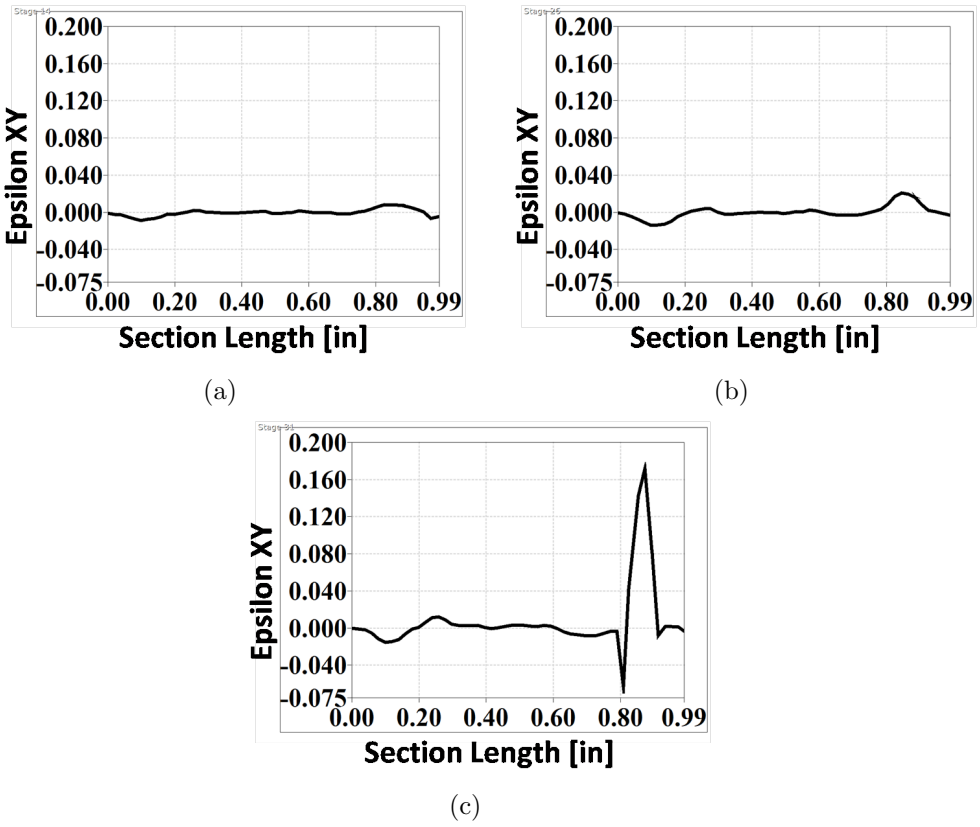

Figure 5.10: Shear strain distribution across the side surface for Type-A 16-ply laminate (a) Linear stage (b) Prior peak load (c) At peak load

The DIC images of the side surface of a typical 16-ply Type A specimen are shown in Fig. 5.8a, Fig. 5.8b and Fig. 5.8c. The specimen is loaded in the global y-direction. Fig. 5.8a, b and c display the strain distribution on the side face of the specimen along the global x-direction corresponding to the linear region, a point prior to peak load and at the peak load of the loaded specimen. It can be observed that the distribution is banded along the thickness. This is due to the different layers present in the specimens. We also observe that, as the loading is increased, the positive strain between the layers +45 and -45 increases rapidly, and subsequently, the specimen delaminates at that interface as clearly shown in Fig. 5.8c. To corroborate the above statement, the strain distributions ϵ_{xx} and ϵ_{xy} along a line on the side face are also plotted. It is clear from Fig. 5.9b and Fig. 5.10b that as the load is increased (progressing from (a) to (b) to (c)), the transverse strain (ϵ_{xx}) and the shear strain

(ϵ_{xy}) attain maximum values at the interface between +45 and -45 layers. Upon further loading, the transverse and shear strains tend to very large values as the specimen delaminates at the interface on the right (refer to Fig. 5.9c and Fig. 5.10c). In summary, the specimens appear to initiate failure by delamination followed by kink band occurring in the post-peak regime.

Similarly, the DIC analysis of the Type B 48-ply laminate is carried out. The DIC images of the side face of a Type B specimen are shown in Fig. 5.11a, Fig. 5.11b and Fig. 5.11c. Fig. 5.11a, b and c display the strain distribution on the side face along the global x-direction. Here, distinct strain bands representing each layer in the laminate do not exist, as opposed to Type A laminates. This maybe due to a lack of a sufficiently fine speckle pattern on the side face, and also perhaps the inability of ARAMIS to capture changes between each thin lamina with different fiber orientation in the 48 - ply laminate. This is in contrast to Type A laminates where relatively thick clustered layers with the same fiber orientation exist. The strain distributions ϵ_{xx} and ϵ_{xy} along a line on the side face are also plotted. We also observe that as the loading is increased, the average strain level along the side face increases, but ARAMIS measurement is unable to capture the behavior of different layers individually. Upon further loading, the transverse and shear strains attain very large values at the center of the specimen as seen in Fig. 5.12c and Fig. 5.13c. In summary, assertive conclusions cannot be made based on purely the DIC analysis of Type B specimens regarding the role of interfaces in the failure of these specimens. Since the stacking sequence leads to a rapidly alternating set of layers, each of relatively small thickness, the field of view used to take images for DIC and the image size does not lead to a sufficiently adequate resolution of the strain field present in these laminates.

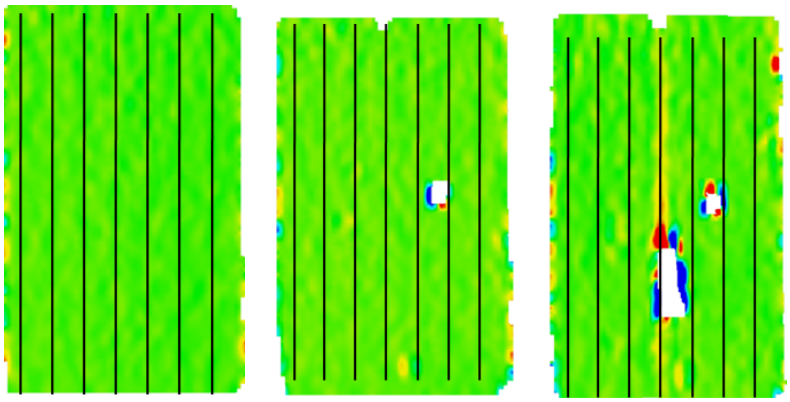

(a) (b) (c)

Figure 5.11: Transverse strain distribution on the side surface for Type-B 48-ply laminate (a) Linear stage (b) Prior peak load (c) At peak load

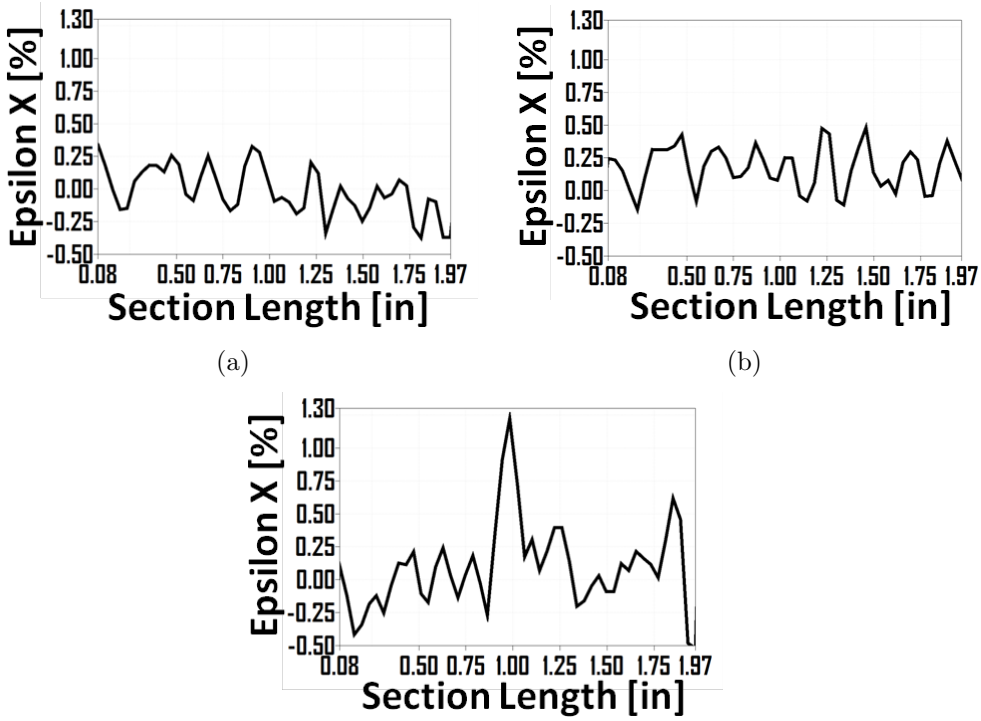

(a) (b)

(c)

Figure 5.12: Transverse strain distribution across the side surface for Type-B 48-ply laminate (a) Linear stage (b) Prior peak load (c) At peak load

5.4 Upscaled Laminate Model

The upscaled homogenized model for Type A laminate consisting of 8-layers of lamina (see Fig. 5.14) was constructed. The off-axis layers (i.e., -45^0,45^0,90^0 layers)

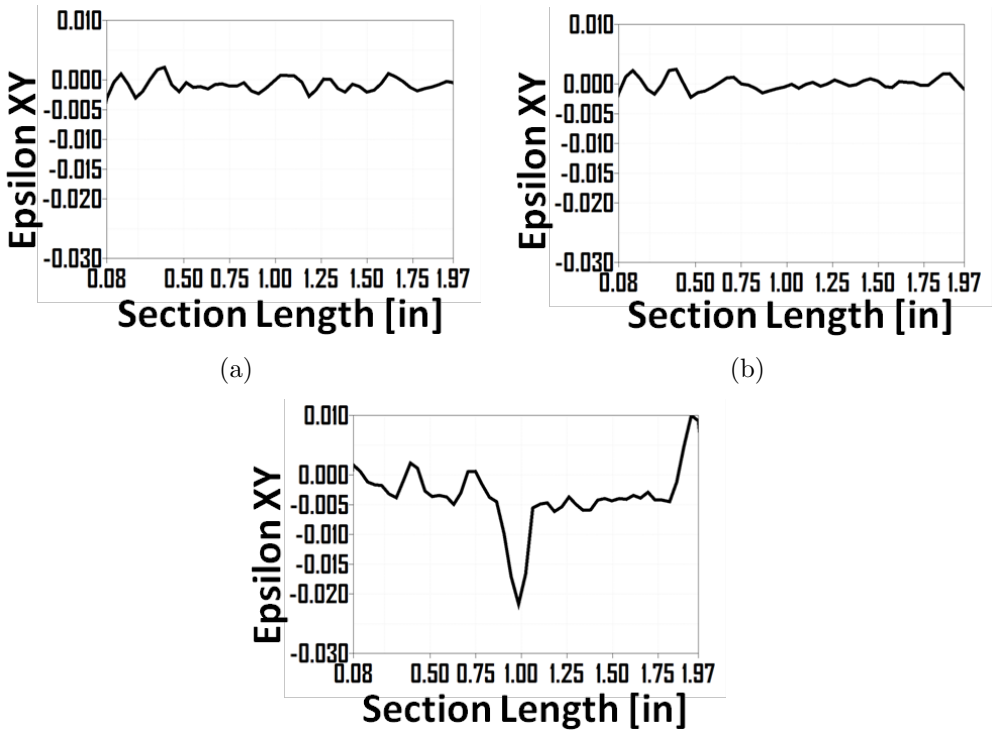

Figure 5.13: Shear strain distribution across the side surface for Type-B 48-ply laminate (a) Linear stage (b) Prior peak load (c) At peak load

were homogenized using the technique mentioned in Chapter II [see also, *Prabhakar and Waas* (2012b)]. Here, the red, cream and blue regions are the homogenized -45, +45 and 90 degree lamina. Micro-mechanics is maintained in the 0^0 layers, as they are the load bearing layers and are responsible for kink band formation in the multidirectional laminates considered. Therefore, the regions in green are the 0 degree fibers, and regions in grey are the matrix material in the 0 degree lamina.

The homogenized elastic lamina properties of the off-axis laminae correspond to a volume fraction of 0.49, are given in Table 5.3. The constants R_{ij} required to calculate the plastic potential of Hill's plasticity model are tabulated in Table 5.4 (note that R_{11} is chosen to be an arbitrarily high value since the 1-direction of the lamina is assumed to be elastic throughout, and hence does not possess a finite yield strength). These properties are applied to off-axis laminae in their rotated principal material

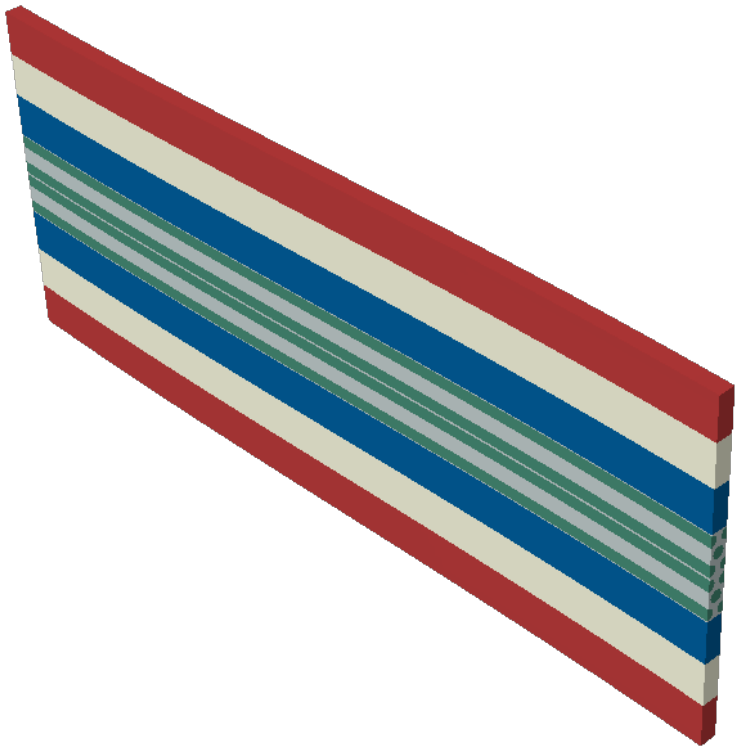

Figure 5.14: 8-layered upscaled model of Type A laminate with homogenized off-axis layers

coordinate axes, accounting for different lamina orientations.

Table 5.2: Fiber properties

E_{11}(GPa)	E_{22}(GPa)	E_{33}(GPa)	G_{12}(GPa)	G_{13}(GPa)	G_{23}(GPa)	ν_{12}	ν_{13}	ν_{23}
276	8.76	8.76	12.0	12.0	3.244	0.35	0.35	0.35

Table 5.3: Elastic homogenized lamina properties

E_{11}(GPa)	E_{22}(GPa)	E_{33}(GPa)	G_{12}(GPa)	G_{13}(GPa)	G_{23}(GPa)	ν_{12}	ν_{13}	ν_{23}
136.8	5.4	5.4	2.5	2.5	1.7	0.42	0.42	0.57

Table 5.4: Values of R_{ij} for calculating Hill's potential constants

R_{11}	R_{22}	R_{33}	R_{12}	R_{13}	R_{23}
18876.5	1.0	1.0	0.95	0.95	1.15

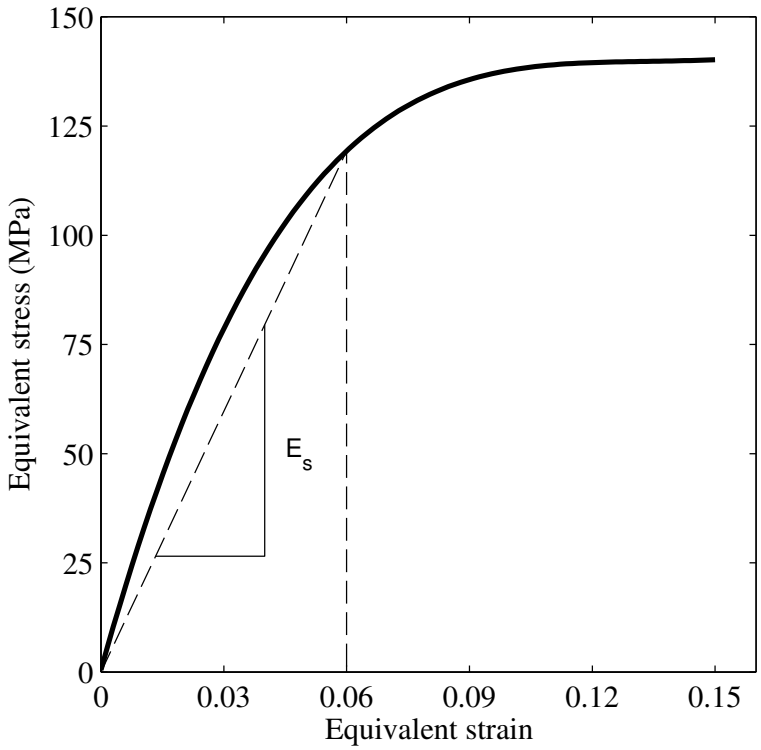

Figure 5.15: Equivalent stress-strain response for the in-situ matrix

A schematic of the model shown in Fig. 5.16 is further used to describe the boundary conditions and loading on the model. The edge AE of the model is prevented from motion in the z-direction, and the corner E is fixed against moving in the global x, y and z-directions. The face BFGC is subjected to compression along the negative x-direction in a displacement control manner. The faces ABCD and EFGH are held flat but are allowed to expand or contract in the y-direction. Also, the faces ABCD and EFGH deform exactly the same way in the x and z-directions. This enables the use of one representative unit cell in the y-direction, along with preserving a constant initial stiffness of the laminate, regardless of the width of the model.

The Riks method option available in ABAQUS [*ABAQUS* (6.10)], which is an arc-length solution scheme, is adopted to conduct the compressive response analysis. As shown in previous studies, [*Lee and Waas* (1999); *Beghini et al.* (2006)], this method captures unstable equilibrium paths (path in the load vs. loaded edge displacement

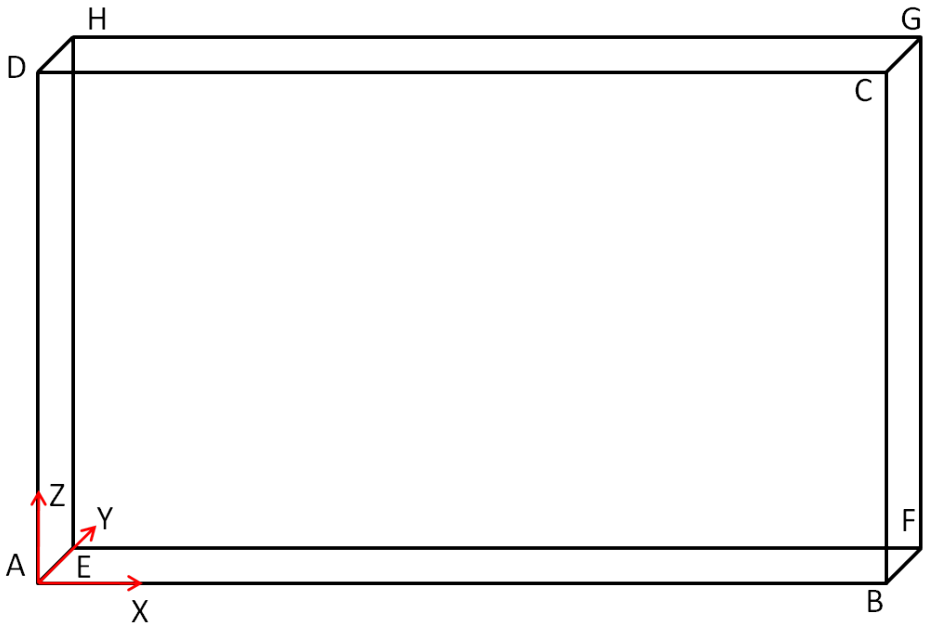

Figure 5.16: A schematic of the laminate model to describe boundary conditions and loading

graph that may show snap-back response) that can occur at limit points.

The model is meshed with 3-D hexahedral elements (C3D8 in ABAQUS v6.10). A slight imperfection is imparted to the model to account for fiber misalignment. Previous work by *Yurgartis* (1987) has shown that initial misalignment angles of 0.5 to 2 degrees of the zero laminae bound the distribution of fiber misalignment that is typical of carbon fiber reinforced pre-preg aerospace laminates. The first buckling mode of the laminate is determined, and is used to impart an imperfection to the model with an effective fiber misalignment angle, (θ), where $\theta = \frac{\delta}{L}$, is defined as shown in Fig. 5.17.

The initial, unloaded state in the compression analysis is assumed to be stress free. The model is seeded with fiber misalignment angle of 1^0, and subjected to displacement controlled compression. Here, macroscopic stress is defined as the total resultant of the x-direction reaction force on the face BFGC divided by the product of the width BF and thickness BC, while the macroscopic strain is defined as the

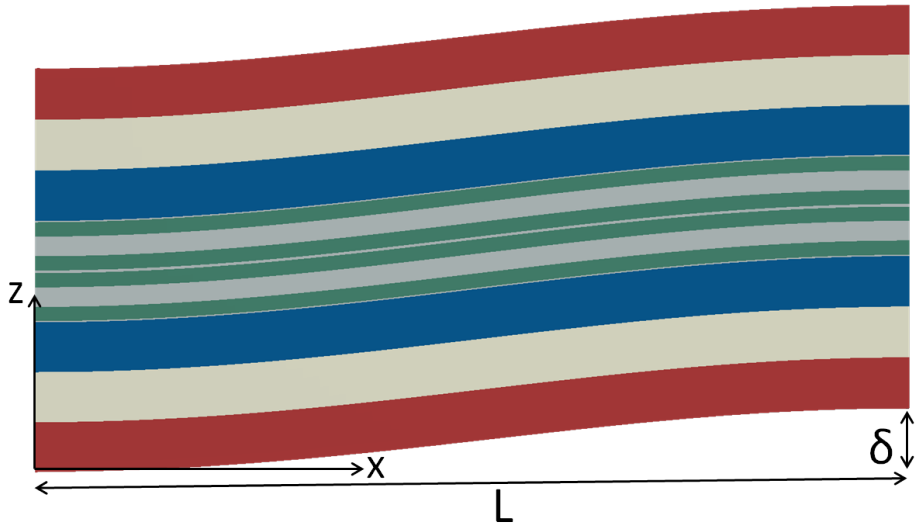

Figure 5.17: Laminate model to describe angle of imperfection

total contraction (change in length between the faces BFGC and AEHD) divided by the initial length AB (refer to Fig. 5.16).

5.5 DCZM Elements at Interfaces

Based on the interface analysis carried out in Chapter III, DCZM elements (explained in Chapter IV) are added at the interfaces of the laminate to model delamination. The DCZM elements adopt a 1D traction law capable of simulating crack formation and propagation, i.e. delamination. The element features the ability to predict delamination initiation based on a traction law that captures the cohesive strength and the fracture toughness in each fracture mode (mode I, mode II and mode-III in the current model). The DCZM elements used in this chapter have been successfully employed in other studies involving crack propagation as presented in *Gustafson and Waas* (2009). A triangular traction separation law is used here. The inputs to the law are cohesive strengths in mode-I and mode-II (σ_c and τ_c), and fracture toughness in mode-I and mode-II (G_{IC} and G_{IIC}). The critical G_{IC} and G_{IIC} values are determined from the standard double cantilever beam (DCB) and edge

notch flexure (ENF) tests respectively [refer to *ASTM(D5528)* (2007) and *Davidson and Sun* (2006)]. The mode-I cohesive strength is backed out from a DCB finite element virtual test, using experimentally determined mode-I fracture toughness as the input, and by varying the value of σ_c until the load-deflection response matches the one determined experimentally. The mode-II cohesive strength is determined through a single lap joint test[*ASTM(D3165)* (2007)]. The details of the above methods to determine the input fracture properties for the materials studied in this thesis are explained in detail in Section 4.3. The fracture properties for the laminate are given in Table 5.5.

Table 5.5: Fracture properties of interfaces in the laminate

G_{IC}	0.67 ± 0.07 N/mm
G_{IIC}	1.67 ± 0.08 N/mm
σ_c	15 ± 2.5 MPa
τ_c	28 ± 2 MPa

It should be noted here that the fracture properties determined are between 0 degree layers in a laminate. Each interlaminar interface between laminae of different orientation should have different fracture properties, especially in mode-II. But, here, the fracture properties between all the interfaces in the laminate are assumed to be the same.

5.6 Effects of Stacking on Compressive Strength and Failure Mode

In order to study the effect of stacking sequence on the compressive strength and failure mode in Type A and Type B laminates, the upscaled homogenized model described above is implemented with interface elements (DCZM) added along the weak interfaces determined a priori from the 2-D reduction analysis. Keeping the

fracture toughnesses fixed at 0.67 N/mm and 1.67 N/mm in mode-I and mode-II, the cohesive strengths are varied, and the corresponding global stress-strain responses are determined.

5.6.1 Type A Laminates

A plot of the global stress-strain responses of Type A 8-ply laminate model with a stacking sequence of $[-45/+45/90/0]s$ are shown in Fig. 5.18.

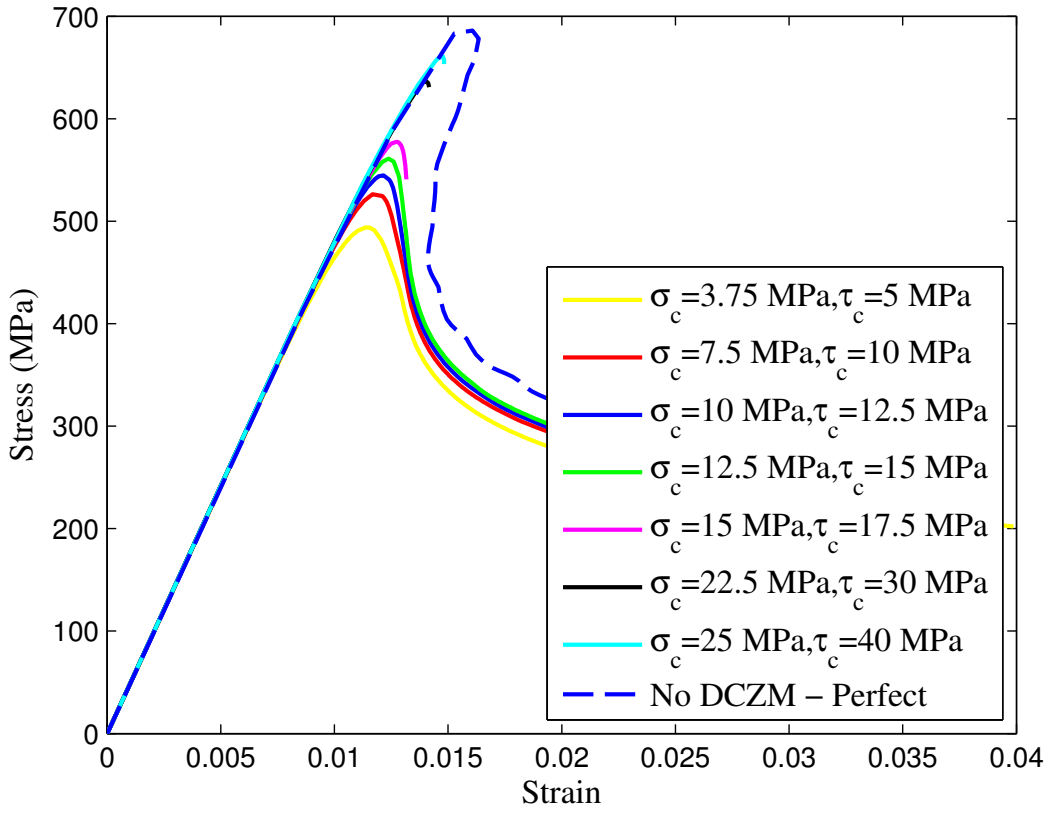

Figure 5.18: Global stress-strain response of upscaled model with DCZM added at -45/+45 interface

In Fig. 5.18, it is observed that the peak stress increases as the cohesive strengths are increased, and finally approaches the value of the model with "perfect" interfaces. Some of the responses shown in Fig. 5.18 have a complete post-peak response until a plateau is reached, whereas the RIKS solver fails to converge beyond the peak

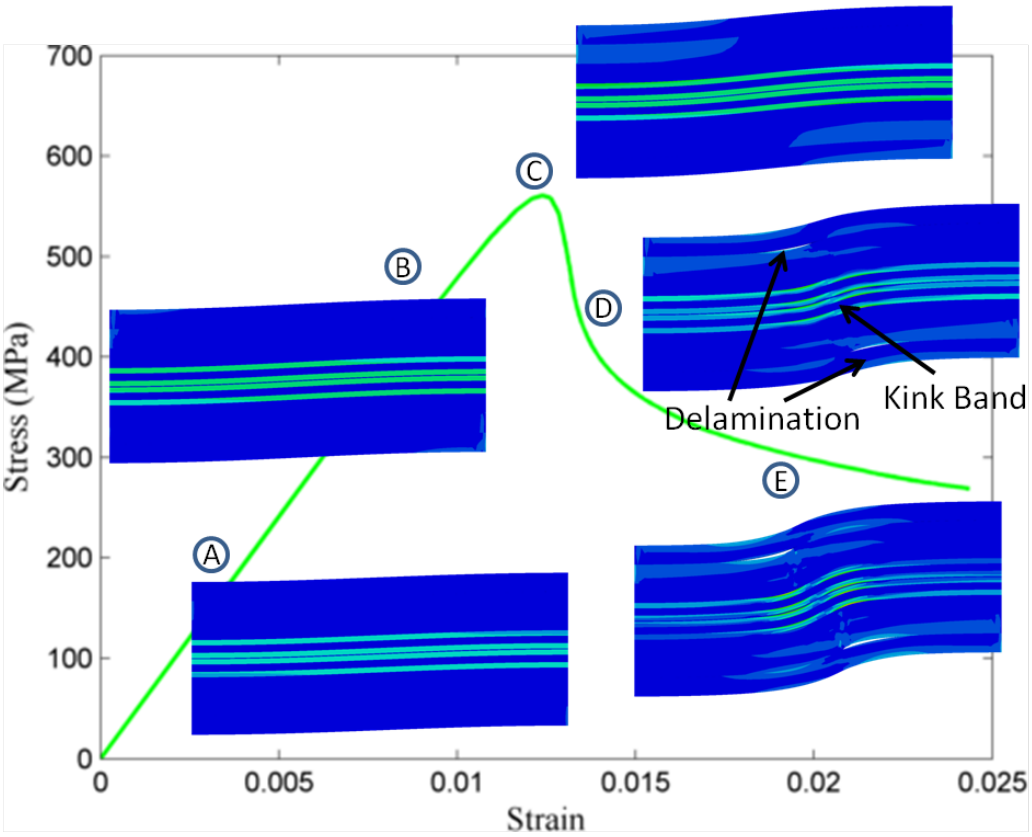

Figure 5.19: Global stress-strain response along with deformed shapes of upscaled model with DCZM added at -45/+45 interface. σ_c=12.5 MPa and τ_c=15 MPa

in other cases. But, all the responses still show the peak stress clearly in order to determine the compressive strength values. For a σ_c value equal to 15 MPa and τ_c of 17.5 MPa, the peak stress is 577 MPa. This is slightly lower than the compressive strength determined experimentally, as seen in Fig. 5.6. If the upper bounds of the fracture toughness values are used, i.e. $G_{IC} = 0.77N/mm$ and $G_{IIC} = 1.76N/mm$ (from Table5.5), and σ_c and τ_c values equal to 15 MPa and 17.5 MPa respectively, it is found that the peak stress is unaltered. Thus, within the bounds of the fracture toughness values obtained experimentally (shown in Table 5.5), and for fixed values of σ_c and τ_c, the predicted compressive strengths remain unaltered, corresponding to a fiber misalignment angle of 1 degree. Other parametric studies were carried out by changing one of the fracture properties and the other three properties held fixed. It

was observed that the peak stress is sensitive to the τ_c value. Keeping the values of G_{IC}, G_{IIC} and σ_c fixed at 0.77 N/mm, 1.76 N/mm and 15 MPa respectively, the value of τ_c was varied between 17.5 MPa and 30 MPa, and the peak stress was observed to increase from 577 MPa to 620 MPa. Therefore, it is seen that τ_c is an important factor in influencing the compressive strength of multidirectional laminates, and thus a good estimate of τ_c is needed for a good prediction of the compressive strength of these laminates.

For illustration purposes, the stress-strain response corresponding to $G_{IC} = 0.67N/mm$, $G_{IIC} = 1.67N/mm$, σ_c=12.5 MPa and τ_c=15 MPa, along with deformed shapes of the model are shown in Fig. 5.19. Here, at the peak stress, i.e. at loading step corresponding to C, sliding between the interfaces of -45 and +45 layers is observed, and in the softening region, i.e., loading step D, formation of a kink band is observed along with delamination at the -45/+45 interface. This implies that the failure strength is influenced by fracture properties of the laminate, and so is the failure mode. Here, a combination of kinking and delamination is observed in the post-peak regime, with the compressive strength affected by cohesive strengths of the delaminating interfaces.

Similarly, a Type A 16-ply laminate was also constructed with interface elements placed along those interfaces that are susceptible to delamination. A similar trend was observed in the behavior of 16-ply laminates, implying that there is an insignificant effect of scaling lamina thickness on the compressive strength of these laminates (not shown here).

5.6.2 Comparison of Type A and Type B Laminates

A comparative investigation of Type A and Type B laminates is carried out in this section. The objective is to investigate the influence of stacking sequence on the compressive strength and failure mode in laminates. Therefore, the compressive response of the two different models was studied. The smallest model that represents

the Type B 48 layer laminate is a 16 ply laminate with zero layers distributed through the thickness with a stacking sequence of $[(-45/+45/90/0)_2]s$. Type A 16-ply laminate is constructed by scaling the thickness of the individual layers in Type A 8-ply laminate from the previous section. 16-ply Type A and Type B laminate models are shown in Fig. 5.20 and Fig. 5.21.

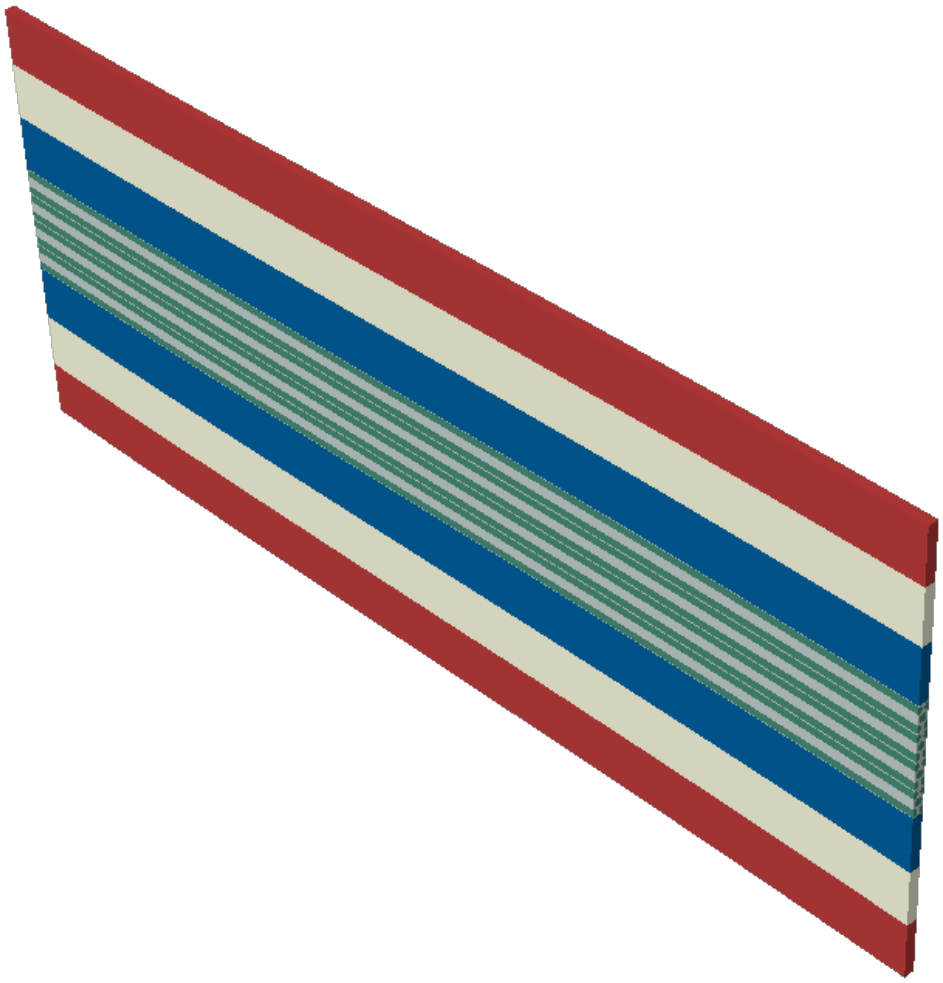

Figure 5.20: Type A 16-ply laminate model

Here, the same color coding as in the case of Type A 8-ply laminate models is followed. The imperfection imparted here is closer to experimentally observed behavior, i.e., only the center zero layers are seeded with an imperfection of $\theta = \delta/L$ as shown in Fig. 5.22. This is because, during the manufacturing process, the pressure

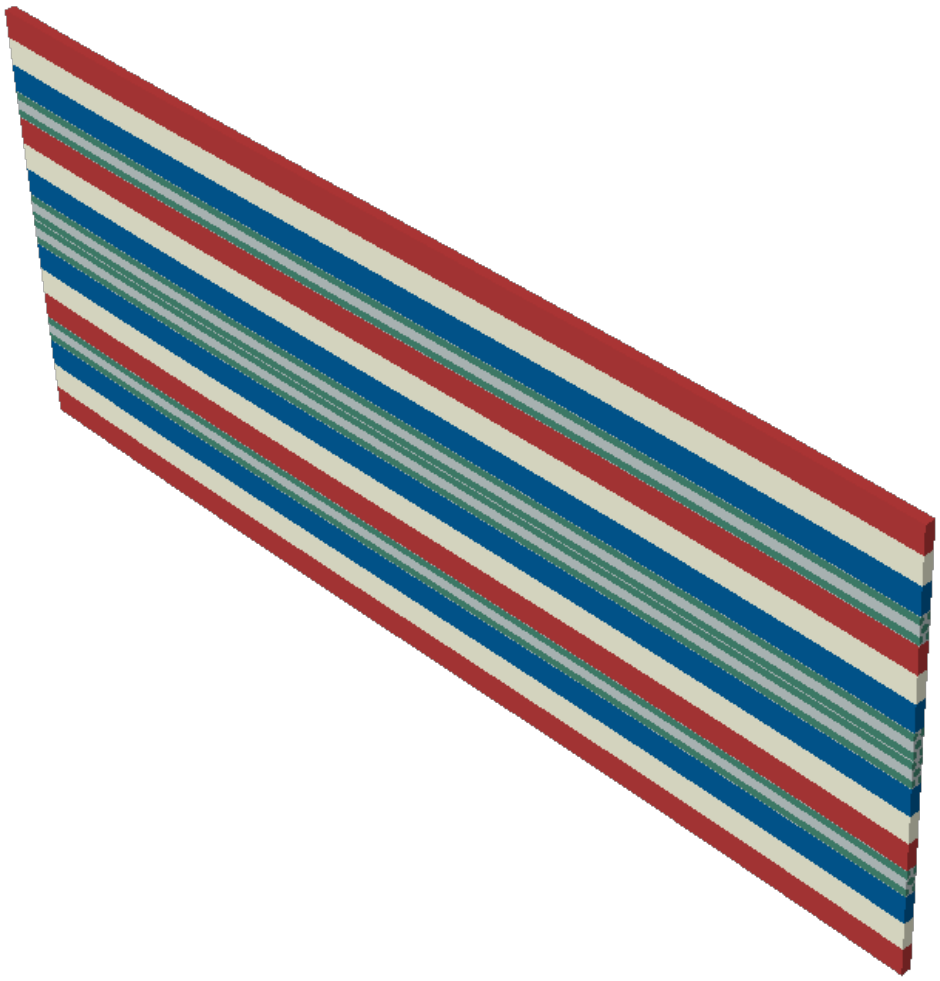

Figure 5.21: Type B 16-ply laminate model

and temperature applied on the top of the laminate causes noticeable undulations in the 0 fibers, as opposed to off-axis layers. This is different from the type of imperfection imparted in the previous cases, where, the imperfection was imparted to the entire laminate model. It was observed that the difference in compressive strength based on the two types of imperfections was 2-3 %, and therefore, a model with imperfection imparted only to the 0 layers is considered henceforth.

The compressive strengths are determined for the two laminates corresponding to mode-II cohesive strengths in the range of 20 - 40 MPa with an imperfection angle of 1 degree. The compressive strengths are plotted against mode-II cohesive strengths in

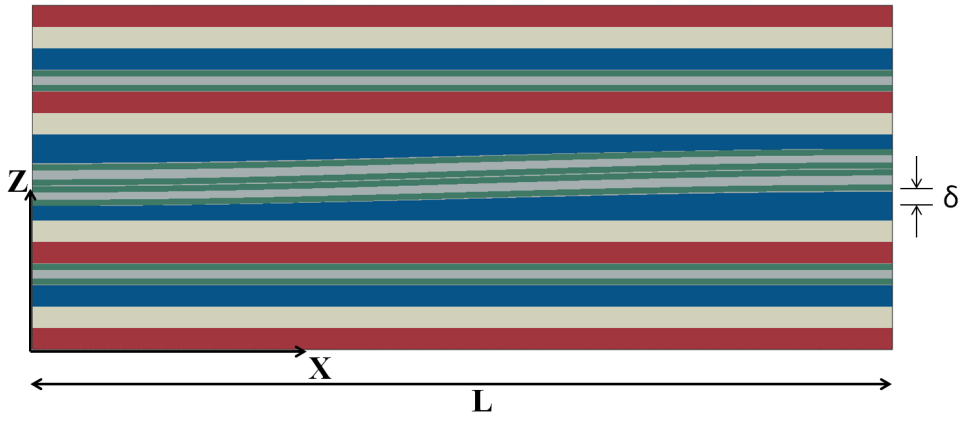

Figure 5.22: Schematic of imperfection imparted to Type B 16-ply laminate model

Fig. 5.23. Here, we observe that the compressive strengths of both the laminates increase with increasing mode-II cohesive strengths. Further, the compressive strength of Type B laminate increases faster as compared to that of Type A laminate with an increase in mode-II cohesive strength. This indicates that, due to distributed 0 degree layers in the Type B laminate, the kink band failure in these laminates is influenced more by the interface fracture properties as compared to the Type A laminate. Having said that, the distributed nature of the 0 layers in Type B laminates also makes the loading on the model more uniform as compared to Type A laminate, where the off-axis layers are subjected to higher stresses compared to the 0 layers. This leads to a nearly 10 % increase in the compressive strength in Type B laminates.

Next, the influence of the imperfection angle on the compressive strength is studied. For a fixed value of mode-II cohesive strength, the imperfection angle is varied from 1 degree to 1.5 degrees, which is within the range of imperfection angles measured in aerospace grade laminates. As expected, the compressive strength reduces with an increase in the imperfection angle. The sensitivity of compressive strength to changes in imperfection angle was similar in both Type A and Type B laminates as seen in Fig. 5.24.

The deformation shapes of the two laminate models with the same material and fracture input properties are shown in Fig. 5.25, Fig. 5.26 and Fig. 5.27 corresponding

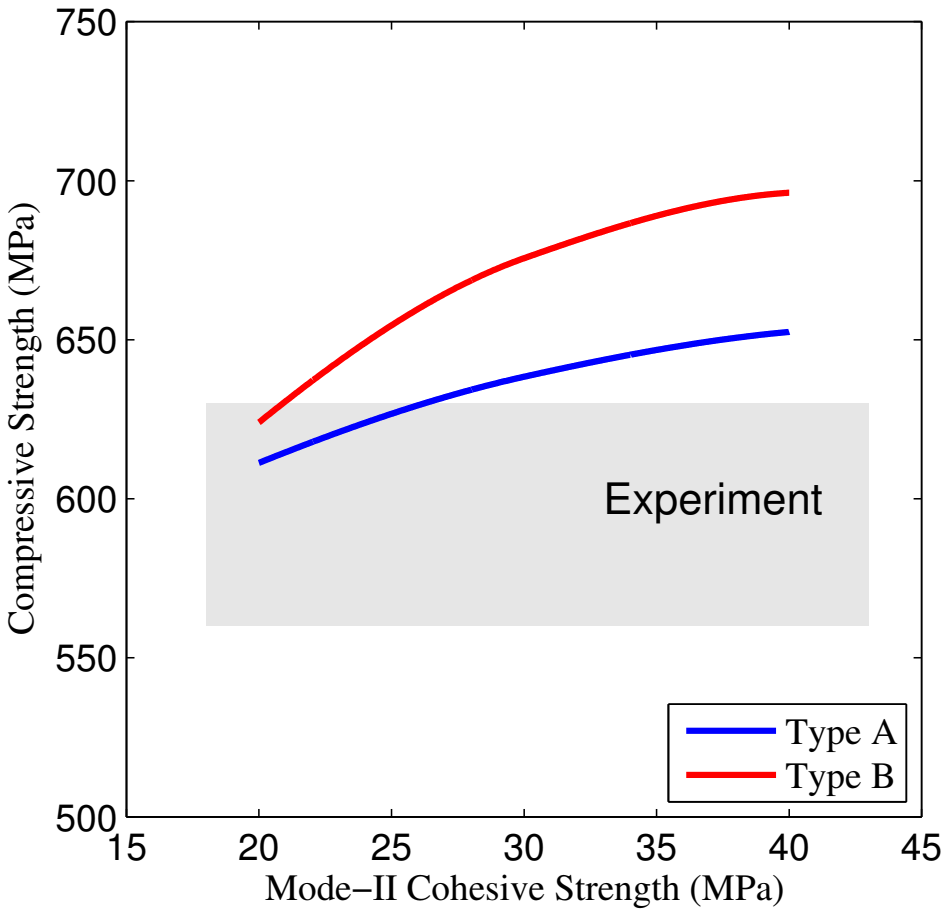

Figure 5.23: Variation of compressive strength of Type A and Type B laminates with varying mode-II cohesive strength of the interfaces

to the initial linear stage, at peak load and in the post-peak regime of the stress-strain response respectively.

It is noticed that, in both the laminates, delamination is accompanied by kink band formation. But, the kink band in the Type B laminate is restricted to a smaller zone compared to the Type A laminate. This implies that, even though the compressive strength is influenced by interface fracture properties in both the laminates, the growth or extent of delamination in Type B laminates is less compared to Type A laminates. This observation is consistent with experimental observations, where it is noted that Type A laminates fail in a catastrophic manner, whereas Type B laminates, after kink banding and delamination, remain intact post-experiment (as shown

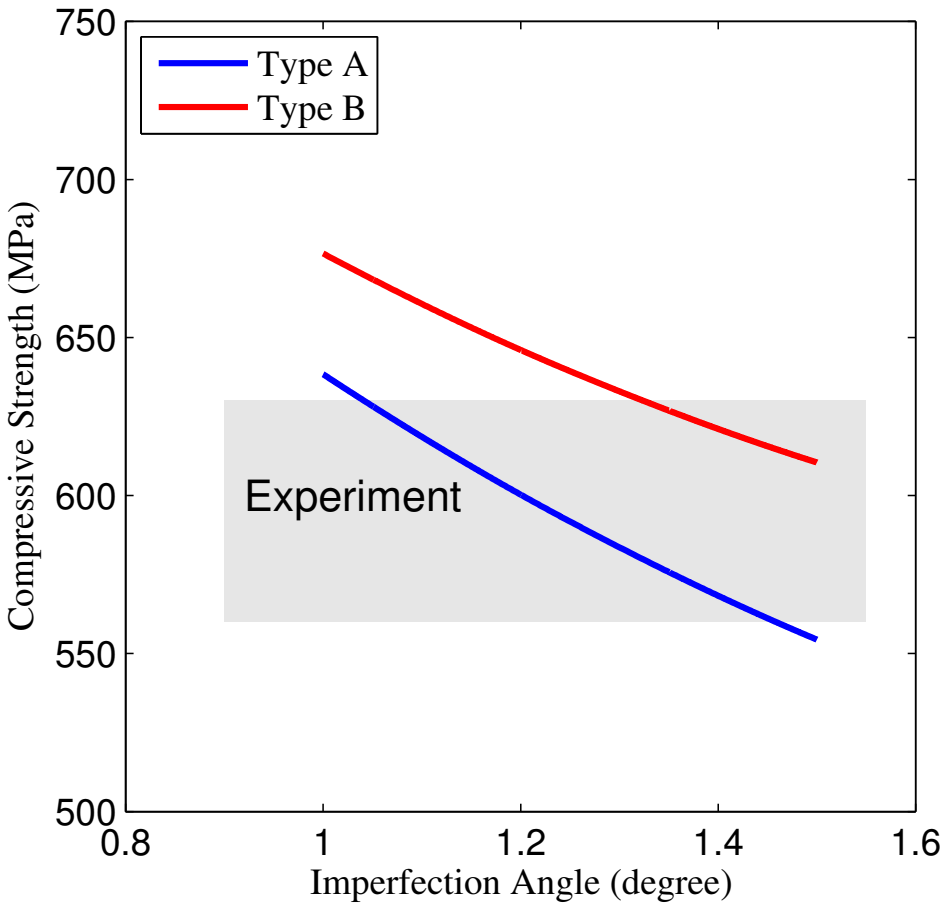

Figure 5.24: Imperfection sensitivity of Type A and Type B laminate models

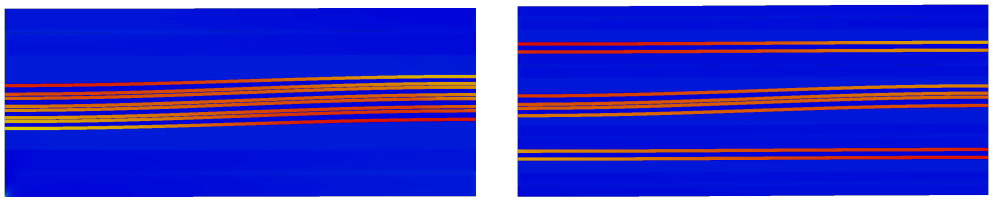

(a) (b)

Figure 5.25: Deformation shapes of (a) Type A and (b) Type B laminate in the initial linear regime of the global stress-strain response

in Fig. 5.4(b) and Fig. 5.5(b), respectively). This suggests that Type B laminates are favored over Type A laminates for structural applications. Indeed, standard laminate design practices limit the number of adjacent plies having the same angle.

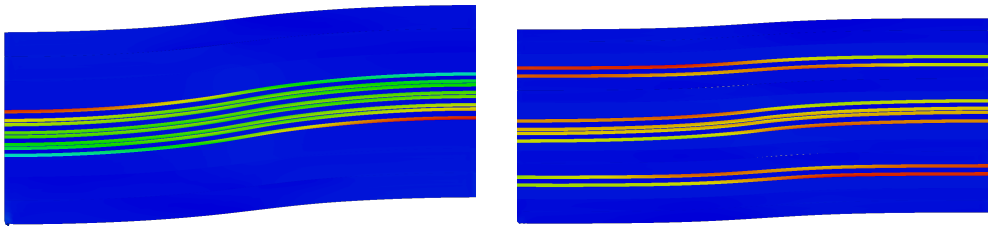

(a) (b)

Figure 5.26: Deformation shapes of (a) Type A and (b) Type B laminate at the peak load of the global stress-strain response

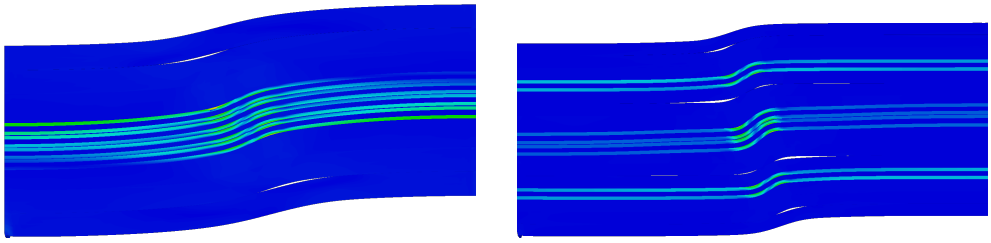

(a) (b)

Figure 5.27: Deformation shapes of (a) Type A and (b) Type B laminate in the post-peak regime of the global stress-strain response

5.7 Strength Allowable of Laminates

An Allowable is a mechanical property having a level of statistical assurance, whereas, a design value is a mechanical property value of the allowable from a specific case. Due to the statistical nature of material properties, a design value is not of much importance to the designers. Instead, certain bases are followed in the design process, namely, A-Basis and B-Basis allowable. These two tolerance bounds are critical in reducing risk in structural designs, and to ensure the structural integrity of the final product. The A-Basis allowable corresponds to a value, such that at least 99 % of the material values are equal or greater than the value with 95 % confidence. Whereas, the B-Basis allowable corresponds to a value such that at least 90 % of the material values are equal or greater than the value with 95 % confidence. It is very time consuming and expensive in terms of material resources to determine these allowables by testing. Therefore, virtual testing could replace the need for many tests

to determine compressive strength allowables. The model developed in this thesis has the potential to be used as a virtual testing model for determining compressive strength of laminates, by adding statistical nature to the materials involved. That is, the matrix and fiber material properties and the interface fracture properties are possible avenues to add statistics to the model. Therefore, the A-Basis and B-Basis allowables could be determined by including statistics to the model presented here.

5.8 Conclusions

Compressive response of two types of laminates were investigated in this chapter. Computational models to predict the compressive strength were constructed based on failure mechanisms observed in experiments. The model facilitates delamination to occur along the interfaces prone to delamination by adding the cohesive (DCZM) interface elements along the selected interfaces. These interfaces were determined a-priori from the knowledge of the laminate stacking sequence and the geometry of the layers. The interfaces determined as the delamination prone interfaces match well with the experimentally observed delaminating interfaces. The properties of the DCZM elements were based on the interlaminar fracture properties that were determined experimentally. The predicted compressive strengths, when compared against the set of experimental results, were found to agree well, both in terms of the maximum load and the failure modes. The mode of failure is determined by the number and the orientation of the lamina in a laminate, the material shear nonlinearity (dictated by the matrix properties) and the interlaminar fracture properties. The methodology outlined in this chapter can be used to quickly assess the compressive strength of *laminates*, within engineering limits, with a knowledge of the fundamental material properties as inputs. Also, this method can be used in the design cycle of the fiber reinforced laminated composites. That is, the compressive strength of the laminates with different combinations of layup orientations, layer thicknesses and

material properties can be investigated virtually. Further, only a handful of different types of laminates need to be manufactured and tested to decide on the final laminate to be used. This could result in the significant reduction of manufacturing and testing related costs.

CHAPTER VI

Continuum - Decohesive Finite Element for Modeling Splitting in Fiber-Reinforced Laminates

6.1 Introduction

A new finite element to model fiber-matrix in-plane fracture of fiber reinforced laminated composites is formulated. The formulation is motivated by the virtual multiscale cohesive method (VMCM) as described in *Rudraraju et al.* (2010), where the displacement field is additively decomposed into a coarse and fine scale. Subsequently, by using the principle of virtual work (PVW), the governing equations for the two scales are obtained. In VMCM, both the fine scale and coarse scale are captured through the incorporation of new shape functions that facilitate the capturing of sharp gradients across discontinities. In the CDFE formulation, the discontinuity is modeled as a physical separation (fracture) within an element, as opposed to a two-scale enrichment of the shape functions. The two sub-elements of a fractured element are connected through a traction-law that embeds the fracture properties of the discontinuity, and its evolution. The two sub-elements are modeled as standard continuum elements, however the discontinuity is captured through an assumed traction-law. Thus, the CDFE is seen as a natural merger between continuum elements and the discrete cohesive zone elements (DCZM), *Xie and Waas* (2006).

This chapter is organized as follows; Section 6.3 provides the mathematical formulation for the CDFE, along with a discussion regarding the input material properties required; continuum to non-continuum transition criteria are discussed in Section 6.4; the details of the finite element implementation are given in Section 6.5, followed by examples of open hole tension predictions of 90, 45 and 0 degree lamina.

It is well known that the regular finite element formulation can be used as long as the material constitutive law has a positive tangent modulus throughout the loading considered, *Bazant and Cedolin* (1991). But, when fracture emerges, the local tangent modulus ceases to be positive definite as shown in Fig. 6.1. Incorporating constitutive laws that display a negative tangent stiffness in a regular finite element setting leads to pathologically mesh dependent solutions. That is, the solution to the boundary value problem becomes ill-posed, with the solution being dependent on element size. Several remedies to this situation have been discussed, and successfully implemented as demonstrated in, for example, *Bazant and Cedolin* (1991).

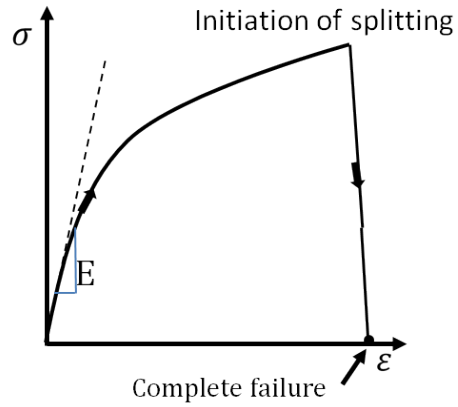

Figure 6.1: Complete stress-strain relation of a material up to failure

Fig. 6.2(a) shows a 1-D bar subjected to tensile loading. The material constitutive response of the bar contains a negative tangent modulus beyond an initial linear part. As the mesh size is decreased, the response of the bar (Fig. 6.2(b)) changes with change in mesh size with no sign of convergence, thereby demonstrating pathological mesh dependency [*Jirasek* (2000)]. In order to overcome such mesh dependency, and

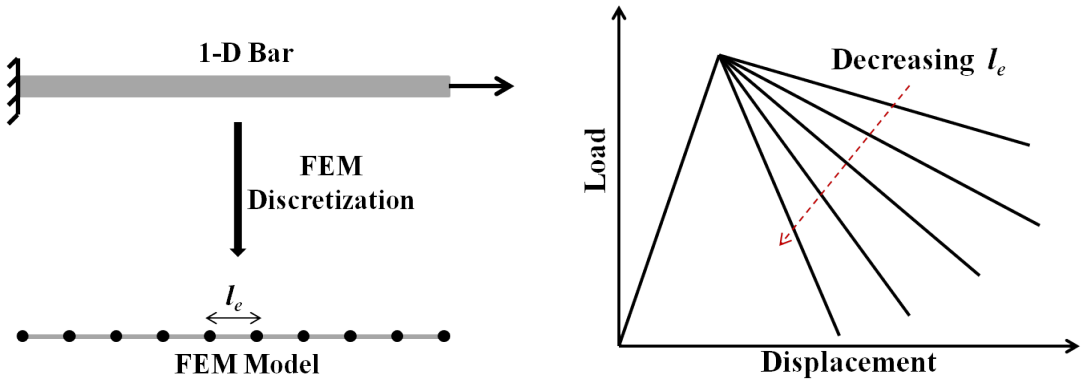

(a) (b)

Figure 6.2: (a) 1-D bar (b) Load-displacement responses of 1-D bar

to be able to model splitting failure, the CDFE is formulated here.

6.2 Summary of Related Prior Work

Several methods have been formulated to model two-piece failure (characterized through a material constitutive law consisting of a softening region). If the crack path in a model is known a-priori, discrete cohesive zone method (DCZM) elements can be placed between potential surfaces along the crack path (*Xie and Waas* (2006), *Gustafson and Waas* (2009)). These elements follow a traction-separation law between them, where the traction on the new surfaces is a function of the separation between the surfaces. The DCZM elements have a very high initial stiffness, which results in almost perfect adhesion between the surfaces. Then, as the element reaches the cohesive strength of the material, the element begins to unload following the traction-separation law. A smeared crack band approach was developed by *Bazant and Oh* (1983), which introduced a characteristic element length into the post-peak softening damage evolution formulation. The softening part of the stress-strain relation was scaled by a characteristic length of the material to ensure that the total energy released due to failure is equal to the fracture toughness of the material, regardless of the element size. Further developments of this approach to account for

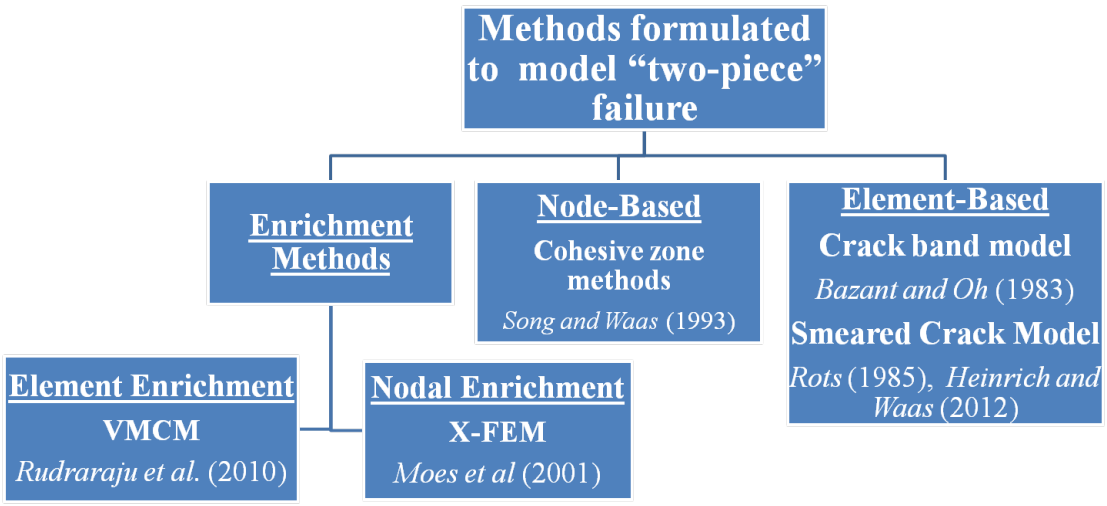

Figure 6.3: Prior methods formulated to model "two-piece" failure

mixed-mode failure was carried out by *de Borst and Nauta* (1985), *Rots and de Borst* (1987), *Camanho et al.* (2007) and *Heinrich and Waas* (2012).

Other methods available fall under the category of enrichment methods, where the shape functions are modified to account for discontinuities within the elements. Nodal enrichment methods, such as the extended FEM (XFEM) presented in *Sukumar and Belytschko* (2000), *Belytschko et al.* (2001), and element enrichment methods, such as the variational multiscale cohesive method (VMCM) presented in *Garikipati and Hughes* (1998), *Garikipati* (2002) and *Rudraraju et al.* (2010), model discontinuities in a continuum by embedding fine scale fields into a coarse scale field in the finite element formulation. The fine scale fields evolve following a cohesive law in the form of a traction - separation law, resulting in mesh objectivity. Since, the elements are embedded with a discontinuity (or multiple discontinuities) within them, the crack path(s) evolution need not be known a-priori. A comparison of enrichment methods is reported in *Oliver et al.* (2006).

The current CDFE method is motivated by the VMCM Method, where the crack path traverses through the element, in the form of discontinuity. The basic difference

between the VMCM and the CDFE is that the discontinuity is modeled physically in an element in CDFE, as opposed to shape function enhancement as in the case of VMCM. The regular shape functions in VMCM are enhanced with a discontinuous shape function to account for the discontinuity in the medium. The discontinuity in CDFE is inserted by fracturing the element into two parts, and the newly created interface tractions are governed by a cohesive traction-separation law. Therefore, the CDFE method results in a straight-forward formulation and implementation as compared to the VMCM. It also finds ready insertion into available FE codes, since standard shape functions are used throughput.

6.3 Mathematical formulation - PVW

In the CDFE formulation, a fractured body (non-continuum) is treated differently from a continuum that has no crack. That is, the PVW for a continuum body, occupying the domain Ω, and limited to the infinitesimal theory of elasticity (refer to Fig. 6.4(a)), is given by,

$$\int_{\Omega} \nabla w : \sigma dV = \int_{\Omega} w f dV + \int_{\Gamma_h} w T dS \tag{6.1}$$

where Γ_h is the traction boundary, w is the virtual displacement field, f is the body force field, T is the prescribed external traction, σ is the Cauchy stress tensor ($\sigma = D : sym(\nabla u)$), where D is the elasticity tensor, and u is the displacement field of the domain.

Next, consider the same body, but containing, within its domain, a surface across which the displacement field is discontinuous. Applying the PVW for a cracked body (refer to Fig. 6.4(b)) results in,

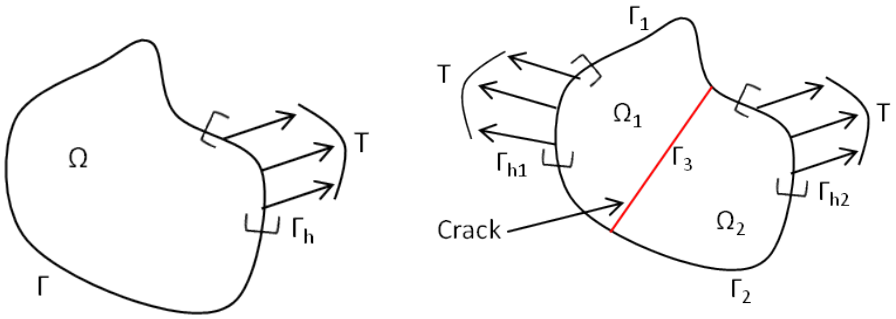

Figure 6.4: (a) Continuum domain (b) Fractured domain

$$\int_{\Omega_1} \nabla w : \sigma \, dV + \int_{\Omega_2} \nabla w : \sigma \, dV - \int_{\Gamma_3} w \, T([[u]]) dS = \int_{\Omega_1} w \, f \, dV + \int_{\Gamma_{h_1}} w \, T \, dS + \int_{\Omega_2} w \, f \, dV + \int_{\Gamma_{h_2}} w \, T \, dS \tag{6.2}$$

where, the interface Γ_3 separates the domain Ω into two domains, Ω_1 and Ω_2. The traction across the two new surfaces of the two separated domains is related to the jump displacements (the displacement discontinuity) through a traction-separation law. That is, the traction is a function of the jump displacements given by $T([[u]])$, where $[[u]]$ denotes the displacement jump. The tractions do work over the jump displacements as the body separates into two pieces. Fig. 6.5(a) and Fig. 6.5(b) show traction laws, where the jump displacement can reverse sign. A 2-D cohesive traction separation law is used that defines the fracture process in departure from a continuum. Two traction-separation laws are used; one each for mode-I (opening) and mode-II (sliding). The mode-I cohesive law, which signifies displacement jumps perpendicular to the fracture surface, in the local coordinate system is,

$$
\begin{aligned}
T_1 &= \sigma_{IC}\left[1-\frac{\delta_I}{\delta_{Im}}\right] \quad \text{if} \quad \delta_I > 0, \Delta\delta_I >= 0 \\
T_1 &= \bar{k}_I \delta_I \quad \text{if} \quad \delta_I > 0, \Delta\delta_I < 0 \quad \text{where,} \quad \bar{k}_I = \frac{\sigma_I^\star}{\delta_I^\star}
\end{aligned}
\tag{6.3}
$$

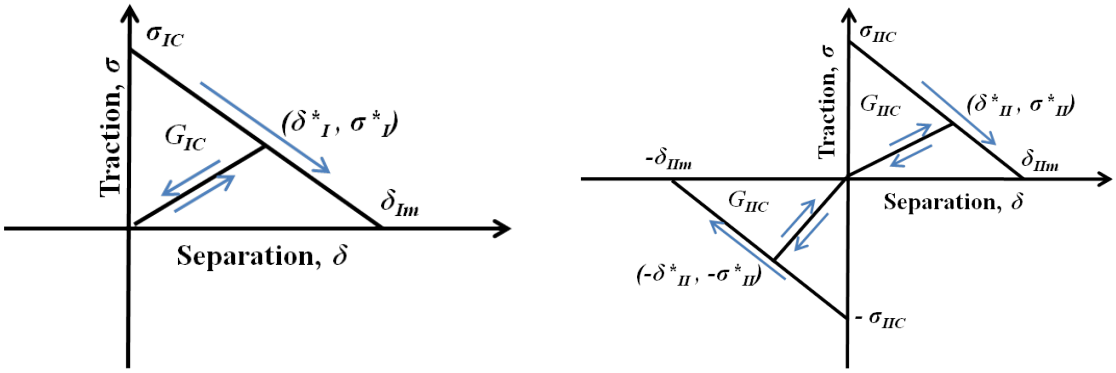

Figure 6.5: (a) Mode-I cohesive law (b) Mode-II cohesive law

Similarly, the mode-II cohesive law, which signifies tangential displacement jumps, in the local coordinate system is given by,

$$
\begin{aligned}
T_2 &= \sigma_{IIC}\left[1-\frac{\delta_{II}}{\delta_{IIm}}\right] \quad \text{if} \quad \delta_{II} > 0, \Delta\delta_{II} >= 0 \\
T_2 &= \bar{k}_{II} \delta_{II} \quad \text{if} \quad \delta_{II} > 0, \Delta\delta_{II} < 0 \quad \text{where,} \quad \bar{k}_{II} = \frac{\sigma_{II}^\star}{\delta_{II}^\star} \\
T_2 &= -\sigma_{IIC}\left[1-\frac{|\delta_{II}|}{\delta_{IIm}}\right] \quad \text{if} \quad \delta_{II} <= 0, \Delta\delta_{II} < 0 \\
T_2 &= \bar{k}_{II} \delta_{II} \quad \text{if} \quad \delta_{II} <= 0, \Delta\delta_{II} > 0 \quad \text{where,} \quad \bar{k}_{II} = \frac{-\sigma_{II}^\star}{-\delta_{II}^\star}
\end{aligned}
\tag{6.4}
$$

where, δ_I and δ_{II} are the jump displacements in mode-I and mode-II between the decohered surfaces of the fractured continuum, and $\Delta\delta_I$ and $\Delta\delta_{II}$ are the corresponding change in the jump displacements between load increments in FEM. Though a triangular traction - separation law is used here, it should be noted that no restrictions on the nature of the traction law are imposed in CDFE.

It is noted that, just as in the VMCM and unlike in other cohesive zone implementations, the emergence of the traction - separation law is at a finite value of the traction. In classical cohesive zone implementations, the traction - separation law emerges from the origin, since such elements are used from the inception of loading, whereas, the emergence of fracture at a finite traction, which is physically correct, is captured in the VMCM and CDFE. Other cohesive zone models thus require a "penalty stiffness", which defines the initial portion of the traction - separation law. This aspect has also been pointed out in earlier work by *Jin and Sun* (2005). Thus, in the CDFE, the *process* of fracture is captured through the traction-jump displacement law. In classical fracture mechanics, the *process* of fracture is not captured in a continuous manner, instead two fractured states, which correspond to two different crack lengths, are treated as isolated states of equilibrium.

Using Equation 6.1 for the intact continuum, and Equation 6.2 for a fractured continuum, the corresponding finite element equations are derived in the following sections.

The material properties required for the CDFE method are discussed below. Since, fiber reinforced lamina is the focus, a transversely isotropic material system is considered. The corresponding transversely isotropic linear elastic material inputs are E_1, E_2, ν_{12} and G_{12} in a plane stress setting. The fiber orientation angle in a lamina is θ, which imparts directionality to the lamina. The cohesive input properties are the in-plane fracture toughnesses and the cohesive strengths (G_{IC}, G_{IIC}, σ_{IC}, σ_{IIC}).

6.4 Transition from a Continuum to a Non-Continuum

The transition criterion required to signal the emergence of a displacement jump is discussed next. A stress based criterion is adopted here. The evolution of the failure/fracture of the continuum is based on a mixed mode energy release criterion. In fiber reinforced lamina, the failure orientation is influenced significantly by the

presence of fibers. That is, since the fibers have strengths that are two orders of magnitude larger compared to the matrix material, the failure direction is dominated by the direction of the fiber. In the present study, both fracture perpendicular and parallel to the fibers, are considered.

For fracture perpendicular to the fiber direction (θ), as shown in Fig. 6.4, the fracture initiation condition is,

$$\left(\frac{\sigma_{11}}{\sigma_C^f}\right) \geq 1 \tag{6.5}$$

where, σ_{11} is the tensile stress along the fiber direction, and σ_C^f is the cohesive strength of the fiber.

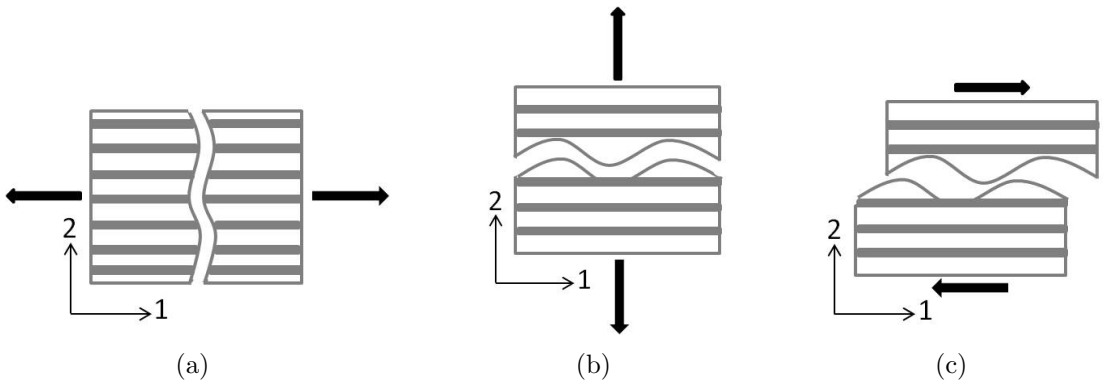

Figure 6.6: (a) Mode-I fracture perpendicular to the fiber direction (b) Mode-I fracture parallel to the fiber direction (c) Mode-II fracture parallel to the fiber direction

For fracture parallel to the fiber direction (θ), as shown in Fig. 6.6, the following transition condition is used,

$$\left(\frac{\sigma_{22}}{\sigma_C^m}\right)^2 + \left(\frac{\sigma_{12}}{\tau_C^m}\right)^2 \geq 1 \tag{6.6}$$

where, σ_{22} and σ_{12} are the transverse and shear stresses in the rotated coordinate system, and 1 is along the fiber direction. σ_C^m and τ_C^m are the cohesive strengths in mode-I and mode-II in the matrix. Since the cohesive strength of the fibers is usually very high compared to that of the matrix material, the matrix failure occurs prior to

fiber failure in a lamina, usually in the presence of multi-axial loading.

In the non-continuum state, fracture evolution is assumed to be governed by a mixed mode energy release criterion given by:

$$\frac{G_I}{G_{IC}} + \frac{G_{II}}{G_{IIC}} \geq 1 \tag{6.7}$$

where, δ_I is separation perpendicular to the fracture path (Mode-I or opening mode), δ_{II} is the separation along the fracture path (Mode-II or sliding mode), G_I is the fracture energy dissipated corresponding to δ_I from Mode-I cohesive law, G_{II} is the fracture energy dissipated corresponding to δ_{II} from Mode-II cohesive law, G_{IC} is the fracture toughness of Mode-I cohesive law and G_{IIC} is the fracture toughness of Mode-II cohesive law.

6.5 Finite Element Formulation

The equations resulting from the application of the PVW to a continuum and a fracturing continuum are descritized to obtain the corresponding finite element equations. In the continuum (Ω), the domain is divided into a finite number of elements. The presentation of the formulation is restricted to two dimensional triangular elements, for illustrative purpose, whose nodal displacements are given by, $U^e = [u_1\ u_2\ u_3\ u_4\ u_5\ u_6]^T$ (refer to Fig. 6.7(a)). It is noted that the method introduced here is independent of the choice of element type.

The displacement field $\{u^e\}$ and the virtual displacement field $\{w^e\}$ of each element, in terms of nodal displacements are given by,

$$\begin{aligned} \{u^e\} &= [N]_{(1,6)}\ \{U^e\}_{(6,1)} \\ \{w^e\} &= [N]_{(1,6)}\ \{W^e\}_{(6,1)} \end{aligned} \tag{6.8}$$

Substituting Equation 6.8 into Equation 6.1, the residual ($\{r\}$) of the finite ele-

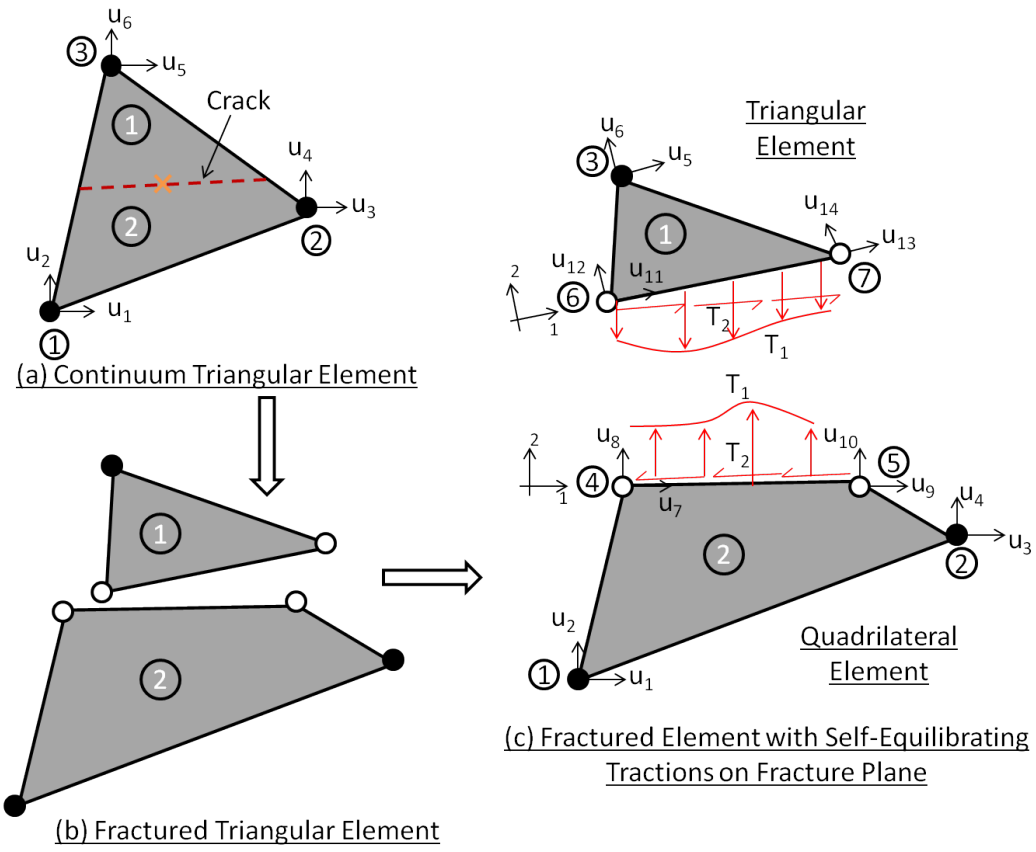

Figure 6.7: Triangular element: (a) Continuum element, (b) Element with discontinuity (c) Fractured element with discontinuity and interface tractions

ment equations for an uncracked body (Ω) is derived as,

$$\{r\} = \int_{\Omega} B^T \; D : Bu \; dV - \int_{\Omega} N f \; dV - \int_{\Gamma_h} N \; T \; dS \tag{6.9}$$

where B is the strain-displacement relation. After linearizing, the above equations are solved to determine the nodal displacements. The corresponding stresses in each element are determined, and checked for transition.

When a transition criterion is met in an element, the element fractures in accordance with the specified traction laws, as shown in Fig. 6.7(b). The black nodes in Fig. 6.7(b) are the original nodes of the element, and the white nodes are two new nodes that emerge due to element fracture. The crack path is parallel or perpendicular

to the fiber direction and cuts across the integration point of the continuum element. To develop the reduced stiffness matrix, consider the additional (dummy) nodes along the fracture path. The interface tractions follow a cohesive traction-separation law as shown in Fig. 6.5(a) or Fig. 6.5(b). Equation 6.4(b) can be rearranged as follows:

$$\int_{\Omega_1} \nabla w : \sigma \, dV + \int_{\Omega_2} \nabla w : \sigma \, dV + \int_{\Gamma_3} w \, T_1(\delta_I) dS + \int_{\Gamma_3} w \, T_2(\delta_{II}) dS = \int_{\Omega_1} w \, f \, dV + \int_{\Gamma_{h_1}} w \, T \, dS + \int_{\Omega_2} w \, f \, dV + \int_{\Gamma_{h_2}} w \, T \, dS \tag{6.10}$$

where, δ_I and δ_{II} are the mode-I and mode-II jump displacements of the interface in a cracked element. Also, $\{\sigma\} = [D]\{\epsilon\}$, where $[D]$ is the constitutive material matrix of the individual sub-elements, $\{\epsilon\}$ is strain vector ($\{\epsilon\}$=f($\frac{\delta u_i}{\delta x_i}$), i=1,2) in each of the the two domains Ω_1 and Ω_2.

The enhanced residual can then be expressed as,

$$\{R\} = \int_{\Omega_1} \nabla w : \sigma \, dV + \int_{\Omega_2} \nabla w : \sigma \, dV - \int_{\Gamma_3} w \, T_1(\delta_I) dS - \int_{\Gamma_3} w \, T_2(\delta_{II}) dS - \int_{\Omega_1} w \, f \, dV - \int_{\Gamma_{h_1}} w \, T \, dS - \int_{\Omega_2} w \, f \, dV - \int_{\Gamma_{h_2}} w \, T \, dS \tag{6.11}$$

In the cracked, but not completely decohered element, sub-element 1 has local nodal displacements given by, $\{u\} = [u_1 \ u_2 \ u_3 \ u_4 \ u_7 \ u_8 \ u_9 \ u_{10}]^T$ and sub-element 2 has local nodal displacements given by, $\{u\} = [u_{11} \ u_{12} \ u_{13} \ u_{14} \ u_5 \ u_6]^T$ as shown in Fig. 6.7(c). The corresponding virtual nodal displacements are $\{w^e\} = [w_1 \ w_2 \ w_3 \ w_4 \ w_7 \ w_8 \ w_9 \ w_{10}]^T$ and $\{w\} = [w_{11} \ w_{12} \ w_{13} \ w_{14} \ w_5 \ w_6]^T$. The terms of Equation 6.10 can be expressed in terms of the following displacement fields:

$$\int_{\Omega_1} \nabla w : \sigma \; dV = \{w_1\}^T_{(6,1)} \left[\int_{\Omega_1} \mathbf{B_1^T D B_1} \; dV \right]_{(6,6)} \{U_1\}_{(6,1)}$$

$$\int_{\Omega_2} \nabla w : \sigma \; dV = \{w_2\}^T_{(8,1)} \left[\int_{\Omega_2} \mathbf{B_2^T D B_2} \; dV \right]_{(8,8)} \{U_2\}_{(8,1)}$$

$$\int_{\Gamma_{h_1}} w \; T \; dS + \int_{\Omega_1} w \; f \; dV = \{w_1\}^T_{(6,1)} [F_1]_{(6,1)} \tag{6.12}$$

$$\int_{\Gamma_{h_2}} w \; T \; dS + \int_{\Omega_2} w \; f \; dV = \{w_2\}^T_{(8,1)} [F_2]_{(8,1)}$$

$$\int_{\Gamma_3} w \; T_1(\delta_I) dS + \int_{\Gamma_3} w \; T_2(\delta_{II}) dS = \{w_3\}^T_{(8,1)} \; T(\delta_I, \delta_{II})$$

where, B_1 and B_2 are strain-displacement relations of Ω_1 and Ω_2. δ_I and δ_{II} are mode-I and mode-II jump displacements at the interface between Ω_1 and Ω_2.

Linearizing Equation 6.11 and rearranging the terms, we obtain an enhanced system of equations corresponding to enhanced nodal displacement field given by,

$$U_e = \begin{bmatrix} u_e \\ \hat{u}_e \end{bmatrix} \tag{6.13}$$

where, $u_e = [u_1 \; u_2 \; u_3 \; u_4 \; u_5 \; u_6]^T$, and $\hat{u}_e = [u_7 \; u_8 \; u_9 \; u_{10} \; u_{11} \; u_{12} \; u_{13} \; u_{14}]^T$.

The corresponding enhanced element stiffness matrix and force vector are given by,

$$K_e = \begin{bmatrix} K^e_{11(6,6)} & K^e_{12(6,8)} \\ K^e_{21(8,6)} & K^e_{22(8,8)} \end{bmatrix} \tag{6.14}$$

$$F_e = \begin{bmatrix} F_{e(6,1)} \\ \hat{F}_{e(8,1)} \end{bmatrix} \tag{6.15}$$

From static condensation, the equivalent stiffness matrix and the force vector of the element can be derived as,

$$[K_{11}^e - K_{12}^e {K_{22}^e}^{-1} K_{21}^e]\{u_e\} = \{\bar{F}_e\} \tag{6.16}$$

$$\{\bar{F}_e\} = \{F_e\} - K_{12}^e {K_{22}^e}^{-1}\{\hat{F}\} \tag{6.17}$$

Therefore, the equivalent stiffness of the cracked element is,

$$[K_e^{eq}] = [K_{11}^e - K_{12}^e {K_{22}^e}^{-1} K_{21}^e] \tag{6.18}$$

Thus, the contribution of the decohered element to the global system is through the original nodal displacements of the continuum triangle element, and is given by,

$$[K_e^{eq}]\{u_e\} = \{\bar{F}_e\} \tag{6.19}$$

$[K_e]$ has contributions from the two sub-elements (triangular element and quadrilateral element) and the interface tractions. The stiffness contributions of the triangular and quadrilateral elements are derived in the same way as any regular continuum element.

The entire procedure for implementing the CDFE method is illustrated in Fig. 6.8 and Fig. 6.9.

1. At increment 'n', $\underline{d}_{n-1}$ is known.

   (a) If 'k' is the current iteration:

   (b) Residual : $\underline{R}\left(\underline{d}_{n-1}^{k}\right) = \underline{K}\,\underline{d}_{n-1}^{k} - \underline{f}_{n}^{ext}$

   (c) If $\underline{R}\left(\underline{d}_{n-1}^{k}\right) \leq TOL \Longrightarrow$ exit. $\underline{d}_{n} = \underline{d}_{n-1}^{k}$
   Else : Carry out Newton-Raphson (N-R) Iterations until $\underline{R}\left(\underline{d}_{n-1}^{k}\right) \leq TOL$ $\Longrightarrow$ exit. $\underline{d}_{n} = \underline{d}_{n-1}^{k} + \delta\underline{d}_{n-1}^{k}$

   (d) Determine $\vec{\sigma}$ for each element. Rotate $\vec{\sigma}$ along fiber direction.

   (e) Check for crack initiation in each element using failure criterion.
   If the criterion is not satisfied within a certain percentage (1%), reduce the increment size by a factor, go back to Step 1, and perform Steps a-e.
   Else, if the transition criterion is satisfied within a certain percentage (1%) $\Longrightarrow$ Separate the element along/perpendicular to fiber direction at the centroid of the element. Determine the modified element stiffness and force vector, and continue.

   (f) With modified assembled stiffness $\underline{K}$ and force vector $\underline{f}$, carry out N-R iterations. Solve for $\underline{d}_{n}$.

   (g) Check if the cohesive sub-element has met the failure criterion:
   If $\frac{G_I}{G_{IC}} + \frac{G_{II}}{G_{IIC}} \geq 1$: Element has broken completely

   Else, Element on the softening curve of the cohesive law

   (h) Store all information of softening elements, and continue to next increment(Step 1)

Figure 6.8: Algorithm for the CDFE method

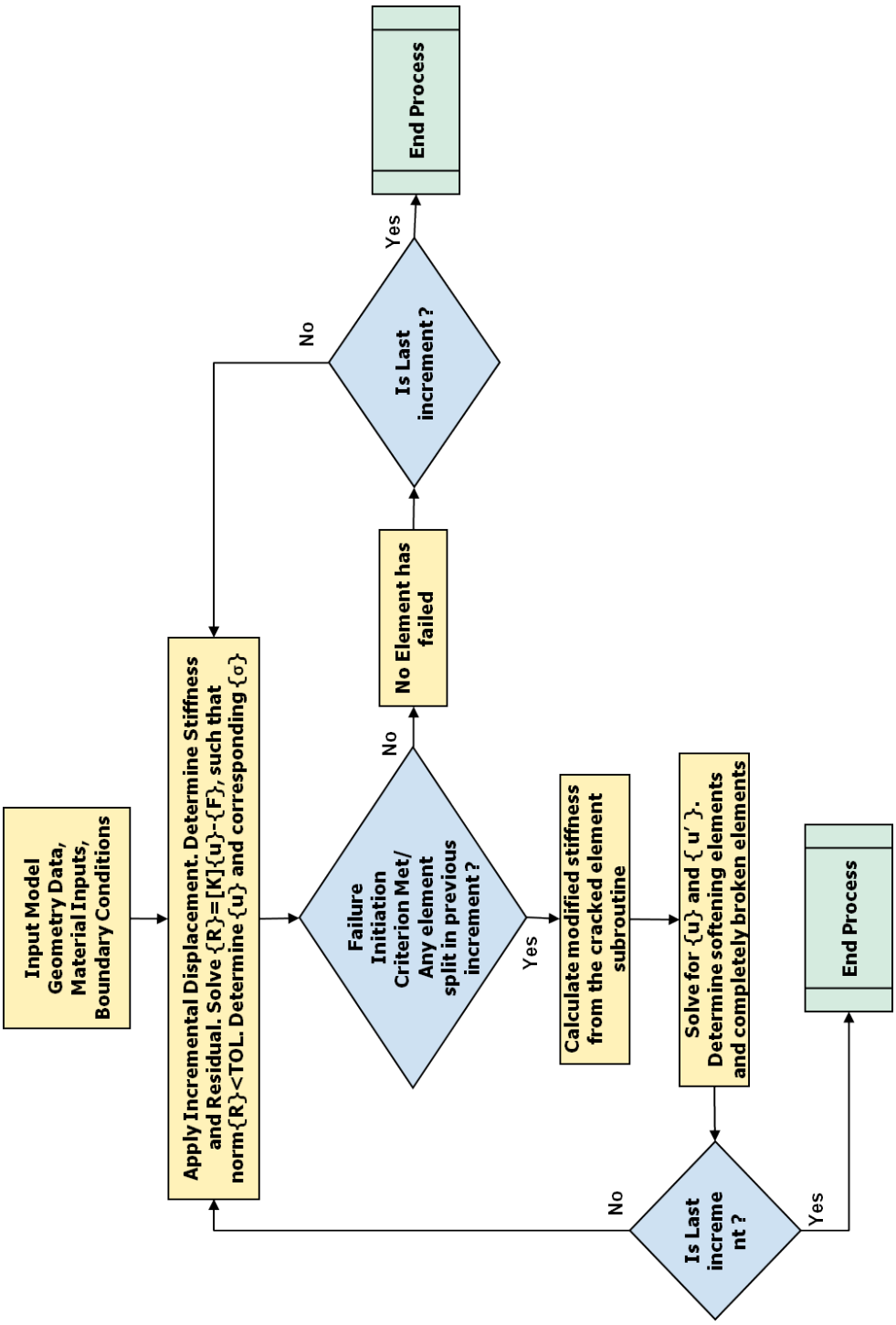

Figure 6.9: A flowchart describing the procedure for the CDFE method

6.6 Open Hole Tension Simulations : Fracture of Matrix Parallel to Fiber Direction

The above finite element formulation has been implemented in an in-house code through a high-level technical computing language and interactive environment within MATLAB. The method is demonstrated by modeling the open hole tension test of 90, 45 and 0 degree lamina, for which a set of experimental results is also available. The lamina material properties are as follows: E_{11}=136 GPa, E_{22}=6.7 GPa, ν_{12}=0.33, G_{12}=3.2 GPa; In addition, the mode I and mode II fracture toughness values are, 0.67 N/mm and 1.67 N/mm respectively, and the mode I and mode II cohesive strengths are 60 MPa and 90 MPa, respectively.

Fig. 6.10 shows the schematic of an open hole specimen subjected to tension. The fiber orientation angle θ is 90 degrees. The corresponding load-load-point extension plots, which show the unstable failure paths for different mesh sizes, are given in Fig. 6.11.

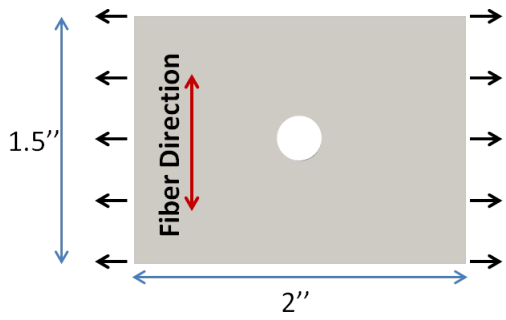

Figure 6.10: Schematic of a 90 degree lamina with a hole subjected to tension

Mesh refinement is carried out along the expected crack path to investigate the influence of mesh size on the global response of the model, as shown in Fig. 6.12. Similar mesh refinement is also carried out for the 45 degree and 0 degree lamina tensile tests investigated further.

Fig. 6.13 shows the evolving displacements and subsequent cracking of a trans-

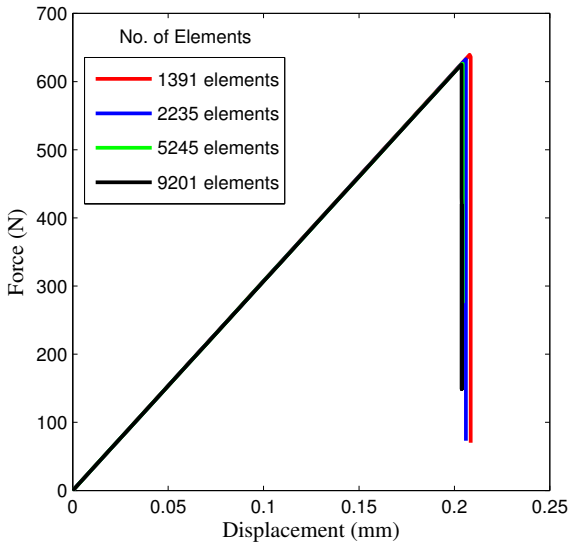

Figure 6.11: Load - load-point extension plot of 90 degree plate with a hole

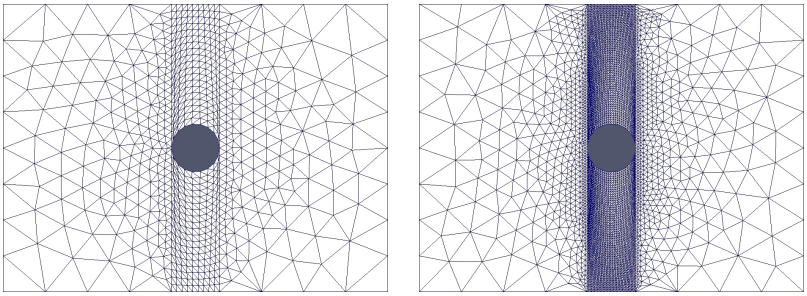

(a) (b)

Figure 6.12: Mesh refinement along the expected crack path; (a) Coarse and (b) Fine

versely loaded single ply. At a critical value of the far-field tension, fracture in mode-I (opening mode), with a crack propagating along the fiber direction (parallel to the fibers) is seen to emerge at the edge of the hole and propagates uninhibitedly, rendering catastrophic failure.

Similarly, the tensile response of an open hole lamina with fiber orientation $\theta = 45$ degrees with respect to the loading direction is also demonstrated. The load - load point displacement responses are plotted for different mesh densities and compared with experimental results in Fig. 6.15. It should be noted here that, the simulation with 1114 elements does not have enough elements for the regular FEM to converge, and therefore, it does not fall in the pathological mesh dependency case study.

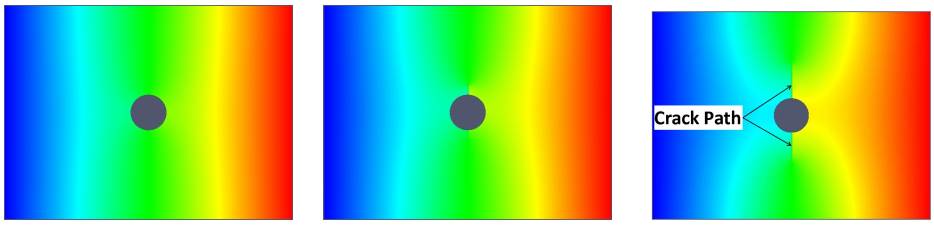

Figure 6.13: Displacement field from the simulation of a 90 degree lamina with a hole in tension at different loading stages; (a) Initial region, (b) Peak load and (c) Post-peak region

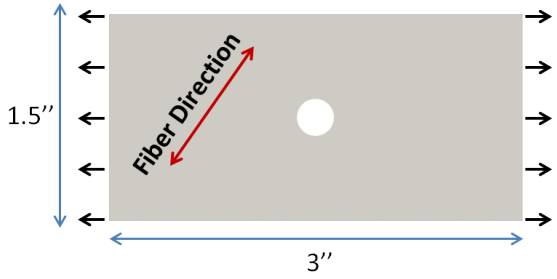

Figure 6.14: Schematic of a 45 degree lamina with a hole subjected to tension

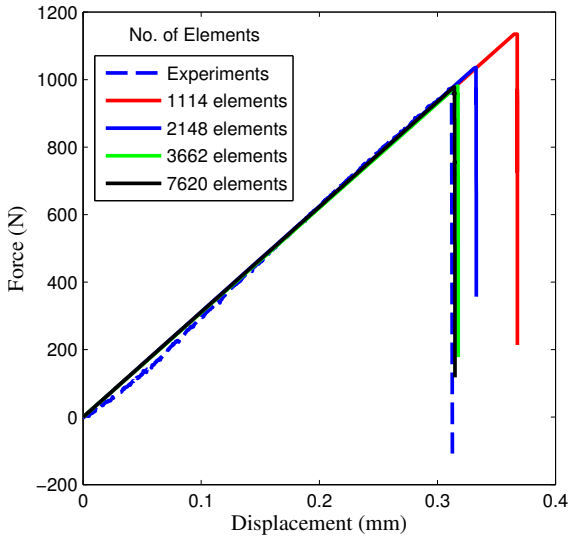

Figure 6.15: Load - load-point extension plot of 45 degree plate with a hole

Here, mixed mode fracture is observed. That is because, along the crack path, both the shear tractions and normal tractions are found to be active. Since the crack is constrained to grow along the fibers or perpendicular to the fibers, the crack tip

stress state will involve a combination of stresses. It is observed that the lamina fractures at an angle 45 degrees to the loading direction, as shown in Fig. 6.16.

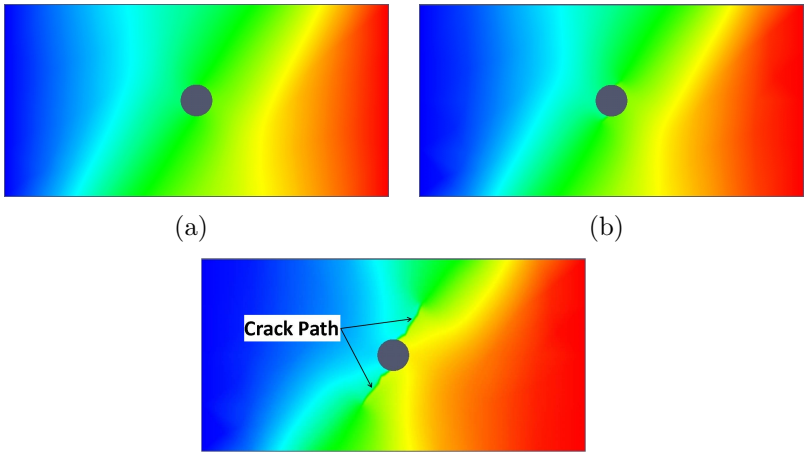

Figure 6.16: Displacement field from the simulation of a 45 degree lamina with a hole in tension at different loading stages; (a) Initial region, (b) Peak load and (c) Post-peak region

Tensile tests were conducted on open hole specimens with fibers orientated at 45 degrees to the loading direction. The face of the laminate was speckled with black dots on a white surface. Images were recorded at fixed intervals during testing. The speckle data was analyzed using digital image correlation method to obtain the strain fields. The axial strain field, i.e. along the x-direction, is shown in Fig. 6.17(a) and Fig. 6.17(b) at an initial loading stage and at the peak load, respectively. The predicted strain behavior of the 45 degree lamina, shown in Fig. 6.17(c) and Fig. 6.17(d), corresponding to an initial loading stage and at the peak load, matches well with the experiments.

Finally, a 0 degree lamina with a hole subjected to tension is studied. A schematic of the model is shown in Fig. 6.18. The load - load point displacement responses are plotted for different mesh densities and compared with experimental results in Fig. 6.19. In the experimental load - load point displacement response, the lamina slips out of the grips causing the load to drop after a peak load is reached. But,

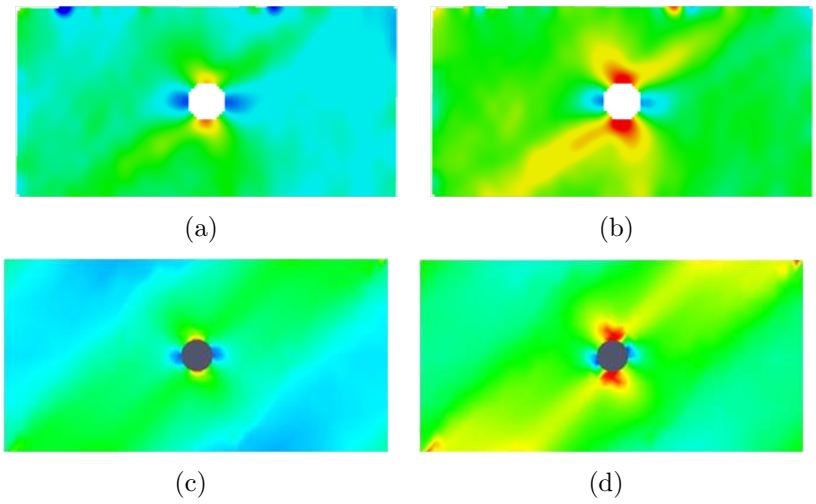

Figure 6.17: Axial strain field from DIC analysis of a 45 degree lamina with a hole in tension at different loading stages; (a) Initial region and (b) Peak load, and corresponding CDFE analysis in (c) and (d)

the grips in the simulation are intact, and therefore, the load continues to increase beyond the peak load from the experiments, but the global stiffness of the response is slightly reduced as compared to the initial part of the response. Similar behavior for a notched 0 degree laminate has also been reported in *Bogert et al.* (2006), and simulated using a crack band model in, *Pineda and Waas* (2012). The failure of the 0 degree lamina open hole tension test is dominated by mode-II failure, and a characteristic longitudinal crack, which emerges at the hole edge, is seen to propagate away from the hole and along the fiber direction. The corresponding deformation plots of the lamina are shown in Fig. 6.20(a), Fig. 6.20(b) and Fig. 6.20(c).

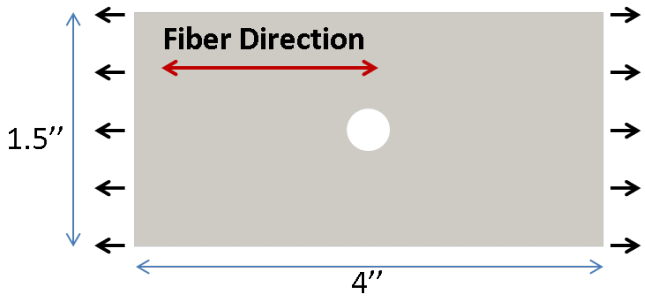

Figure 6.18: Schematic of a 0 degree lamina with a hole subjected to tension

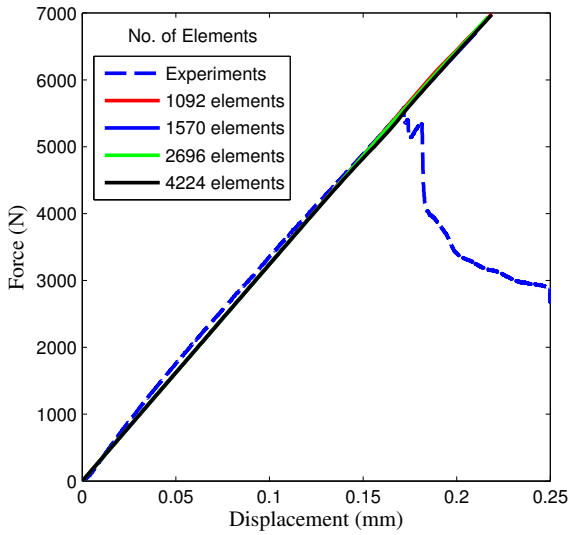

Figure 6.19: Load - load-point extension plot of 0 degree plate with a hole

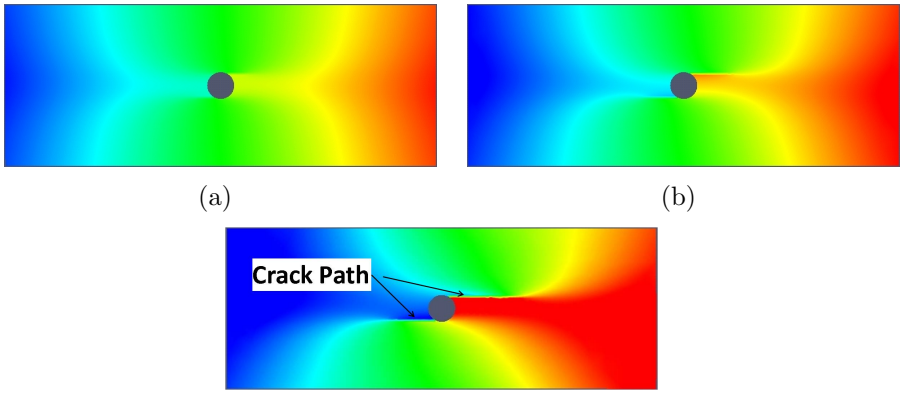

Figure 6.20: Displacement field from the simulation of a 0 degree lamina with a hole in tension at different loading stages; (a) Initial region, (b) Peak load and (c) Post-peak region

The experimentally obtained DIC strain fields of a 0 degree lamina was also obtained as in the case of a 45 degree lamina. The splitting fracture occurs along the fiber direction, and propagates through the length of the specimen, starting at the hole edge. Experimental strain fields at an initial stage and at the peak load are shown in Fig. 6.21(a) and Fig. 6.21(b), respectively. These shear strain fields obtained from experiment closely match those corresponding to the predictions from numerical simulations (shown in Fig. 6.21(c) and Fig. 6.21(d)).

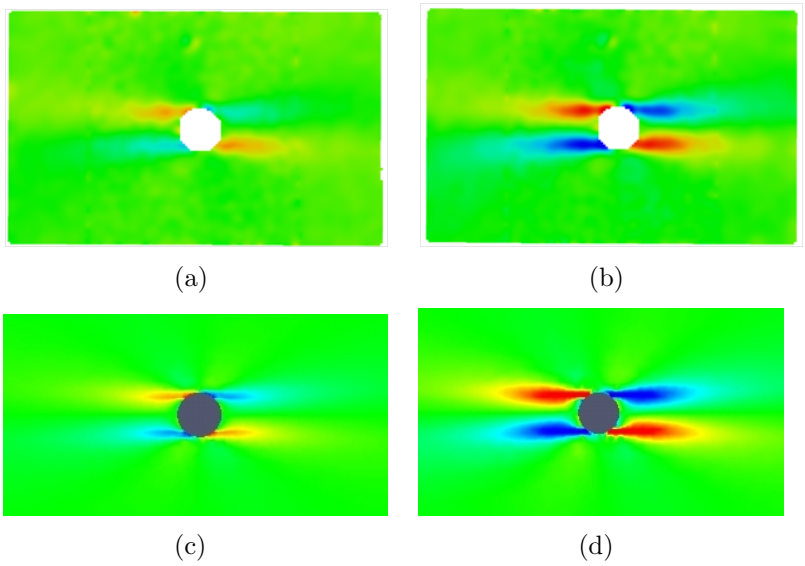

Figure 6.21: Shear strain field from DIC analysis of a 0 degree lamina with a hole in tension at different loading stages; (a) Initial region and (b) Peak load, and corresponding CDFE analysis in (c) and (d)

6.7 Discussion and Concluding Remarks

The CDFE method proposed has the potential to be used in predicting in-plane failure by fracture in laminated composites, as demonstrated through the single lamina examples that have been studied. The predictions converge to a single response with mesh refinement. Therefore, pathological mesh dependency is not observed in this method. Fracture by splitting can also be captured by a crack band model, *Pineda and Waas* (2012) or smeared crack model, *Heinrich and Waas* (2012), which are weak discontinuity implementations, whereas, the present CDFE and VMCM methods are strong discontinuity methods allowing the crack path to be independent of the element boundaries. The CDFE formulation has a few caveats. The triangle element can virtually decompose only into a triangle and a quadrilateral element. This may render the problem ill-conditioned if the intended crack-path is very close to any one of the nodes of the original triangular element. A method to circumvent this issue is to allow the triangle to decompose into either two triangles, or one triangle and one quadrilateral. Such a general implementation is ongoing.

As with any post-peak, strain softening capturing numerical method, the predicted response in the post-peak regime is dependent on the characteristic length scales, defined by, $l_1 = \frac{E_{xx}G_{IC}}{\sigma_C^2}$ and $l_2 = \frac{G_{xy}G_{IIC}}{\tau_C^2}$ in mode-I and mode-II, respectively, *Yerramalli and Waas* (2004b). That is, stable crack path and response is observed when the lengths l_1 and l_2 are sufficiently large, making the failure more "ductile", whereas, unstable response is observed when these lengths are small compared to the current crack length, rendering the failure to be brittle. In the case of brittle failure, the dynamic equations of motion will need to be considered, since an initiated crack will propagate a finite distance prior to attaining an equilibrium state (if any exists) For such cases, an explicit solution scheme is more suitable. Notwithstanding these issues, the CDFE can be used for cases that are presently studied using standard cohesive zone methods and VMCM. Furthermore, the CDFE can be implemented in a straight-forward manner, using existing element libraries without recourse to special shape functions for enrichment.

The open hole lamina tension predictions carried out to demonstrate the CDFE approach shows its efficiency in capturing transitions from continuum response to fracture in a seamless manner. The predicted results compared well against experimental results for laminae loaded remotely at different angles to the fiber direction.

CHAPTER VII

Conclusion and Original Contributions

In this thesis, a novel computational modeling framework to predict the compressive strength of fiber reinforced polymer matrix composite (FRPC) laminates has been presented. The model development was motivated by a set of experimental results on the compression response of two different FRPCs. The experimental results showed that both failure mode and failure load were influenced by the laminate stacking. Furthermore, the two dominant failure modes, kink-banding in the on-axis (zero degree lamina) layers and delamination between differently oriented laminae, were found to be present. Digital image correlation (DIC) measurements clearly showed that prior to failure, the (+45/-45) interfaces delaminated prior to global failure in one type of laminate (laminate with o degree layers clustered along the centerline), while the two modes of kinking in zero plies and delamination appeared almost simultaneously in the other type of laminates (laminate with 0 degree layers distributed through the thickness of the laminate).

The computational model that was presented included interface elements to capture delamination and a micromechanical approach to capture kink-banding. Furthermore, a homogenization procedure to reduce micromechanical considerations of the off-axis layers was introduced. To reduce the size of the computational model, those interfaces that are most susceptible to delamination were first determined through

a free-edge stress analysis. The inputs to implement the model, which consist of fracture properties of interfaces and the nonlinear shear response of the matrix material, were measured for the composite material system studied in this thesis. The predictions of the model matched well with the experimental observations, and were found to accurately account for failure mechanism interactions. Therefore, this model can replace the need to carry out large numbers of tests to obtain the compressive strength allowable for FRPC laminates. This allowable is an essential element in the design of lightweight FRPC aerostructures. Furthermore, in the spirit of the integrated computational materials engineering (ICME) national thrust, *Committee on Integrated Computational Materials Engineering* (2008), the model that is presented here can easily be extended to account for the autoclave manufacturing process of the laminates, by introducing residual stresses due to cure shrinkage of the matrix.

In the latter part of the thesis, a new computational model to predict fiber-matrix splitting failure, a failure mode that is frequently observed in in-plane tensile failure of FRPC's, was also presented. By considering a single lamina, this failure mechanism was seamlessly modeled through the development of a continuum-decohesive finite element (CDFE). The CDFE was motivated by the variational multiscale cohesive method (VMCM) presented earlier by *Rudraraju et al.* (2010) at the University of Michigan. In the CDFE, the transition from a continuum to a non-continuum is modeled directly (physically) without resorting to enriching the shape functions of the element. Thus, the CDFE is a natural merger between cohesive elements and continuum elements. The predictions of the CDFE method were also found to be in very good agreement with corresponding experimental observations.

Provided below are suggestions for future studies:

- The details of *in-situ* degradation in a lamina are due to formation of matrix cracks (microcracks) within the fibers as shown by [*Ng et al.* (2010)]. This mechanism can be modeled directly and would aid in the elimination of a off-

axis (+45/-45) test to characterize the in-situ shear response of the matrix material. Thus, the upscaling procedure developed here can be combined with the micromechanics model to develop a virtual method that uses only fiber and matrix properties

- When kink bands are observed, the band boundary shows a line of broken fibers. Thus, fiber breaking an be incorporated in the computational model through a CDFE approach (presented in this thesis) or a smeared crack approach (presented in *Heinrich and Waas* (2012)).

- Both the micromechanics models and the upscaled models can incorporate processing induced thermal effects to predict manufacturing induced effects in the laminates. This would fit in well within the broader ICME framework for FRPCs.

- Extend the CDFE formulation to incorporate the dynamics of failure. This would necessitate using explicit solutions schemes of the resulting finite element equations.

APPENDICES

APPENDIX A

Concentric Cylinder Model Equations

The homogenized lamina properties are obtained using a concentric cylinder model (CCM) shown in Fig. A.1. The CCM equations for equivalent lamina properties [*Hashin and Rosen* (1964), *Hill* (1964), *Pankow* (2010)] are as follows;

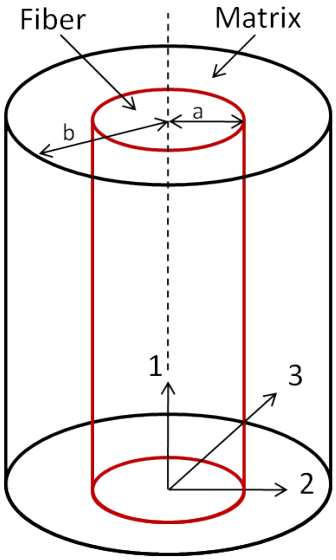

Figure A.1: A sketch of the concentric cylinder model with fiber volume fraction $V_f = \frac{a^2}{b^2}$

Axial modulus :

$$E_1 = E_1^f(1+\gamma)V^f + E^m(1+\delta)(1-V^f) \tag{A.1}$$

where,

$$\gamma = \frac{2\nu_{21}^f E^m(1-\nu_{23}^f-2\nu_{12}^f\nu_{21}^f)V^f(\nu_{12}^f-\nu^m)}{E_2^f(1+\nu^m)(1+V^f(1-2\nu^m))+E_m(1-\nu_{23}^f-2\nu_{12}^f\nu_{21}^f)(1-V^f)} \tag{A.2}$$

$$\delta = \frac{2E_2^f\nu^m V^f(\nu^m-\nu_{12}^f)}{E_2^f(1+\nu^m)(1+V^f(1-2\nu^m))+E_m(1-\nu_{23}^f-2\nu_{12}^f\nu_{21}^f)(1-V^f)} \tag{A.3}$$

Transverse modulus :

$$E_2 = \frac{1}{\frac{\eta^f V^f}{E_2^f}+\frac{\eta^m(1-V^f)}{E^m}} \tag{A.4}$$

$$E_3 = E_2 \tag{A.5}$$

where,

$$\eta^f = \frac{E_1^f V^f + \left[(1-\nu_{12}^f\nu_{21}^f)E^m+\nu^m\nu_{21}^f E_1^f\right](1-V^f)}{E_1^f V^f + E^m(1-V^f)} \tag{A.6}$$

$$\eta^m = \frac{[(1-\nu^{m^2})E_1^f-(1-\nu^m\nu_{12}^f)E^m]V^f+E^mV^m}{E_1^f V^f+E^m(1-V^f)} \tag{A.7}$$

Poisson's ratio :

$$\begin{aligned}\nu_{12} &= \frac{[(1-V^f)(1-\nu_{23}^f-2\nu_{12}^f\nu_{21}^f)]\nu^m E^m}{((1-V^f)(1-\nu_{23}^f-2\nu_{12}^f\nu_{21}^f))E^m+(1+V^f+(1-V^f)\nu^m-2V^f\nu^{m^2})E_2^f} \\ &+\frac{[\nu^m+V^f(2\nu_{12}^f-\nu^m)+(\nu^{m^2}(1-2V^f\nu_{12}^f-V^f))]E_2^f}{((1-V^f)(1-\nu_{23}^f-2\nu_{12}^f\nu_{21}^f))E^m+(1+V^f+(1-V^f)\nu^m-2V^f\nu^{m^2})E_2^f}\end{aligned}$$

Shear modulus :

$$G_{12} = G^m\left[\frac{(G^m+G_{12}^f)-V^f(G^m-G_{12}^f)}{(G^m+G_{12}^f)+V^f(G^m-G_{12}^f)}\right] \tag{A.8}$$

$$G_{13} = G_{12} \tag{A.9}$$

$$G_{23}^{*} = \frac{1}{\frac{\frac{1}{G_{23}^{f}} V^{f} + \eta_4 \frac{1}{G^{m}} (1 - V^{f})}{V^{f} + \eta_4 (1 - V^{f})}} \tag{A.10}$$

where,

$$\eta_4 = \frac{3 - 4\nu^{m} + \frac{G^{m}}{G_{23}^{f}}}{4(1 - \nu^{m})} \tag{A.11}$$

Subscripts f and m refer to the fiber and matrix phases. E represents the modulus, G the shear modulus, V the volume fraction, ν poisson's ratio. The 1 axis is in the fiber direction as shown in Figure A.1.

APPENDIX B

Interaction between Kinking and Splitting in the Compressive Failure of Unidirectional Fiber Reinforced Laminated Composites

This appendix is a paper that is published in *Composites Structures* [*Prabhakar and Waas* (2012c)], and addresses the topic of interactive failure in unidirectional laminates. Since, the focus of the thesis is on the interactive failure in multidirectional laminates, the preliminary work carried out for unidirectional laminates is presented here.

Introduction

Fiber kink banding has been identified as a compressive strength limiting mechanism in aligned fiber reinforced composite laminates that are finding increasing use in lightweight aerostructures, (*Schultheisz and Waas* (1996) and *Waas and Schultheisz* (1996)). While early studies determined that the compressive strength can be determined by a knowledge of the shear nonlinearity in the stress-strain response of a lamina in tandem with a knowledge of initial fiber misalignment (*Budiansky and*

Fleck (1993) and *Schapery* (1995)), it was later determined through a combination of experiments and numerical modeling that the kink band formation is an evolutionary process, which is governed by local stress state (including stress multi-axiality), details of the material constitutive model and the fiber misalignment angles as explained in papers by *Sun and Jun* (1994), *Kyriakides et al.* (1995), *Lee and Waas* (1999), *Vogler et al.* (2001), *Yerramalli and Waas* (2003), *Yerramalli and Waas* (2004a), *Basu et al.* (2006), *Pimenta et al.* (2009a), *Pimenta et al.* (2009b), *Feld et al.* (2011). As loading proceeds, regions of fiber misalignment in the composite undergo deformation due to combined compression and shear loading. This region is surrounded by other material whose deformation characteristics, in general, are different. The progressively increasing local fiber misalignment coupled with a softening shear nonlinearity, perpetuates a local limit-load type instability that initiates a rapid formation of a kink band. During this formation, the external tractions required to support the structure, in general, decrease, indicating an instability. The regions within the band undergo large straining while material outside the band, relaxes and unloads. Consequently, the mechanics of this process is related to the local microstructural details, geometry and volumes of material that are occupied by the band and that are outside the band.

Lee and Waas (1999), *Lee et al.* (2000), *Vogler et al.* (2001), *Pimenta et al.* (2009a) and *Pimenta et al.* (2009b), have shown that kink-band formation can also involve splitting in combination or in isolation of the band formation. *Lee and Waas* (1999) studied the effect of fiber volume fraction on the compressive failure mode, while *Yerramalli and Waas* (2003) studied the effect of fiber type and load multi-axiality on failure. In both these studies energy released by splitting failure in combination with kinking was identified as contributing to the failure mechanism. Since the strains within the band can become in excess of the tolerable strain limits of the matrix and/or the fiber/matrix interface, it is conceivable that energy released by splitting is another mechanism by which energy is dissipated in the process of kink-band for-

mation, in addition to the nonlinear volumetric energy released by the matrix. The formation of kink banding as an energy release mechanism in limiting the compressive strength of laminates with cut-outs has previously been addressed by *Waas et al.* (1990), *Ahn and Waas* (1999), *Ahn and Waas* (2002), and *Berbinau et al.* (1999), while the influence of fiber waviness on compressive failure of unidirectional laminates has been studied by *Wisnom* (1994). Micromechanical models to predict compressive strengths have been proposed by *Naik and Kumar* (1999), and *Xu and Reifsnider* (1993), while the high strain rate response in compression has been addressed in *Guedes et al.* (2008), *Ochola et al.* (2004), *Pintado et al.* (2001) and *Hosur et al.* (2001). Typical values of experimental compressive strength (X_C) of modern fiber reinforced lamina (0^0 degree plies) are tabulated in Table B.1.

Table B.1: Compressive strength of unidirectional fiber reinforced lamina

Material Description	X_C (MPa)	Reference
APC-2/AS4 Composite	1044-1156	*Kyriakides et al.* (1995)
Glass-Fiber composites, V_f=0.4-0.6	650-880	*Lee and Waas* (1999)
Carbon fiber HM-S/Epoxy, V_f=0.45-0.55	650-690	*Lo and Chim* (1992)
Carbon fiber HM-S/Epoxy, V_f=0.5-0.6	735-780	*Hancox* (1975)
Carbon fiber HM-S/Epoxy, V_f=0.45-0.5	580-585	*Martinez et al.* (1981)
Boron fiber/Epoxy, V_f=0.45	800	*Lager and June* (1969)
Carbon fiber HT-S/Epoxy, V_f=0.4-0.5	840-1030	*Lo and Chim* (1992)
Carbon fiber HT-S/Epoxy, V_f=0.4-0.5	910-1095	*Hancox* (1975)
T 300/5208, V_f=0.59	1228	*Lo and Chim* (1992)

This chapter is concerned with the interaction between splitting and kink-banding in the compressive failure of composites, studied by using a micromechanics based 2D finite element model representation of the composite. The details of the representative volume element of a fiber matrix composite that is suitable for understanding and delineating the most important aspects of determining the compressive strength is also examined. While splitting is governed by the fracture properties of the matrix and/or fiber matrix interface, the kink banding is governed by the nonlinear response

of the matrix material in a misaligned fiber composite, (*Prabhakar and Waas* (2012b), *Yerramalli and Waas* (2004b)). First, the minimum size of computational model required to determine a converged value of compressive strength of the laminate is established. This is followed by an interactive failure model that includes discrete cohesive zone elements (DCZM) added along the interface between fibers and matrix, allowing for kinking and splitting failure mechanisms to interact. Here, a parametric study is carried out with different sets of values for the fracture properties, in order to extract the compressive strength limiting mechanism.

Determining critical model size

Modeling overview

2-D finite element representative micromechanics models of carbon fiber reinforced polymer (CFRP) matrix unidirectional laminates are examined in this chapter. Since, one of the goals is to investigate the effects of model size on the compressive strength, scaled micromechanics models preserving a fixed fiber volume fraction and aspect ratio are considered. The fiber volume fraction and aspect ratio (length/cross-section height of the model) are maintained at 50% and 2 respectively. It has been shown by *Yerramalli and Waas* (2004a) that there is no significant difference in response between 2-D models and 3-D models for composites with high fiber volume fraction and low imperfection. That is, the difference in the response of 2-D model and 3-D model increases with increase in imperfection angles. Since, aerospace grade laminates have low imperfections (*Yurgartis* (1987)), 2-D models can be used as opposed to 3-D models. Further, the response of 2-D model is in very good agreement with 3-D model if the fibers are regularly spaced making the laminate periodic in the third dimension. Therefore, 2-D models are adopted for computational expediency and because they capture the essential details of the mechanisms associated with compressive response

for fiber volume factions in excess of 50%. The smallest model consists of 6 fibers, followed by 12, 24, 48 and 96 fibers. Since, the aspect ratio and fiber volume fractions are held fixed in all the models, the global size of the models increase by a factor of 2 as compared to the previous size. Therefore, if the smallest model i.e. size 1 model has a dimension of 0.12 mm x 0.06 mm, the size 2 model has dimensions of 0.24 mm x 0.12 mm, and size 3 has dimensions of 0.48 mm x 0.24 mm (refer to Table B.2).

Table B.2: Dimensions and number of fibers in different size models

	Number of fibers	Length (mm)	Width (mm)
Size 1	6	0.12	0.06
Size 2	12	0.24	0.12
Size 3	24	0.48	0.24
Size 4	48	0.96	0.48
Size 5	96	1.96	0.96

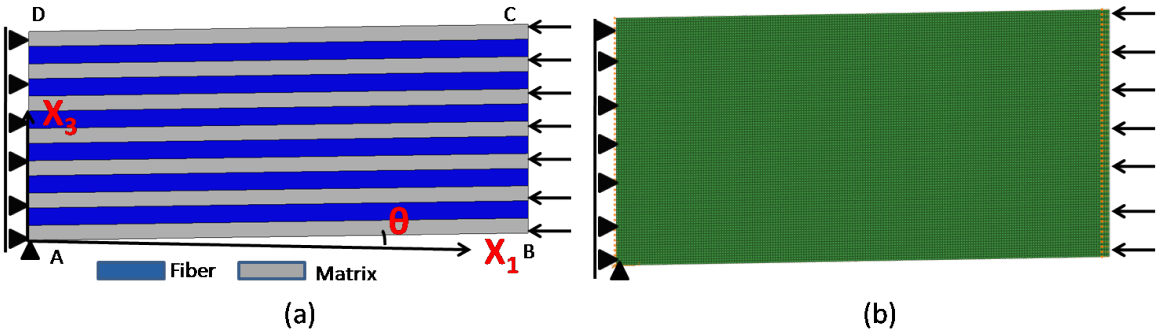

Figure B.1: a) 6 fiber model of a unidirectional composite; (b) Meshed model of the laminate

A schematic of a 2-D unidirectional composite along with the boundary conditions prescribed and subjected to compression is shown in Fig. B.1(a). A displacement controlled uniform compressive loading is applied on edge BC as shown in Fig. B.1(a). Also, a meshed model with boundary conditions applied is shown in Fig. B.1(b). The fiber diameter is fixed at 0.005 mm, which is representative of carbon fibers in aero-structural laminates. An initial ply misalignment of 1 degree is imparted to all the

models, as seen in Fig. B.1(a) represented by an angle θ (=1) degrees. Previous work by *Yurgartis* (1987) has shown that initial misalignment angles of 0.5 to 2 degrees bound the distribution of fiber misalignment that is typical of carbon fiber reinforced aero-structural laminates.

Table B.3: Fiber properties (*Lee and Waas* (1999))

E_{11} (GPa)	E_{22} (GPa)	E_{33} (GPa)	G_{12} (GPa)	G_{13} (GPa)	G_{23} (GPa)	ν_{12}	ν_{13}	ν_{23}
276	8.76	8.76	12.0	12.0	3.244	0.35	0.35	0.35

Fibers are assumed to be orthotropic and linearly elastic. The orthotropic properties of the carbon fiber are given in Table B.3, taken from *Lee and Waas* (1999). The degrading polymer matrix is modeled as an isotropic elastic-plastic governed by J2 incremental theory of plasticity, (*Lubliner* (2008)). It should be noted that plasticity is one of the many ways to approximate nonlinearity of a material. But, plasticity is adopted here as a way of modeling nonlinearity induced in the model due to matrix nonlinearity. The equivalent stress-equivalent strain response of the in-situ matrix, which corresponds to it's uniaxial stress-strain response is shown in Fig. B.2.

To establish the baseline compression response, the scaled models are assumed to have a perfect interface between fibers and matrix. This implies that the fibers are restricted from splitting from the matrix. Four noded, bilinear quadrilateral elements (CPE4 in the ABAQUS code) with a characteristic length of 0.0015 mm (i.e. at least 3 elements through the thickness of the fiber) and non-linear geometry are used for the fibers and matrix in all 2D (plane strain) analyses reported in this chapter. Due to the initial ply misalignment, and along with non-linear geometry used, the possibility of an unstable snap-back response is accommodated by employing the arc-length based Riks solver in the ABAQUS code, *ABAQUS* (6.10).

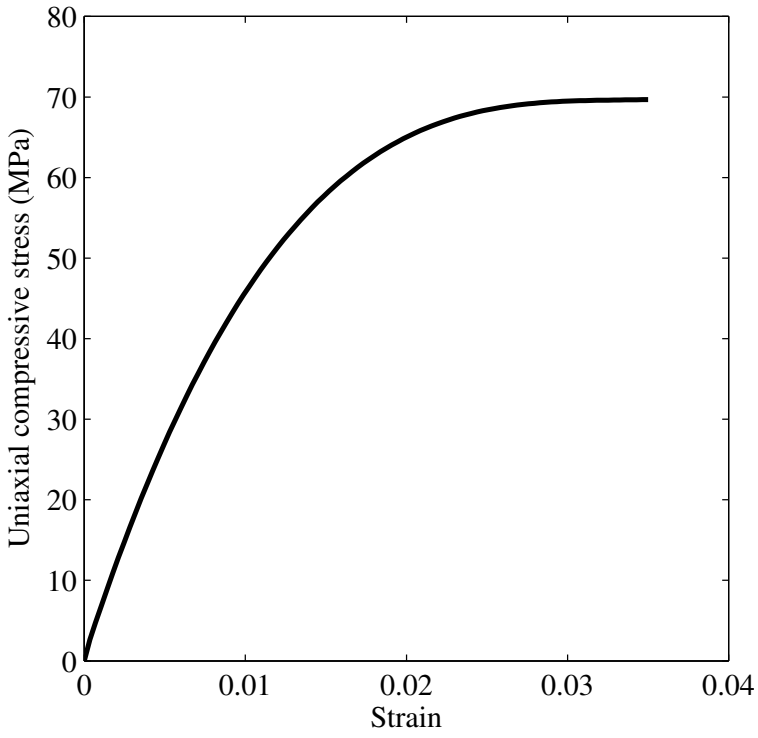

Figure B.2: Uniaxial compressive stress-strain curve of the in-situ matrix

Results

Fig. B.3 shows a global compressive stress-strain curve along with a series of deformed shapes of the size 3 model, corresponding to the loading history. Point A corresponds to the initial linear path, point B corresponds to the peak stress, point C lies in the snap back regime and point D represents the plateau region of the macroscopic stress-strain response shown in Fig. B.3.

For all sizes of the model (given in Table B.2), corresponding global compressive stress-strain curves are determined. In all the responses, an initial linear macroscopic stress-strain response is terminated by a peak stress, followed by a progressively decreasing stress-increasing strain branch or a snap-back branch as shown in Fig. B.4.

The snap-back branch becomes more prominent as the model size increases. It is observed that the peak stress increases initially with an increase in model size, and gradually asymptotes to a converged value (from 704 MPa to 730 MPa). It is also

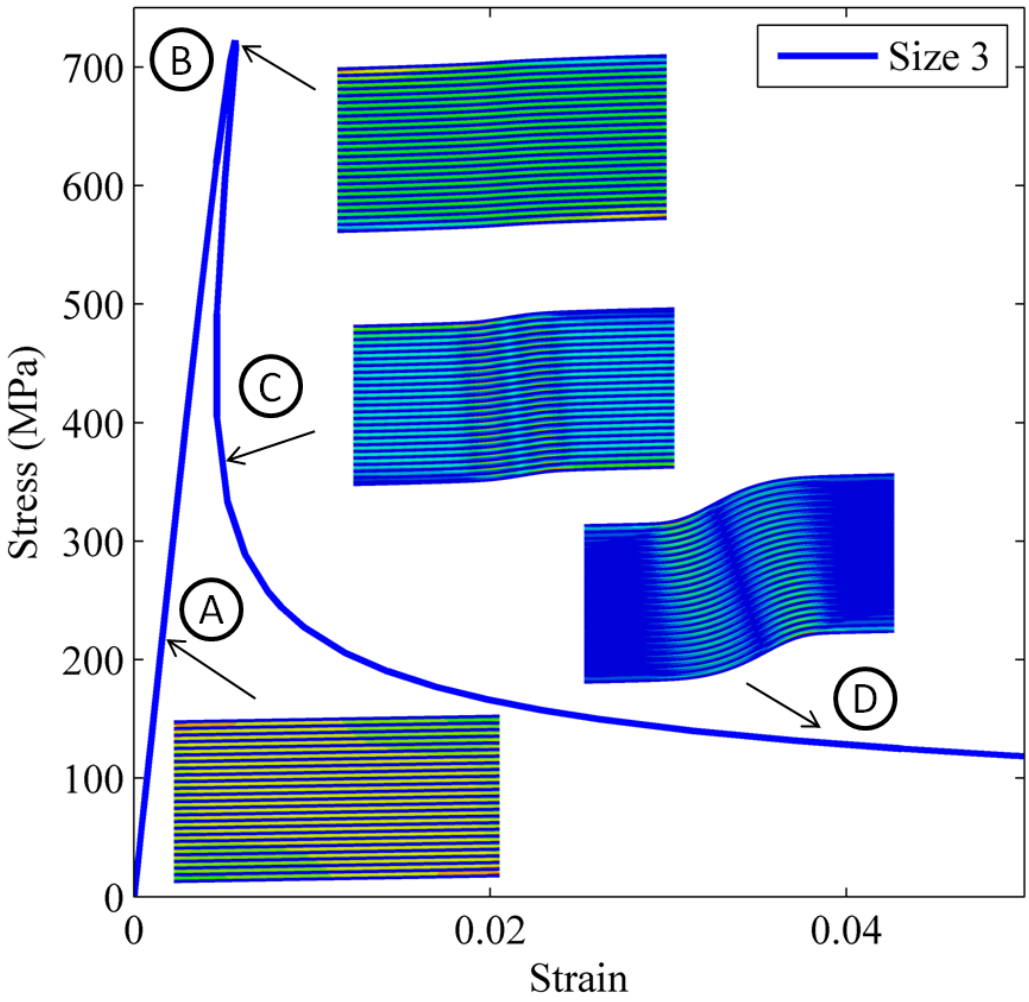

Figure B.3: Global stress-strain curve with deformation plots at different loading stages

observed that the peak stress is fairly low for model size 1, and gradually converges for sizes 3 and above as shown in Fig. B.5.

Typical deformation plots for Size 1 and Size 3 models are shown in Fig. B.6(a) and Fig. B.6(b). A distinct difference in the deformation behavior of the two models in the post-critical regime is observed. A compact kink band is observed in the Size 3 model and larger size models, but is absent in the Size 1 model. This difference is manifested in the stress-strain curve of the models as well. Size 3 model displays a snap-back response behavior whereas Size 1 does not. It can be concluded that the Size 1 model geometry does not facilitate the formation of the kink band because

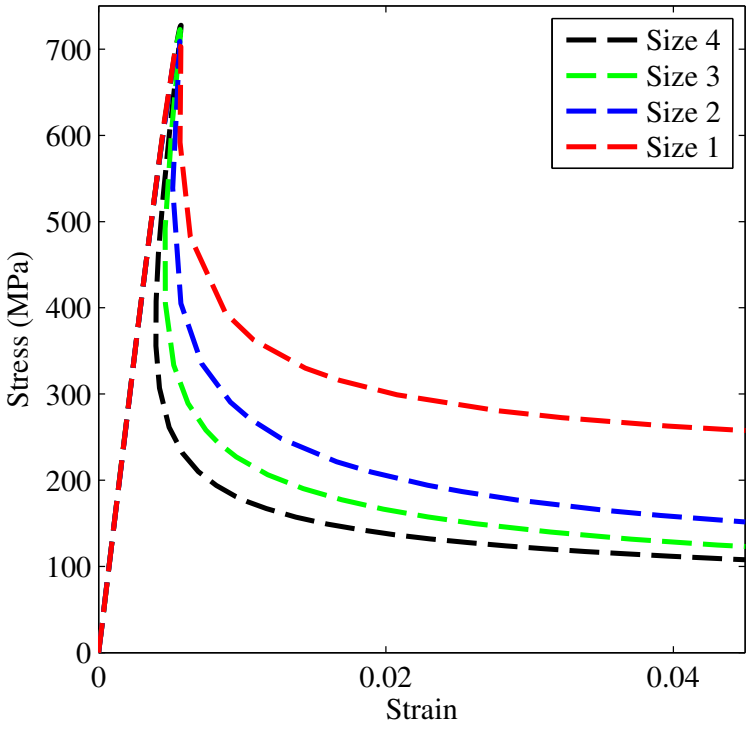

Figure B.4: Global stress-strain curves for different model sizes

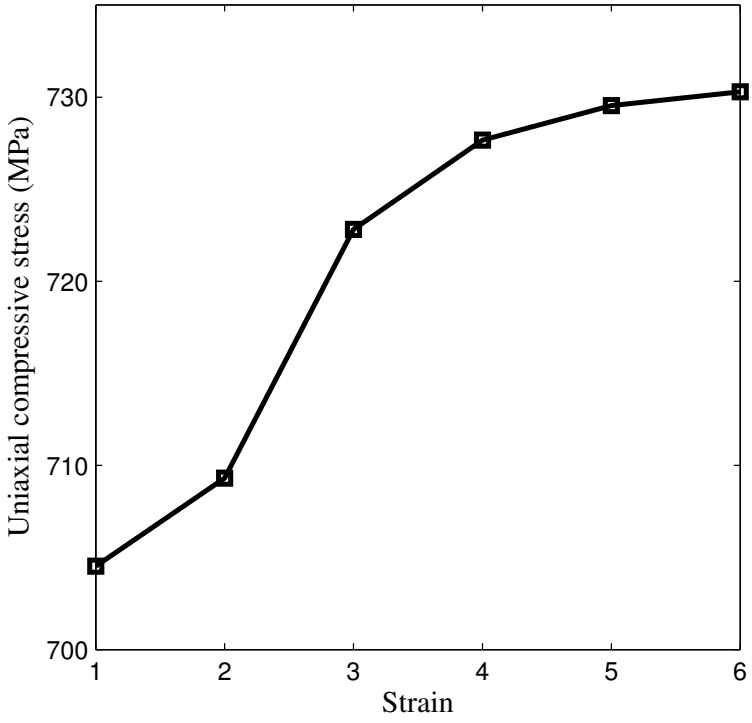

Figure B.5: Peak stress for models with perfect interfaces

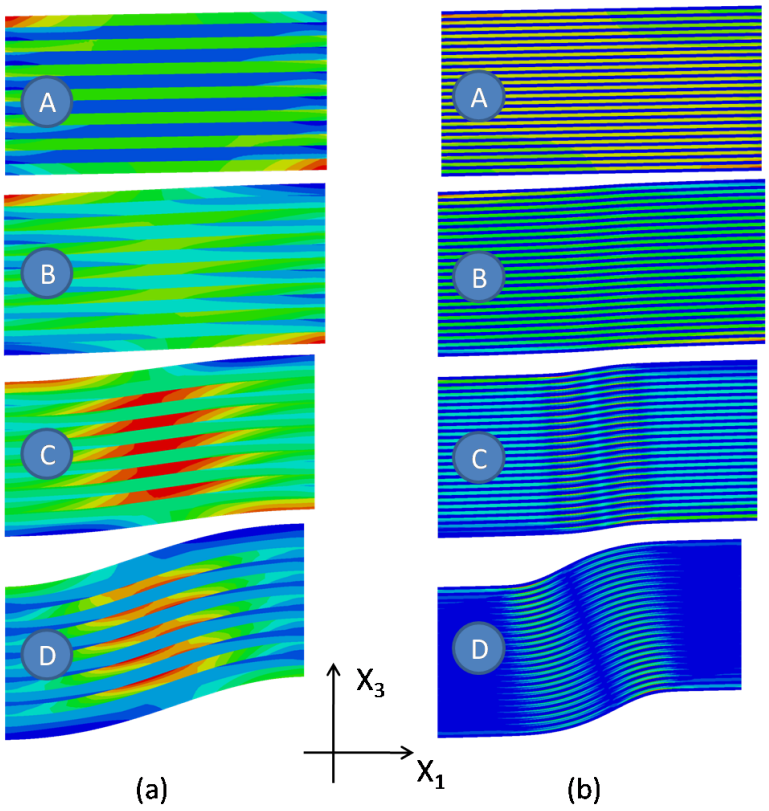

Figure B.6: (a) Deformation of Size 1 model; (b) Deformation of Size 3 model

its overall width is insufficient to accommodate the kink band, and therefore adds a geometrical constraint. This shows that the model size must not be restrictive in allowing the "free" formation of the kink band in the post-peak stress-strain regime. The percentage difference in peak stresses of the models of consecutive sizes are determined. The percentage difference in peak stress between Size 3 and Size 4 models (and between subsequent larger size models) is less than 1 percent. Therefore, the Size 3 model with 24 fibers is chosen as the baseline model for obtaining the compressive strength. Also, Size 3 model captures the kink band well within its overall length along the loading direction.

Table B.4: Local strains in model without splitting capability

Load Step	Local ϵ_{22}	Local γ_{12}
A	0.000915	0.00235
B	0.00725	0.06492
C	0.032	0.306
D	0.194	0.675

Observations

The local strains (ϵ_{22} and γ_{12}) in the local coordinate system at the center of the model (which also lies within the kink band at loading stages C and D) are tabulated in Table B.4. It is observed that these strains attain very large values beyond the peak stress, and exceed the failure strains of typical polymer matrix materials (*Ng et al.* (2010)). These high strains suggest fiber/matrix splitting, which has been observed in conjunction with the formation of kink banding (*Yerramalli and Waas* (2003), *Pimenta et al.* (2009a), *Pimenta et al.* (2009b)).

In the next section, Size 3 (baseline) model is considered to investigate the mechanics of the splitting process during kink band formation, where discrete cohesive zone method (DCZM) elements, (*Gustafson and Waas* (2009)) are added along the interface between the matrix and fibers. These elements model splitting through effective traction laws. The details of these laws are associated with the energetics of the splitting process. The following sections will explain the micromechanics based model with DCZM elements and the corresponding results of the parametric study that was conducted.

Interactive failure between splitting and kinking failure

DCZM elements are added along the fiber-matrix interfaces for allowing splitting to occur in conjunction with or without the kink-band formation. Fig. B.7(a) shows

a schematic of the DCZM elements added along the interface between the fibers and matrix with a 6 fiber model, shown as red lines. A similar analysis as that carried out without interface elements was conducted on models of different sizes with interface elements. It was found that Size 3 model gives a converged value of compressive strength even for the cases where interfaces separate. Therefore, subsequent analysis results reported correspond to the size 3 model, which was established as the minimum size required for predicting a converged value of compressive strength. Even though the DCZM elements are placed along the fiber-matrix interface, they represent approximately matrix cracks in the regions close to fibers which coalesce to form splitting cracks within the matrix. The DCZM elements are explained in the next section, followed by a parametric study for different sets of inputs to these elements.

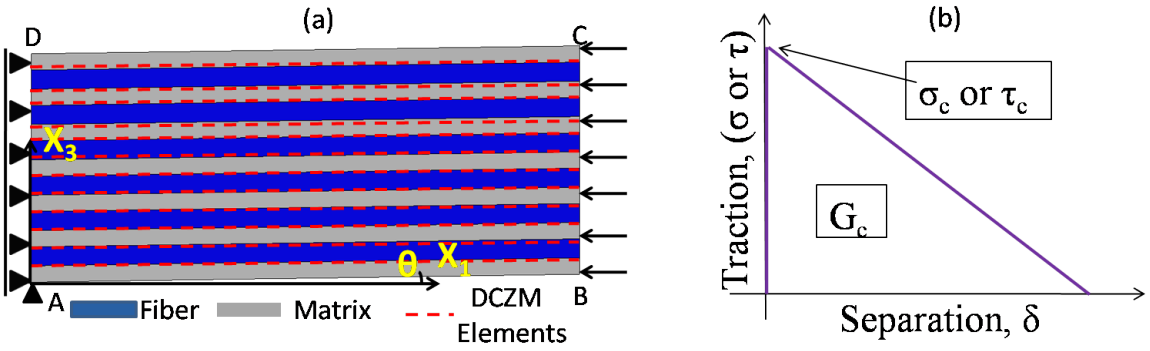

Figure B.7: a) 6 fiber model with cohesive elements added at the interface between fibers and matrix to accommodate splitting; (b) Triangular traction-separation law for DCZM elements

Modeling with Discrete cohesive zone method (DCZM) elements

DCZM elements are interface elements that adopt a 1D traction law capable of simulating crack formation and propagation, i.e. splitting. The element features the ability to predict splitting initiation based on a traction law that captures the cohesive strength and the fracture toughness, in each fracture mode (mode I and mode II in the current model).

The DCZM elements used in this chapter have been successfully employed in other studies involving crack propagation as presented in *Gustafson and Waas* (2009). A triangular cohesive law is adopted here, and is shown in Fig. B.7(b). The input parameters to DCZM elements are fracture toughness (G_{IC} and G_{IIC}) and cohesive strength (σ_c and τ_c). Several analyses are carried out for different combinations of these input parameters. These combinations of parameters are in the range of cohesive property values reported in the literature (For example, see *Jimenez and Miravete* (2004), *Jiang et al.* (2007)). Six cases are considered and are explained in detail in the following sections.

While buckling analysis is traditionally done using implicit codes with an arc-length method, e.g. RIKs method (as used for models with perfect interfaces in the previous sections), the inclusion of splitting in this study introduces convergence difficulties that is beyond the capabilities of implicit solvers to handle. Even though implicit solvers are unconditionally stable, the presence of two unstable failure mechanisms require very small time steps for convergence, and solutions diverge at critical points. Therefore, in this study, an explicit code (ABAQUS Explicit 6.10) with explicit user element subroutine for interface (DCZM) elements is used to generate the computational results. In this study, even though the loading is quasi-static, kink-banding, and splitting at the interfaces, are both dynamic events, which impart a large amount of kinetic energy. Therefore, for these types of problems, explicit analysis is used here. A comparison between RIKS and Explicit analysis is carried out for Size 3 model with only kinking capability (no splitting allowed) in the model. The global stress-strain curves from the two analyses are shown in Fig. B.8, and are in good agreement with each other. Therefore, the Explicit method is used with confidence in the following analyses.

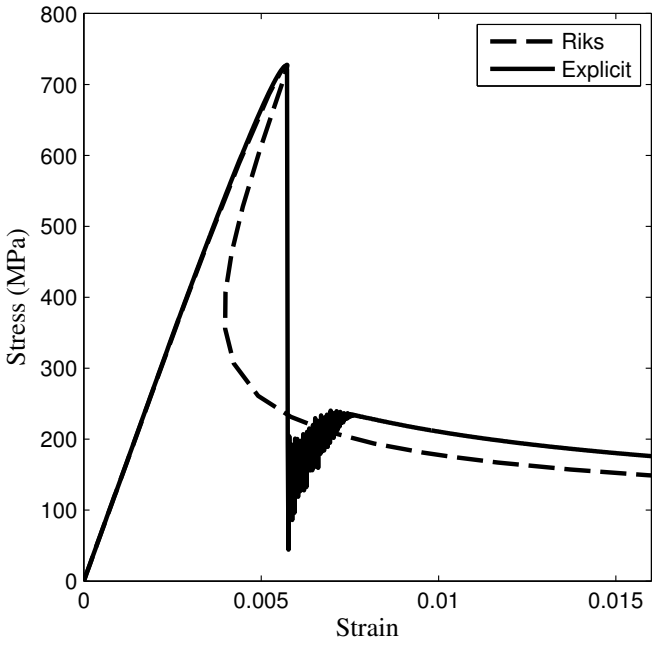

Figure B.8: Global stress-strain curves for Size 3 model using RIKS method and Explicit method for the case without splitting capability in the model

Parametric study

A parametric study is carried out to investigate the effect of varying magnitudes of fracture properties on the global compressive strength and failure mode (splitting or kinking) of the laminate. The different cases considered are shown in Table B.5.

In the first case, the fracture toughnesses in both mode-I and mode-II are held fixed at $0.525kJ/m^2$ and $1.751kJ/m^2$ while the cohesive strengths are varied as shown in Table B.5. In the second case, the fracture toughnesses in both mode-I and mode-II and the cohesive strength in mode-II are held fixed at $0.525kJ/m^2$, $1.751kJ/m^2$ and 80MPa respectively, while the cohesive strength in mode-I is varied as shown in Table B.5. In the third case, the fracture toughnesses in both mode-I and mode-II and the cohesive strength in mode-I are held fixed at $0.525kJ/m^2$, $1.725kJ/m^2$ and 40MPa respectively, while the cohesive strength in mode-II is varied. In the fourth case, the fracture toughnesses in both mode-I and mode-II are reduced to $0.00525kJ/m^2$ and $0.01751kJ/m^2$ respectively, while the cohesive strengths are varied as in Case 1.

Table B.5: Cases 1-4

	σ_c (N/mm^2)	G_{IC} (kJ/m^2)	τ_c (N/mm^2)	G_{IIC} (kJ/m^2)
Case 1.1	2.5	0.525	5.0	1.751
Case 1.2	5.0	0.525	10.0	1.751
Case 1.3	10.0	0.525	20.0	1.751
Case 1.4	20.0	0.525	40.0	1.751
Case 2.1	2.5	0.525	80	1.751
Case 2.2	5.0	0.525	80	1.751
Case 2.3	10.0	0.525	80	1.751
Case 3.1	40	0.525	10	1.751
Case 3.2	40	0.525	20	1.751
Case 3.3	40	0.525	40	1.751
Case 4.1	2.5	0.00525	5.0	0.01751
Case 4.2	5.0	0.00525	10.0	0.01751
Case 4.3	10.0	0.00525	20.0	0.01751
Case 4.4	20.0	0.00525	40.0	0.01751

Results and discussion

The macroscopic stress-strain responses for all the above cases were determined. It is observed that the compressive strengths are unaltered by varying either mode-I or mode-II fracture toughness, when the cohesive strengths are fixed at large values (say 40 MPa and 80 MPa in mode-I and mode-II). This is because the cohesive strengths in either case are fixed at relatively large values, which results in no separation in the DCZM elements, and hence the model responds by a mechanism of kink band formation with no energy released by splitting. As such, the fracture toughness of the interface corresponding to high cohesive strengths of interfaces has no effect on the compressive strength of the laminate.

In Case 1 where the cohesive strengths are systematically reduced in magnitude, while keeping the fracture toughnesses fixed, the compressive strength reduces with

a reduction in the cohesive strengths. Further, to determine the influence of mode-I and mode-II cohesive strengths individually on the compressive strengths of the laminate, the cohesive strengths in the two modes are reduced individually keeping one at a relatively large value, as described in Case 2 and Case 3. Here, it is observed that the compressive strength of the laminate is influenced by a variation in mode-II cohesive strength, but not by a reduction in the mode-I cohesive strength of the interface elements. This implies that the failure of the unidirectional laminate is by mode-II splitting at the fiber-matrix interface, with little influence from the mode I component. That is, in Case 3, as the mode-II cohesive strength of the DCZM elements are reduced, the separation between the interface elements increases beyond the critical separation corresponding to mode-II cohesive strength in the traction-separation law, beyond which the the DCZM elements soften reducing their load bearing capacity. This results in splitting of the interfaces, followed by a reduction in the macroscopic compressive strength.

In case 4, again the compressive strength is seen to reduce with a reduction in cohesive strength as observed in case 3, and the magnitudes in each case are unaltered as compared to case 3. Therefore, the fracture toughness values with splitting interfaces do not influence the compressive strength of the laminate. The corresponding global compressive stress-strain curves are plotted in Fig. B.9(a). As the mode-II cohesive strength is increased, the compressive strength appears to converge to the compressive strength of the model with no interface elements given in Fig. B.3.

The deformation plots representing displacement in global x_1 - direction at different loading stages (refer to Fig. B.9(b)) for the model without interface elements are shown in Fig. B.10. Stage 3 represents the point corresponding to the compressive strength of the laminate, and Stage 4 lies in the post-peak regime of the global stress-strain curve. A distinct kink band is formed at Stage 4 showing kink band failure mode.

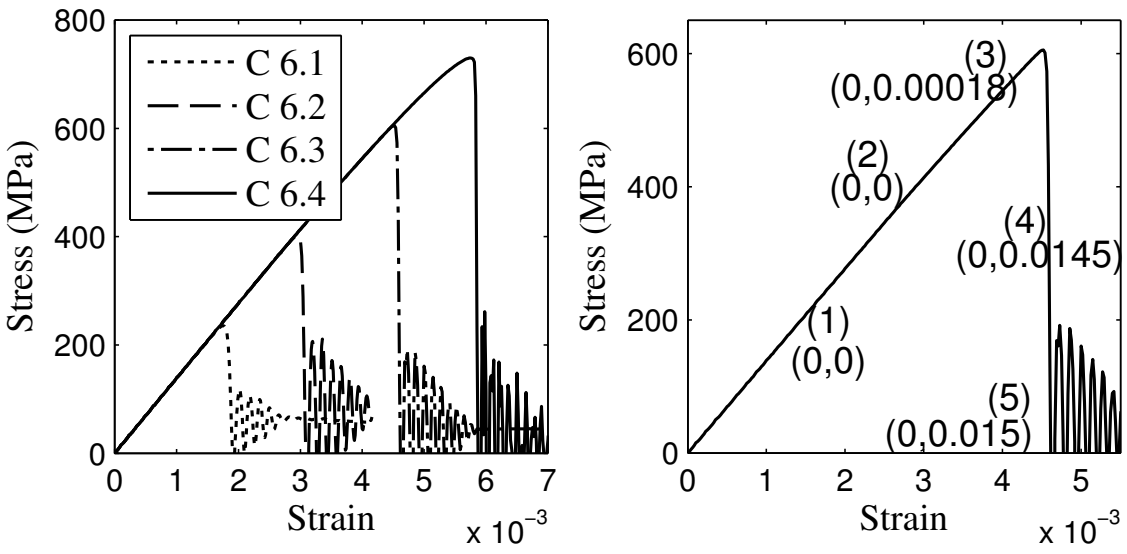

Figure B.9: (a) Global stress-strain curves for Case 4; (b) Global stress-strain curve for Case 4.3 with (G_I/G_{IC},G_{II}/G_{IIC}) at different loading stages

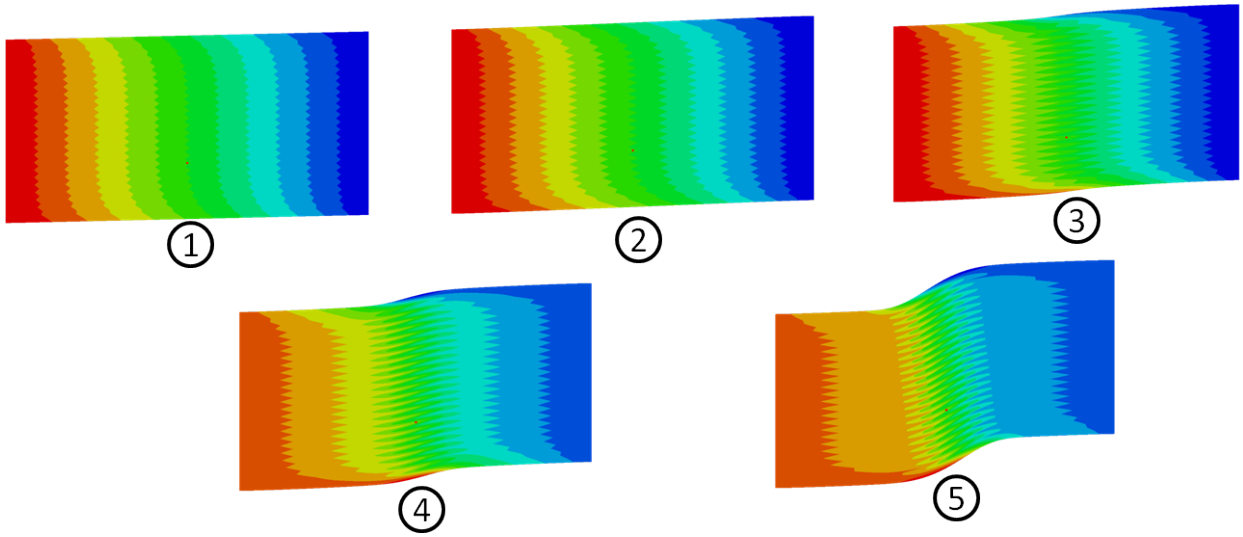

Figure B.10: Deformation (U_1) plots of the model showing failure by kinking (model without interface elements)

Corresponding deformation plots for model with interface elements for Case 4.3 is shown in Fig. B.11. Again, Stage 3 corresponds to compressive strength in the global stress-strain curve, and it is observed that the interfaces begin to separate in mode-II at this stage. That is, there is a relative displacement (shown by drastic change is

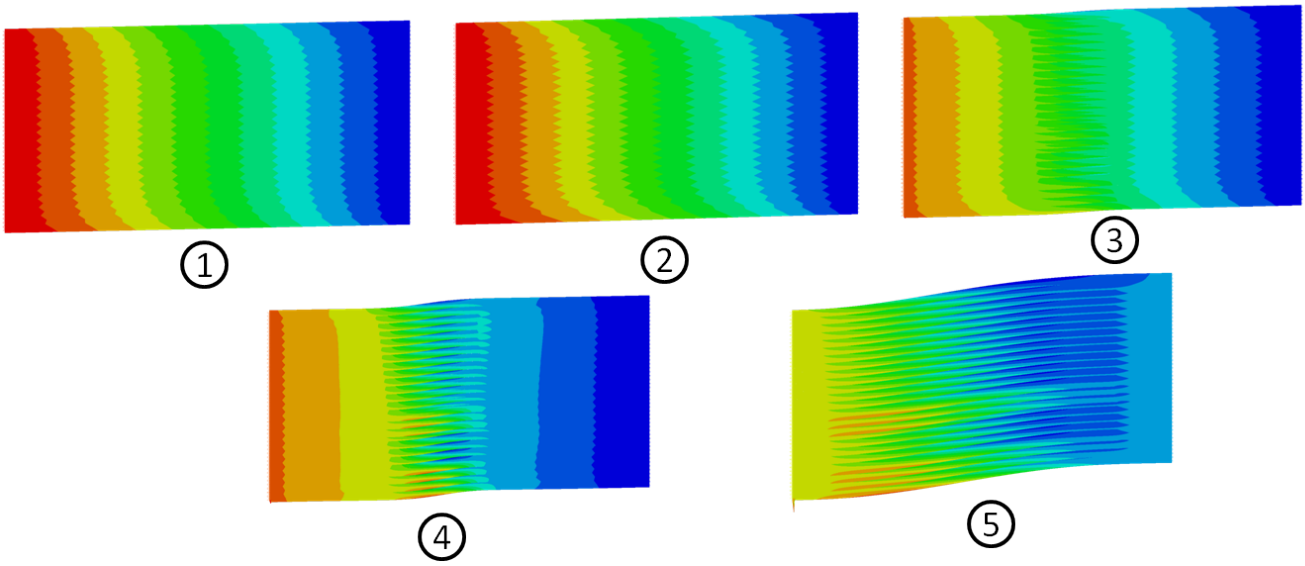

Figure B.11: Deformation (U_1) plots of the model failure by splitting (model with interface elements)

color) in the loading direction between the top and bottom of the interface (mode-II sliding). Stage 4 is a point in the post-peak regime, where the interface separation is more evident, and at stage 5 the interface elements have opened through the length of the model. Hence, the interfaces are completely broken. Therefore, it is deduced that energy is dissipated through mode-II splitting, and there is no distinct kink band formed in the post peak regime. The ratios of fracture energy released per surface area with respect to the critical fracture toughness (G_I/G_{IC} and G_{II}/G_{IIC}) in mode-I and mode-II at the center of the model are shown at different loading stages on the global stress-strain curve plotted in Fig. B.9(b) for the case 4.3. It is observed that the mode-II failure mode is dominant, since the ratio G_{II}/G_{IIC} is much greater than G_I/G_{IC} near the global peak strength and beyond. A similar mode-II dominance is observed in the rest of the cases.

For the same case, (case 4.3), the local strains ϵ_{22} and γ_{12} as a function of the loading history are tabulated in Table B.6. These strains are now compared against the corresponding strains for the case without the interface DCZM elements that was

Table B.6: Local strains in model with DCZM

Load Step	Local ϵ_{22}	Local γ_{12}
A	0.000811	0.00185
B	0.00566	0.0533
C	0.01357	0.0056

reported earlier in the chapter, Table B.4. Load steps A,B and C correspond to the same loading stages as mentioned in Table B.4.

It is observed that the local strains in the two models are comparable prior to the attainment of the peak strength. However, in the post-peak regime, the strains drop in the model with the DCZM, in contrast to the model with non-separating interfaces. This is because energy is released by splitting beyond the peak strength, and the model does not experience extremely high local strains as before. This is more realistic, since the lamina cannot bear such large strains as shown in Table B.4. Therefore, adding the interface elements allows the model to dissipate energy through splitting only, or in conjunction with kinking. From the above results, it can also be deduced that a good knowledge of the mode-II cohesive strength of the fiber-matrix interface in the laminate is necessary to determine the compressive strength and failure mode of the unidirectional laminate accurately.

Conclusions

The mechanics of failure mode interaction in the compression response of fiber composites has been studied by utilizing a micromechanics based finite element model incorporating discrete cohesive zone elements. It is shown that the mode II cohesive shear strength has a significant influence in affecting the magnitude of the composite compressive strength. A minimum size of the representative fiber/matrix volume element (RVE) was established to accurately capture the kink band failure mode. Compressive strength predictions with smaller RVE sizes was found to be misleading.

Models that included interface cohesive elements captured the interaction between splitting and kink band formation for several of the different cases considered in this study. It was determined that compressive failure by sliding splitting was dominant, and the compressive strength is affected by the degree of mode-II cohesive strength of the interface. The compression response of the composites was studied that highlights the competition between splitting and kink banding. It was concluded that a model should have splitting capability to determine the compressive response of a laminate, and the compressive strength and mode of failure (splitting or kinking) are dependent on the interface fracture properties.

BIBLIOGRAPHY

BIBLIOGRAPHY

ABAQUS (6.10), *ABAQUS 6.10 Documentation*, Simulia.

Ahn, J. H., and A. M. Waas (1999), A micromechanics-based finite element model for compressive failure of notched uniply composite laminates under remote biaxial loads, *Journal of Engineering Materials and Technology - Transactions of the ASME*, *121*(3), 360–366.

Ahn, J. H., and A. M. Waas (2002), Prediction of compressive failure in laminated composites at room and elevated temperature, *AIAA Journal*, *40*(2), 346–358.

ARAMIS (6.3.0), *ARAMIS Software Documentation*, GOM Optical Measuring Teqhniques.

Armero, F., and K. Garikipati (1996), An analysis of strong discontinuities in multiplicative finite strain plasticity and their relation with the numerical simulation of strain localization in solids, *Int J Solids Struct*, *33*, 2863–2885.

ASTM(D3165) (2007), Standard test method for strength properties of adhesives in shear by tension loading of single-lap-joint laminated assemblies.

ASTM(D5528) (2007), Standard test method for mode i interlaminar fracture toughness of unidirectional fiber-reinforced polymer matrix composites.

Barenblatt, G. (1962), The mathematical theory of equilibrium cracks in brittle fracture, *Advances in Applied Mechanics*, *7*, 55–129.

Basu, S., A. M. Waas, and D. R. Ambur (2006), Compressive failure of fiber composites under multi-axial loading, *Journal of the Mechanics and Physics of Solids*, *54*(3), 611–634.

Bazant, Z., and L. Cedolin (1991), *Stability of Structures: Elastic, Inelastic, Fracture, and Damage Theories*, Dover books on engineering, Dover Publ.

Bazant, Z., and B. Oh (1983), Crack band theory for fracture of concrete, *Materials and Structures*, *16*, 155–177.

Beghini, A., Z. P. Bazant, A. M. Waas, and S. Basu (2006), Postcritical imperfection sensitivity of sandwich or homogenized orthotropic columns soft in shear and in transverse deformation, *International Journal of Solids and Structures*, *43*(18-19), 5501–5524.

Belytschko, T., N. Mos, S. Usui, and C. Parimi (2001), Arbitrary discontinuities in finite elements, *International Journal for Numerical Methods in Engineering*, *50*(4), 993–1013.

Berbinau, P., C. Soutis, and I. A. Guz (1999), Compressive failure of 0^0 unidirectional carbon-fibre-reinforced plastic (cfrp) laminates by fibre microbuckling, *Composites Science and Technology*, *59*, 1451–1455.

Blockley, R., and W. Shyy (2010), *Encyclopedia of Aerospace Engineering, 9 Volume Set*, no. v. 7 in Encyclopedia of Aerospace Engineering, John Wiley & Sons.

Bogert, P. B., A. Satyanarayana, and P. B. Chunchu (2006), Comparison of damage path predicions for composite laminates by explicit and standard finite element analysis tool, *47th AIAA Structures, Structural Dynamics, and Materials Conference*.

Budiansky, B., and N. A. Fleck (1993), Compressive failure of fiber composites, *Journal of the Mechanics and Physics of Solids*, *41*(1), 183–211.

Camacho, G. T., and M. Ortiz (1996), Computational modeling of impact damage in brittle materials, *Int J Solids Struct*, *33*, 2899–2938.

Camanho, P., P. Maim, and C. Dvila (2007), Prediction of size effects in notched laminates using continuum damage mechanics, *Composites Science and Technology*, *67*(13), 2715–2727, doi:10.1016/j.compscitech.2007.02.005.

Committee on Integrated Computational Materials Engineering, N. R. C. (2008), *Integrated Computational Materials Engineering: A Transformational Discipline for Improved Competitiveness and National Security*, The National Academies Press.

Davidson, B. D., and X. Sun (2006), Geometry and data reduction recommendations for a standardized end notched flexure test for unidirectional composites, *Journal of ASTM International*, *3*.

de Borst, R., and P. Nauta (1985), Non-orthogonal cracks in a smeared finite element model, *Eng. Comput.*, *2*, 35–46.

Dugdale, D. S. (1960), Yielding of steel sheets containing slits, *Journal of the Mechanics and Physics of Solids*, *8(2)*, 100–104.

Feld, N., O. Allix, and E. Baranger (2011), Micro-mechanical prediction of ud laminates behavior under combined compression up to failure: influence of matrix degradation, *Journal of Composite Materials*, *45*(22), 2317–2333.

Garikipati, K. (2002), A variational multiscale method to embed micromechanical surface laws in the macromechanical continuum formulation, *CMES-COMPUTER MODELING IN ENGINEERING & SCIENCES*, *3*(2), 175–184.

Garikipati, K., and T. J. R. Hughes (1998), A study of strain-localization in a multiple scale framework. the one dimensional problem, *Comput Methods Appl Mech Eng*, *159*, 193–222.

Guedes, R. M., M. F. S. F. de Moura, and F. J. Ferreira (2008), Failure analysis of quasi-isotropic cfrp laminates under high strain rate compression loading, *Composite Structures*, *84*(4), 362–368.

Gustafson, P., and A. Waas (2009), The influence of adhesive constitutive parameters in cohesive zone finite element models of adhesively bonded joints, *International Journal of Solids and Structures*, *46*(10), 2201–2215.

Gustafson, P. A. (2008), Analytical and experimental methods for adhesively bonded joints subjected to high temperatures, *Dissertation, University of Michigan*.

Hancox, N. L. (1975), The compression strength of unidirectional carbon fibre reinforced plastic, *Journal of Materials Science*, *10*, 234–242.

Hashin, Z., and B. W. Rosen (1964), The elastic moduli of fiber-reinforced materials, *Journal of Applied Mechanics*, *31*(2), 223–232, doi:10.1115/1.3629590.

Heinrich, C., and A. M. Waas (2012), Investigation of progressive damage and fracture in laminated composites using the smeared crack approach, *53rd AIAA/ASME/ASCE/AHS/ASC Structures, Structural Dynamics and Materials Conference, 23 - 26 April 2012, Honolulu, Hawaii (AIAA 2012-1537)*.

Herakovich, C. T. (1998), *Mechanics of Fibrous Composites*, John Wiley & Sons, Inc.

Hill, R. (1964), Theory of mechanical properties of fibre-strengthened materials: I. elastic behaviour, *Journal of the Mechanics and Physics of Solids*, *12*(4), 199–212, doi:10.1016/0022-5096(64)90019-5.

Hosur, M. V., J. Alexander, U. K. Vaidya, and S. Jeelani (2001), High strain rate compression response of carbon/epoxy laminate composites, *Composite Structures*, *52*(3-4), 405–417.

Jiang, W. G., S. R. Hallett, B. G. Green, and M. R. Wisnom (2007), A concise interface constitutive law for analysis of delamination and splitting in composite materials and its application to scaled notched tensile specimens, *International Journal for Numerical Methods in Engineering*, *69*(6), 1982–1995.

Jimenez, M. A., and A. Miravete (2004), Application of the finite element method to prediction of onset of delamination growth, *Journal of Composite Materials*, *38*(15), 1309–1335.

Jin, Z.-H., and C. T. Sun (2005), Cohesive zone modeling of interface fracture in elastic bi-materials, *Engineering Fracture Mechanics*, *72*, 1805–1817.

Jirasek, M. (2000), Comparative study on finite elements with embedded discontinuities, *Comput Methods Appl Mech Eng*, *188*, 307–330.

Kyriakides, S., R. Arseculeratne, E. J. Perry, and K. M. Liechti (1995), On the compressive failure of fiber-reinforced composites, *International Journal of Solids and Structures*, *32*(6-7), 689–738.

Lager, J. R., and R. R. June (1969), Compressive strength of boron-epoxy composites, *Journal of Composite Materials*, *10*, 234–242.

Lee, S. H., and A. M. Waas (1999), Compressive response and failure of fiber reinforced unidirectional composites, *International Journal of Fracture*, *100*, 275–306.

Lee, S. H., C. S. Yerramalli, and A. M. Waas (2000), Compressive splitting response of glass-fiber reinforced unidirectional composites, *Composites Science and Technology*, *60*, 2957–2966.

Lo, K. H., and E. S. M. Chim (1992), Compressive strength of unidirectional composites, *Journal of Reinforced Plastics and Composites*, *11*, 838–896.

Lubliner, J. (2008), *Plasticity Theory*, Dover Publications.

Martin, E., D. Leguillon, and N. Carrere (2012), A twofold strength and toughness criterion for the onset of free-edge shear delamination in angle-ply laminates, *International Journal of Solids and Structures*, *47*(9), 1297–1305.

Martinez, G. M., M. R. Piggott, D. M. R. Bainbridge, and B. Harris (1981), The compression strength of composites with kinked, misaligned and poorly adhering fibres, *Journal of Materials Science*, *16*.

Moes, N., and T. Belytschko (2002), Extended finite element method for cohesive crack growth, *Eng Fract Mech*, *69(7)*, 813–833.

Moes, N., J. Dolbow, and T. Belytschko (1999), A finite element method for crack growth without remeshing, *Int J Numer Methods Eng*, *46*, 131–150.

Naik, N. K., and R. S. Kumar (1999), Compressive strength of unidirectional composites: evaluation and comparison of prediction models, *Composite Structures*, *46*(3), 299–308.

Ng, W. H., A. G. Salvi, and A. M. Waas (2010), Characterization of the in-situ nonlinear shear response of laminated fiber-reinforced composites, *Composites Science and Technology*, *70*(7), 1126–1134.

Nimmer, R. P., L. R. Kaisand, L. P. Inzinna, and A. M. Wafa (1996), Mode-i and mode-ii crack growth rate data for hercules 8551-7, *Technical Information Series, GE Research & Development Center*.

Ochola, R. O., K. Marcus, G. N. Nurick, and T. Franz (2004), Mechanical behaviour of glass and carbon fibre reinforced composites at varying strain rates, *Composite Structures*, *63*(3-4), 455–467.

Oliver, J., A. Huespe, and P. Snchez (2006), A comparative study on finite elements for capturing strong discontinuities: E-fem vs x-fem, *Computer Methods in Applied Mechanics and Engineering*, *195*(37–40), 4732–4752.

Pankow, M. R. (2010), The deformation response of 3d woven composites subjected to high rates of loading, *Thesis, University of Michigan (http://hdl.handle.net/2027.42/77889)*.

Pietruszczak, S. T., and Z. Mroz (1981), Finite element analysis of deformation of strain softening materials, *Int J Numer Methods Eng*, *17*, 327–334.

Pimenta, S., R. Gutkin, S. T. Pinho, and P. Robinson (2009a), A micromechanical model for kink-band formation: Part i experimental study and numerical modelling, *Composites Science and Technology*, *69*, 948–955.

Pimenta, S., R. Gutkin, S. T. Pinho, and P. Robinson (2009b), A micromechanical model for kink-band formation: Part ii analytical modelling, *Composites Science and Technology*, *69*, 956–964.

Pineda, E., and A. M. Waas (2012), Modeling progressive failure of fibre reinforced laminated composites: Mesh objective calculations, *Aeronautical Journal*, *116*, 1221–1245.

Pintado, P., C. Pedraza, J. M. del Castillo, and F. G. Benitez (2001), Experimental investigation of the dynamic response of graphite-epoxy composite laminates under compression, *Composite Structures*, *53*(4), 493–497.

Pipes, R. B., and I. M. Daniel (1971), Moiré analysis of the interlaminar shear edge effect in laminated composites, *Journal of Composite Materials*, *5*.

Pipes, R. B., and N. J. Pagano (1970), Interlaminar stresses in composite laminates under uniform axial extension, *Journal of Composite Materials*, *4*.

Prabhakar, P., and A. Waas (2012a), The interaction of failure modes in the compression response and failure of laminated composites, *Proceedings of the 53rd AIAA/ASME/ASCE/AHS/ASC Structures, Structural Dynamics, and Materials Conference, Hawaii, USA (AIAA 1216559)*.

Prabhakar, P., and A. M. Waas (2012b), Upscaling from a micromechanics model to capture laminate compressive strength due to kink banding instability, *Computational Materials Science (http://dx.doi.org/10.1016/j.commatsci.2012.08.025)*.

Prabhakar, P., and A. M. Waas (2012c), Interaction between kinking and splitting in the compressive failure of unidirectional fiber reinforced laminated composites, *Composite Structures (http://dx.doi.org/10.1016/j.compstruct.2012.11.005)*.

Rots, J., and R. de Borst (1987), Analysis of mixed-mode fracture in concrete, *J. Eng. Mech.*, *113(11)*, 1739–1758.

Rots, J., P. Nauta, G. Kuster, and J. Blaauwendraad (1985), Smeared crack approach and fracture localization in concrete, *Heron*, *30(1)*, 1–48.

Rudraraju, S. S., A. Salvi, K. Garikipati, and A. M. Waas (2010), In-plane fracture of laminated fiber reinforced composites with varying fracture resistance: experimental observations and numerical crack propagation simulations, *Int J Solids Struct*, *47(78)*, 901–911.

Schapery, R. A. (1995), Prediction of compressive strength and kink bands in composites using a work potential, *International Journal of Solids and Structures*, *32*(6-7), 739–765.

Schellekens, J. C. J., and R. DeBorst (1993), On the numerical integration of interface elements, *Int J Numer Methods Eng*, *36*, 43–66.

Schultheisz, C. R., and A. M. Waas (1996), Compressive failure of composites .1. testing and micromechanical theories, *Progress in Aerospace Sciences*, *32*(1), 1–42.

Song, S., and A. M. Waas (1993), A nonlinear elastic foundation model for interlaminar fracture of laminated composites, *Compos Eng*, *3(10)*, 945–959.

Sukumar, M. N. M. B., N., and T. Belytschko (2000), An extended finite element method (x-fem) for two- and three-dimensional crack modeling, *Numer. Methods Eng.*, *48(11)*, 1741–1760.

Sun, C. T., and A. W. Jun (1994), Compressive strength of unidirectional fiber composites with matrix non-linearity, *Composites Science and Technology*, *52*(4), 577–587.

Ungsuwarungsri, T., and W. G. Knauss (1987), The role of damage-softened material behavior in the fracture of composites and adhesives, *Int J Fract*, *35*, 221–241.

Vogler, T. J., S. Y. Hsu, and S. Kyriakides (2001), On the initiation and growth of kink bands in fiber composites. part ii: analysis, *International Journal of Solids and Structures*, *38*, 2653–2682.

Waas, A. M., and C. R. Schultheisz (1996), Compressive failure of composites .2. experimental studies, *Progress in Aerospace Sciences*, *32*(1), 43–78.

Waas, A. M., C. D. Babcock Jr., and W. G. Knauss (1990), An experimental study of compression failure of fibrous laminated composites in the presence of stress gradients, *International Journal of Solids and Structures*, *26*(9-10), 1071–1098.

Wisnom, M. R. (1994), The effect of fibre waviness on the relationship between compressive and flexural strengths of unidirectional composites, *Journal of Composite Materials*, *28*.

Xie, D., and Waas (2006), Discrete cohesive zone model for mixed-mode fracture using finite element analysis, *Eng Fract Mech*, *73*, 1783–1796.

Xie, D., A. Salvi, C. Sun, A. M. Waas, and A. Caliskan (2006), Discrete cohesive zone model to simulate static fracture in 2-d triaxially braided carbon fiber composites, *J Compos Mater*, *40*, 1–22.

Xu, X. P., and A. Needleman (1994), Numerical simulation of fast crack growth in brittle solids, *J Mech Phys Solids*, *42*, 1397–1434.

Xu, Y. L., and K. L. Reifsnider (1993), Micromechanical modeling of composite compressive strength, *Journal of Composite Materials*, *27*, 572–588.

Yerramalli, C. S., and A. M. Waas (2003), A failure criterion for fiber reinforced polymer composites under combined compression-torsion loading, *International Journal of Solids and Structures*, *40*(5), 1139–1164.

Yerramalli, C. S., and A. M. Waas (2004a), The effect of fiber diameter on the compressive strength of composites - a 3d finite element based study, *Computer Modeling in Engineering and Sciences*, *6*(1), 1–16.

Yerramalli, C. S., and A. M. Waas (2004b), A nondimensional number to classify composite compressive failure, *Journal of Applied Mechanics - Transactions of the ASME*, *71*(3), 402–408.

Yurgartis, S. W. (1987), Measurement of small angle fiber misalignments in continuous fiber composites, *Composites Science and Technology*, *30*, 279–293.

Zhang, D., J. Ye, and H. Y. Sheng (2006), Free-edge and ply cracking effect in cross-ply laminated composites under uniform extension and thermal loading, *Composite Structures*, *76*(4), 314–325.